An Experimental Determination of the Trailing-Edge Base Pressure on Blades in Transonic Turbine Cascades

by

Michael W. Walls

Thesis submitted to the Faculty of the

Virginia Polytechnic Institute and State University

in partial fulfillment of the requirements for the degree of

Master of Science

in

Mechanical Engineering

APPROVED:

Dr. Hal L. Moses, Chairman

Dr. John Moore

Dr. Eugene F. Brown

September, 1993

Blacksburg, Virginia

An Experimental Determination of the Trailing-Edge Base Pressure on Blades in Transonic Turbine Cascades

by

Michael W. Walls

Dr. Hal L. Moses, Chairman

Mechanical Engineering

(ABSTRACT)

This thesis documents an experimental investigation of the base (trailing edge) pressure and its approximate distribution on a transonic turbine blade. Since the base pressure plays an important role in determining the profile loss on blades with thick trailing edges, both the base pressure and the blade losses are presented for a range of transonic exit Mach numbers. The overall objective of this work is to provide experimental data for improving current computer-based models used in designing turbine blades.

The two-dimensional cascade was tested in the VPI&SU Transonic Cascade Wind Tunnel, a blow-down type of tunnel facility. The blade design for the cascade was based on the pitchline profile of the high pressure turbine in a commercial jet engine with a design exit Mach number of approximately 1.2. In order to carefully instrument the thin trailing edge, the blades used in the experiment were made five times the size of the actual engine blade. With this large-scale blade, five static pressure taps were placed around the trailing edge. In addition to these taps, the rearward portion of the suction surface was also instrumented with five static pressure taps. The aerodynamic losses were quantified by a loss coefficient: the mass-averaged total pressure drop divided by the total pressure upstream of the blade row. These measured pressures were taken with a fixed total pressure probe upstream of the cascade and a pitchwise

traversing probe in the downstream position. The cascade was tested for an exit Mach number ranging from 0.70 to 1.40.

The results of the experiments indicate a decreasing normalized base pressure (p_B/p_{t1}) with increasing downstream Mach number (M_2) until the minimum value of p_B/p_{t1} = 0.30 at M_2 = 1.30. The approximate base pressure distributions for all transonic downstream Mach numbers indicate nearly uniform pressure around the central 90° of the trailing edge. Results for the profile loss are displayed for exit Mach numbers between 0.70 and 1.35; the trend of increasing loss with decreasing base pressure is shown. The shadowgraph pictures taken reveal the trailing edge region of the flow for several downstream transonic Mach numbers.

ACKNOWLEDGEMENTS

I would like to thank my advisor, Dr. Hal Moses, for the overall guidance of this research project. Without his continual assistance and direction, none of this work would have been possible. I appreciate the times he has provided me with the wise advice necessary for the success of this research.

I would also like to thank Dr. John Moore and Dr. Eugene Brown for serving on my committee. Both of them have given me useful advice for this project and, from their courses, I am indebted to them for most of my knowledge of fluid mechanics and turbomachinery.

The financial assistance for this research has been provided by General Electric Aircraft Engines and the Tau Beta Pi Association. I am especially thankful to Brent Gregory and Monty Shelton of General Electric for the initial idea for this project and for their patience in seeing the idea carried out.

A special thanks is to be given to Roger Doughty and Tibor Kiss, who have continually helped me in running the wind tunnel. I thank Roger for his expertise concerning the

"ins" and "outs" of how to run the wind tunnel and for his day-to-day assistance. I thank Tibor for his assistance in the wind tunnel, especially with teaching me how to take the shadowgraph pictures. I greatly appreciate the computational data he has provided for this thesis. I would also like to thank Wade Pulliam for his help in running the wind tunnel and for breaking up some of the monotony of working in the "dungeon". I wish all of these guys the best in their research and their future careers.

Finally, I thank Gary Stafford at the Cascade Wind Tunnel and Jerry Lucas in the Mechanical Engineering Shop for their technical assistance.

TABLE OF CONTENTS

LIST OF TABLES

LIST OF FIGURES

LIST OF SYMBOLS

Symbols:

A : Channel Area

A^* : Throat Area

C : Blade Chord

Cp : Pressure Coefficient

H : Boundary Layer Shape Factor

h : Shear Layer Thickness in Tanner's [7] model

h^* : Projected Shock Wave Length in Tanner's [7] model

j : Direction Normal to Blade Surface in ANSERS Code

k : Direction Tangential to Blade Surface in ANSERS Code

L : Mass-averaged Loss

M : Mach Number

P : Pitch Length

p : Static Pressure

p_t : Total Pressure

Δp_t : Total Pressure Difference, p_{t1}-p_{t2}

R : Ideal Gas Law Constant

RH : Upstream Relative Humidity

S : Span Length

St : Strouhal Number

T : Throat Length

T_t : Total Temperature

T_s : Static Temperature

te : Trailing Edge Thickness

U : Velocity in the Direction of the Flow

u : Velocity in x-direction

v : Velocity in y-direction

x : Direction Along Wind Tunnel Axis

y : Pitchwise Direction

β : Relative Flow Angle (measured counterclockwise from x)

γ : Specific Heat Ratio

δ : Trailing Edge Wedge Angle or Boundary Layer Thickness

δ^* : Boundary Layer Displacement Thickness

ϵ : Suction Surface Turning Downstream of Throat

θ : Boundary Layer Momentum Thickness

μ : Viscosity

ρ : Density

Subscripts:

$()_{atm}$: Atmospheric

$()_{ax}$: Axial

$()_B$: Base Region

$()_i$: Initial (Beginning of Run)

$()_{is}$: Isentropic

$()_j$: Discrete y-position of Downstream Probe

$()_{te}$: Trailing Edge

$()_\infty$: Freestream

$()_1$: Upstream Location

$()_2$: Downstream Location Behind Blade #2

$()_3$: Downstream Location Behind Blade #3

1.0 INTRODUCTION

In attempts to evaluate the performance of aircraft engines, a large body of research over the past several decades has been devoted to studying the flow losses occurring within the compressor and turbine blade rows. Although various definitions have been conceived for quantifying these losses, one of the most common and well-known definitions is the concept of *drag*.

For the flow over a body of arbitrary shape, the drag force is defined as the force component acting on the body along the axis of the freestream. In the classical potential flow theory, the predicted drag for the flow over a body of any shape is zero. In reality, as experiments have shown, all bodies immersed in a moving fluid will exhibit a finite drag. This drag force is commonly divided into two components: one due to the frictional forces acting over the surfaces and one due to the pressure distribution around the body. The later component is commonly called *form drag* and is induced by the difference between the high pressure in the front stagnation region and the low pressure in the rear separated region.

For bluff (relatively thick) bodies the form drag tends to be much larger than the frictional drag component and much research in aerodynamics has been devoted toward understanding how form drag is generated and developing methods for its reduction.

Of course, if the low rearward pressure in the separated region behind the body could be increased, then the form drag would be reduced. Thus, many recent efforts have been dedicated toward prediction of the pressure in this region. Unfortunately, as White [1] points out, boundary layer theory cannot accurately estimate the (usually low) pressure distribution in the separated region.

A common practical situation in which this problem arises is the flow around the trailing edge of a typical blade in the turbine section of an aircraft engine. Since the trailing edge is relatively thick to allow for blade cooling, the turbine blade can be considered as a bluff body (in comparison to a compressor blade). In addition, the flow in the trailing edge region of a typical turbine blade is highly viscous and transonic with complex shock structures. T.H. Moulden [2] mentions that, for these flows, "the inviscid flow solution will not be an adequate first approximation in many important situations".

In spite of these complications, the basic structure of the flow in the trailing edge region is well understood. The flow approaching the trailing edge separates on both sides of the turbine blade; this forms two shear layers which unite downstream at the *reattachment point*. Thus, a *dead air region* is formed immediately behind the trailing edge and between the two shear layers. The pressure in this region, the *base pressure*, is typically assumed to be constant throughout the dead air region. The strength of the trailing edge shock system, the rearward suction surface pressure distribution, and the mixing losses occurring downstream are strongly affected by the base pressure. Exactly how the losses are generated within the trailing edge region is not well understood. A knowledge of the base pressure, however, is essential for calculating the shock system, the viscous losses, and the flow rate of cooling air in the case of cooling injection at the trailing edge.

The present investigation attempts to experimentally determine the base pressure and its approximate distribution on the trailing edge of a turbine blade. The blade profile studied is typical of a turbine blade in the high-pressure turbine stage in a commercial aircraft engine. Due to the difficulty in instrumenting the thin trailing edge with static pressure taps, wind tunnel tests were carried out on a cascade of enlarged blades. Since the losses are strongly influenced by the base pressure, results are presented for both the base pressure and the aerodynamic losses of the turbine airfoil for a range of downstream transonic Mach numbers. The overall objective of this experiment is to extend the database of knowledge concerning base flows on turbine blades and to provide experimental data to compare with the output of current computer codes used in aerodynamic modelling. Ultimately, this should improve the methods in which the trailing edge flow region is modelled with these computational methods.

2.0 LITERATURE REVIEW

A relatively large amount of research and study of trailing edge flow fields has been taking place since the 1950's. Subjects such as base pressure, trailing edge loss, shock structure, coolant ejection effects, and trailing edge geometry effects have been analyzed with theories and experiments. The following chapter summarizes the significant past research efforts relating to the trailing edge flow in transonic turbine cascades.

2.1 Description of the Trailing Edge Flow Pattern

The basic pattern of transonic flow around the trailing edge of a blade profile is documented by several researchers and is currently well understood. Denton, et al. [3] provide a detailed account of the trailing edge flow field and their description is summarized here.

Figure 1 displays a schematic of a typical transonic flow field around the trailing edge of a turbine blade. For most cases of interest, the flow just upstream of the trailing edge will be supersonic on the suction surface and nearly sonic on the pressure surface. Immediately behind the trailing edge is an approximately triangular region bounded by two shear layers. The pressure within this *base region* is the base pressure and it is

typically assumed to be uniform around much of the trailing edge. The details of this region, however, can influence the flow over much of the rearward portion of the blade suction surface.

The flows coming from the suction and pressure sides of the blade initially undergo a Prandtl-Meyer expansion (regions 1 in Figure 1). The air is often overexpanded by this process and is quickly recompressed to the base pressure through a weak *separation shock*, or *lip shock* (lines 2 in Figure 1). For some cases, the Prandtl-Meyer expansion simply expands the flow to the base pressure. Near the beginning of the trailing edge curvature the flow separates on both sides, forming the shear layers (lines 3 in Figure 1) lining the base region.

At some point downstream the flows from the suction and pressure sides must meet and turn to a common flow direction. This region where the shear layers meet is commonly called the *confluence region* or *reattachment region*. The flow turning generates *reattachment shocks* which propagate into the flow (lines 4 in Figure 1). These shocks are also referred to as *wave shocks* or *trailing edge shocks* and are stronger than the separation shocks occurring near the base region. The trailing edge shock from the pressure side (line 5 in Figure 1) propagates toward the suction surface of the adjacent blade and interacts with its boundary layer; this shock strongly affects that blade's rearward suction surface pressure distribution. The other trailing edge shock moves downstream away from the blade row. Depending on the downstream Mach number, a vortex shedding pattern may occur downstream of the reattachment region.

Even though the basic flow pattern around the trailing edge is well understood, the base pressure is very difficult to predict. This is largely due to the highly viscous nature of

the flow field. The ability to theoretically predict the base pressure has been a continuing goal in trailing edge flow research.

2.2 Theoretical Models for Base Pressure Prediction

Over the past several decades, various analysis methods have been applied in order to approximate or predict the base pressure behind aerodynamic bodies. This section presents the fundamental ideas of these models and their specific application to cascade testing. Most of the methods can be grouped into three basic categories: backward facing step flow models, inviscid flow models, and Navier-Stokes computational codes. At the present time, it cannot necessarily be concluded that any one of these categories of base pressure models is better than others.

2.2.1 Backward Facing Step Flows

Figure 2 displays the basic features of the supersonic flow over a backward facing step. The model is representative of the flow on one side of the turbine blade approaching a blunt trailing edge with the separation point at the corner A and reattachment at a point B downstream of the step. The approaching supersonic flow expands and turns partially around the corner A. The region bounded by the triangle ABC contains the separated fluid moving in a clockwise recirculating pattern (although this is also referred to as the "dead air" region.) In order to turn back in the direction of the freestream, the flow is recompressed through a shock downstream of the reattachment point. This shock does not fully extend to the lower wall because the boundary layer flow close to the wall is subsonic and the compression process becomes continuous.

Tanner [4] has provided a good comprehensive review of the important backward facing step flow analysis methods. The most prominent of these methods is the Chapman-Korst model for steady, two-dimensional, turbulent flow. The model is essentially a boundary layer integral method and is applicable for supersonic approaching flows. The viscous mixing region in the vicinity of line AB in Figure 2 is assumed to have the same static pressure as the adjacent freestream and the mixing process occurring between the expansion and recompression regions is assumed to be isobaric. The expansion fan follows the Prandtl-Meyer function and, similarly, the flow conditions in the freestream determine the pressure increase in the recompression region (oblique shock wave). Finally, the conservation of mass is applied to determine the location of the reattachment point B in Figure 2. With these restrictions, a system of equations can be solved to obtain the base pressure (pressure along the wall AC). An exact analytical solution exists if the boundary layer approaching the step is assumed to be negligible.

Figure 3 displays the base pressure results for the theory (shown as "Korst" in the figure) in comparison with some experimental values for backward facing step flows. In the figure the base pressure coefficient (Cp_B) is the difference between the base pressure and the pressure just upstream of the step, normalized by the inlet dynamic pressure. For approaching freestream Mach numbers (M_∞) near 1.0, the Chapman-Korst theory overestimates the base pressure coefficient by approximately 30% of the experimental value; this overestimation is reduced for higher freestream Mach numbers.

Several authors have attempted to refine the Chapman-Korst theory using a different reattachment criterion. Nash [5] developed a method which takes into consideration

that the pressure at the reattachment point differs from the final recovery pressure downstream. This required a new parameter (N in Figure 3) based on empirical information to be introduced; this parameter is essentially a normalized pressure recovery. As can be seen in Figure 3, Nash's method predicted a base pressure coefficient approximately 30% lower than experimental values over most of the inlet Mach number range between 1.0 and 3.0. McDonald [6] divided the region of pressure rise at the end of the dead-air region into a region of isentropic flow reattachment followed by a region of rehabilitation of the newly attached boundary layer in the downstream direction. Both Nash and McDonald assumed a finite approaching boundary layer thickness. Thus, it appears that the assumption of negligible approaching boundary layer (Chapman-Korst) predicts a base pressure too high and the assumption of finite approaching boundary layer predicts a base pressure too low (Nash).

Tanner [7] has obtained good results for the base pressure coefficient; this can be seen in Figure 3. Tanner noted that the pressure drag in a steady separated flow will be generated through an energy loss of the main flow; this energy loss can be found in the flow downstream of the reattachment point (i.e. in the wake of the body). Thus, a connection exists between the maximum rate of outflow from the dead air region and the drag of the body. The base pressure can be found by equating the flow of entropy in the shear layer of thickness h (in Figure 2) to the entropy flow produced by the shock wave of projected length h^* (in Figure 2).

For applying any of these analyses to trailing edge flows, the model would actually need to be used twice (once for each side of the trailing edge) and conditions matched at the reattachment point. Inoue, et al. [8] have applied two of these models to study the flow around a blunt trailing edge of a turbine blade. The Chapman-Korst model with no

inlet boundary layer is compared to McDonald's method with a variable inlet boundary layer thickness. The results of both of these models are also compared with experimental results of a blade with a 70 degree stagger angle and design exit Mach number of 1.3. For the computation, the inlet flow on the suction side was supersonic and the inlet flow on the pressure side was sonic. The analysis shows an eight percent increase in the base pressure (normalized by the suction surface static pressure upstream of the trailing edge) with an increase in the suction side Mach number from 1.2 to 1.6; the authors attribute this to the wake deflection to the suction side on account of the interaction of the jet streams from each side of the blade. In addition, the (normalized) base pressure prediction of the Chapman-Korst model (with negligible inlet boundary layer) is actually eight percent higher than the predicted pressure from McDonald's model (with finite inlet boundary layer). This is in agreement with the results of the fundamental backward facing step flow model. The model also indicates the expected trend of increasing base pressure with increasing suction side boundary layer.

The research by Amana, et al. [9] is probably the best example of this flow model being applied for the study of trailing edge flow. They make the same basic assumptions of the Chapman-Korst model with adjustments made for a rounded trailing edge. The expansion fan is still assumed to be centered around a single point, but care is taken to determine the location of the separation shock (see Figure 1) by an oblique shock relation. The results indicate that the predicted base pressures are within five percent of the measured base pressures (from cascade experiments) for freestream Mach numbers near the trailing edge region between 1.4 and 1.9. The model is also able to predict the trailing edge shock wedge angle and the downstream flow angle.

Though the backward facing step flows have been used to predict the trailing edge pressure, some important differences exist between the model and the actual flow around a turbine blade trailing edge. In the backward step flow the separation point occurs at a known location; for a real trailing edge with continuous curvature, the location of separation must be solved for or assumed at a specified point. Another problem with the backward step model is that the lower wall would, at best, be represented by a free boundary in a real trailing edge flow. This lower wall is also not necessarily parallel to the upper wall in a real flow problem such as the case being studied. Korst [10], however, has provided experimental data for cases of backward step flows with inclined downstream walls. An additional assumption which is not truly satisfied in the model is the steady flow assumption since a vortex shedding pattern commonly occurs just downstream of the reattachment point. The vortex shedding, however, is not as severe for supersonic downstream flow, for which this model applies. In spite of these differences, both Inoue, et al. [8] and Amana, et al. [9] have obtained good agreement between experimental base pressures on a turbine blade and computed base pressures using these backward facing step models.

2.2.2 Inviscid Flow Models

Although numerous researchers have studied inviscid flow patterns over turbine blade profiles, very few have actually used an inviscid method to study the trailing edge region. Since the fluid in the base region has undergone separation, it would appear obvious that a viscous analysis should be employed for studying the trailing edge region. Indeed, this is true for any detailed study; a reasonable first approximation of base pressure (as well as loss), however, can be obtained with these inviscid models.

Gostelow [11] has developed a finite-difference potential flow model which can be used for a flows over turbomachinery blades. Since his calculation is one of the few inviscid models which gives careful attention to the trailing edge region, his model for the base flow is briefly discussed here. Gostelow placed several grid points on a rounded trailing edge and, to supply a trailing edge boundary condition, sought to locate the stagnation point. He found that moving the stagnation point by 0.15 percent of the chord from the center of the trailing edge results in a five degree change in the outlet flow angle. The location of the stagnation point also strongly affected the rearward pressure distribution on both the suction and pressure sides. Gostelow assumes that the presence of viscosity determines the actual stagnation point. By matching the static pressure coefficients from the suction and pressure sides, a unique calculated pressure distribution is obtained. He proceeds to use this method to predict the pressure distribution on a cusped airfoil. Bogod, et al. [12] have also applied an inviscid finite-difference method to cascade flows; the rounded trailing edges, however, had to be replaced by pointed edges. They found that the flow pattern near the trailing edge region depended significantly on the magnitude of the pressure at the exit of the calculation domain. This ought to be expected since the overall pressure gradient across the cascade drives the flow. Changing the pressure gradient will indeed change the flow pattern downstream of the throat (for choked flow).

Denton, et al. [3] have developed a control-volume Euler solution for cascade flows which can predict both the base pressure and the mixed-out loss. They note that, for an unstaggered cascade, "finite volume Euler solutions conserve these variables (mass, momentum, and energy) exactly and so should succeed in predicting the base pressure and loss even when the details of the flow around the trailing edge are inaccurate, due to shock smearing and the neglect of viscosity". Thus, by satisfying the conservation

equations of mass, momentum, and energy for a control volume, they were able to predict base pressure and loss for an unstaggered cascade of blades. Figure 4 shows the basic control volume model applied for both the staggered and unstaggered cascade. For a staggered cascade, a relationship between the base pressure and the average suction surface pressure downstream of the throat had to be initially guessed and then solved for by iteration using characteristics theory. The base pressure results for a staggered cascade of flat plates compared reasonably well to Sieverding's, et al. [16] correlation of the experimental data. Since the modelled cascade was not tested experimentally, however, it remains difficult to judge the true success of their method. MacMartin, et al. [13] have used a similar "mixed out" method to predict blade loss. Their calculation predicted a 21% total pressure loss, as compared to an experimental value of 28%. Denton, et al. [3] have also used their method to study the effect of suction surface curvature on the base pressure, noting an increase in base pressure for an increase in curvature for all transonic Mach numbers.

2.2.3 Navier-Stokes Solutions

There have only been a few attempts to study the viscous effects in the trailing edge region by attempting a numerical simulation of some form of the Navier-Stokes equations. C.C. Horstman [14] used the time-dependent, Reynolds-averaged, Navier-Stokes equations to study separated, asymmetric trailing edge flows in the transonic regime. Various two-equation turbulence models were used to study the effect of the turbulence modelling on the velocity profiles and boundary layer quantities. Good agreement among the various turbulence models was concluded. The trailing edge studied, however, was not representative of that of a typical turbine blade; instead, the

model was essentially a flat plate with curvature on one side leading to a sharp trailing edge.

A time-dependent, compressible Navier-Stokes simulation over two turbine blade designs was carried out by Dawes, et al. [15] to predict base pressures and blade losses. They employed a two-layer, eddy viscosity/mixing length turbulence model and specified transition to turbulence at a particular location on the blade. One of the turbine blades tested had a 50% thicker trailing edge. The computational model predicted base pressures which were, in general, lower than the experimentally measured values. The authors attribute this to the relatively simple turbulence modeling. The computation also revealed that the base pressure for the blade with the thicker trailing edge was insensitive to transition location on the blade surface; this was not experimentally verified. The blade with the thicker trailing edge showed lower base pressures for transonic outlet flow.

2.3 Experimental Research

Since the early 1970s, a continuing effort has been put forth in experimental research of the trailing edge flow field of transonic turbine blades. The following section summarizes the results of previous experimental research concerning the base pressure and the trailing edge losses of turbine blades. The primary focus for most of these studies has been to examine how changes in various parameters affect the base pressure.

2.3.1 *Effects of Blade and Cascade Geometry*

A series of studies carried out at the Von Karman Institute for Fluid Dynamics has resulted in the development of a well-known base pressure correlation by Sieverding, et al. [16]. This correlation assumes that the base pressure (p_B) is a function of the upstream total pressure (p_{t1}) , the downstream static pressure (p_2), and the blade geometry. Seven parameters are identified which characterize the blade geometry: (1) incidence angle, β_1; (2) shape of the blade channel upstream of the throat; (3) trailing edge thickness, *te*; (4) "gauging angle" of the tailboard (used to generate a shock-boundary layer interaction on the model); (5) trailing edge wedge angle, δ; (6) angle, ϵ, between the tangents to the suction surface in the throat and at the trailing edge; and (7) area ratio A_{te}/A^* of the supersonic part of the blade channel in the case of convergent-divergent bladings. Due to limited amount of data, Sieverding does not use all of these parameters in the correlation. The correlation ultimately assumes the form:

$$p_B/p_{t1} = \text{fn}(p_2/p_{t1},\ ½(\delta+\epsilon)) \quad \text{Convergent Blades}$$

$$p_B/p_{t1} = \text{fn}(p_2/p_{t1},\ A_{te}/A^*) \quad \text{Convergent/Divergent Blades}$$

Using data from 16 different cascades, a graphical correlation of the above functional forms is constructed; this correlation is shown in Figure 5. (Note: Sieverding's exit static pressures, p_2, for these cascades were measured at 40% to 60% of the chord length downstream of the trailing edge.) The correlation is applicable to cascades before the limit loading condition is reached. The limit loading condition occurs when the pressure side trailing edge shock extends out beyond the trailing edge of the next blade; thus, the flow around the blade surface is unaffected by lowering the back pressure downstream. A schematic included in Figure 5, however, shows how the base

pressure behaves near the limit loading condition. The correlation shows a base pressure which is lower than the downstream pressure for most of the geometric configurations.

Several recent experiments have indicated base pressures higher than those predicted by the correlation. Doughty [17] has compared experimental base pressures with Sieverding's correlation for three different values of $\frac{1}{2}(\delta+\epsilon)$; the measured base pressures were slightly higher than predicted. Xu, et al. [18] have also predicted higher base pressures. The axial position where the downstream pressure is measured may have an effect on the differences among the results of the correlation and the experiments.

Since the development of Sieverding's correlation, attempts to study geometric changes which were originally excluded from the correlation have been made. Experiments by Dawes, et al. [15] have shown that a 10 degree increase in the incidence angle, β_1, substantially increases the base pressure for supersonic downstream Mach numbers. In addition, the effect of trailing edge thickness, *te*, on base pressure and losses has been studied thoroughly. Xu, et al. [18] have noted that the trailing edge loss is directly proportional to the trailing edge thickness, with a greater constant of proportionality at transonic and supersonic speeds. Denton [19] has provided a good review of correlations which consider trailing edge thickness in predicting profile losses. Zeidan [20] concluded that the trailing edge thickness mainly effects the trailing edge shock strength, noting a 20 to 30 percent increase in loss over the range, $1 < M_2 < 1.2$, for a 57% thicker trailing edge.

A paper by Kiock, et al. [21] has shown that even the tunnel environment can have an effect on measured losses. They note that the tunnel environment includes factors such as inlet flow development and blockage due to measurement probes. After testing the same cascade in four different wind tunnels, they found that the surface Mach number distributions differed considerably in the rear half of the suction side. The results indicated slight shifts in the base pressure coefficient (base pressure normalized by downstream dynamic pressure) for the different wind tunnel tests. They also noted that the loss and exit flow angle were not strongly affected by changes in the axial velocity density ratio between 0.9 and 1.0.

A few researchers have documented the effect of Reynolds number on the base pressure in transonic flow. Wind tunnel tests in which the Reynolds number can be varied independently of the freestream Mach number provide the best source of data for these experiments. Motallebi, et al. [22], in studying vortex shedding off the base region of a model resembling a flat plate, were able to vary the Reynolds number (based on chord and freestream conditions) between 1.6×10^6 and 2.8×10^6 for a freestream Mach number of 0.6. In this range, the effect of Reynolds number on base pressure was negligible. Paige [23], however, has found that, by changing the Reynolds number of a transonic turbine blade from 7×10^5 to 3×10^5 for constant Mach number, the base pressure increased significantly while the momentum thickness near the trailing edge remained nearly the same.

2.3.2 Details of the Flow Region

A large amount of research in trailing edge flows has not only been concerned with the determination of the base pressure, but has also been involved with some of the finer

details of the flow region. Such details include the base pressure distribution, the strength of the separation shock, the effect of the boundary layers near the trailing edge, the nature of the confluence region, the downstream flow angle, and the periodic vortex shedding.

Sieverding, et al. [16,24] have carried out an experimental determination of the base pressure distribution for a turbine profile. Due to the difficulties in instrumenting a thin trailing edge with many pressure tappings, a model which simulated the overhang section of a convergent cascade was developed. The model consisted of a single flat plate with 19 pressure tappings at different angular positions around the rounded trailing edge; the wind tunnel walls around the flat plate were curved to simulate the flow through the rearward portion of a turbine profile. The pressure side Mach number at the trailing edge was 1.02, remaining constant for all tests. For limit loading conditions, the pressure around the trailing edge was uniform over the central 100 degrees for trailing edge suction side Mach numbers between 1.0 and 2.3. To simulate part load conditions, a tailboard was used to generate a shock-boundary layer interaction on the suction surface. The reflected shock, however, returned to the tailboard and reflected again, interacting with the downstream wake region. The measured pressure distribution was still very uniform over the central 100 degrees of the trailing edge. The results indicate that the base pressure for flows with shock impingement on the suction surface (part load) were higher by 10 to 25% of the base pressure without shock interference (limit loading).

Sieverding, et al. [16] have also determined the strength of the separation shock. The shock strength appears to be the same for either side of the trailing edge, with a pressure ratio of 1.15 $\pm$ .05. Amana, et al. [9], using angle measurements from a

Schlieren photograph on the same experimental setup, have reported a Mach number ratio of 0.81 ± .02 across the separation shock. At least one of these values is incorrect, for these pressure and Mach number ratios cannot be accomplished with even a normal shock.

The boundary layer parameters near the trailing edge have also been studied by a few researchers. Xu, et al. [18] and Sieverding, et al. [24] have noted that the boundary layer shape factor at the trailing edge is believed to have a significant influence on the mixing process. This has been difficult to verify experimentally, but Mee, et al. [25] have provided detailed measurements of the displacement thickness (δ^*), momentum thickness (θ), and shape factor (H) at 99% of the axial chord (C_{ax}) for exit Reynolds number of 10^6. For downstream Mach numbers increasing from 0.7 to 1.2, the shape factor increased from 1.5 to 2.1 and the mixing loss (normalized by a reference kinetic energy loss value) increased from 0.4 to 1.1. The computations of Xu, et al. [18] are in good agreement with these values.

The nature of the confluence region (reattachment region) has been a concern for checking the validity of the base pressure flow models as well as the experimental correlations. Several experiments have indicated base pressures that deviate from Sieverding's [16] correlation, which uses the downstream pressure, p_2, as a reference pressure. Bölcs, et al. [26] therefore sought a new reference pressure to correlate their cascade data. They attempted to develop a correlation to find the base Mach number from the Mach number at the recompression point. The recompression Mach number, however, has to be found from the method of characteristics and the correlation is only good above Mach numbers near 1.1. Motallebi, et al. [22] showed that the confluence region moves downstream as the freestream became more supersonic. Sieverding, et al.

[16,24] have studied the pressure distribution along the wake centerline just downstream of the trailing edge. They note that the pressure recovery zone is much longer than the isobaric dead water region at the trailing edge; this suggests a revision of the base pressure theories (specifically, the isobaric mixing assumption).

The inclination of the exit flow has been documented by Kiock, et al. [21] for transonic downstream Mach numbers. In the subsonic range, increasing the downstream Mach number resulted in the flow direction moving slightly toward the pressure side. In the supersonic range, the flow turned back strongly toward the suction side for increasing Mach numbers. The results of Xu, et al. [18] indicate the same behavior of the exit flow angle. Mee, et al. [25] carried out wake traverses near the trailing edge to obtain the flow angle variation across the wake for different axial positions downstream of the trailing edge. Initially, at 3.2 trailing edge diameters downstream, a difference of nearly 30 degrees in flow angle exists on either side of the wake centerline. As mixing occurs, the flow angle becomes more uniform downstream.

The periodic vortex shedding pattern downstream of the trailing edge is also related to the base pressure. Dawes, et al. [15] noted that the base pressure and the near-wake region are strongly influenced by vortex shedding for subsonic exit velocities. This vortex shedding became suppressed for supersonic exit velocities. Bölcs, et al. [26], however, indicated that in the range, $0.8 < M_2 < 1.2$, the base pressure is periodically unsteady, oscillating at the fundamental frequency of the alternating vortex system emerging from the trailing edge. This frequency depends on the Reynolds number. Most of the research concerning vortex generation from the base region has been in the context of coolant ejection from the trailing edge.

2.3.3 *Effects of Trailing Edge Coolant Ejection*

One important reason for the knowledge of the base pressure is to compute the amount of coolant flow for blades with trailing edge coolant ejection. Studies have revealed, however, that the presence of coolant flow substantially alters the base pressure. MacMartin, et al. [13] noticed that the base pressure coefficient, Cp_B, increased from a negative 30% to near 0% by increasing the cooling mass flow rate from 0% to 7% of the mainstream mass flow rate (per passage). (This coefficient, Cp_B, is the difference between the base pressure, p_B, and the downstream pressure, p_2, normalized by the downstream dynamic pressure.) Surprisingly, this increase in base pressure had no significant effect in reducing the losses. Xu, et. al [18] indicate that even though trailing edge ejection can significantly increase the base pressure, the additional loss suffered by the ejected fluid may not compensate for the reduction in the trailing edge loss. Bertsch [27] studied the effects of trailing edge coolant ejection on losses; he concluded that the effect of ejection on the total pressure losses is not large and that the ejection does not affect the trailing edge shock strength or surface pressure distribution. The ejection may have had a small effect on the shock angle.

The effect of coolant ejection on the vortex shedding pattern from the base region has been studied in great detail. The work of Motallebi, et al. [22] determines the relationship between the base pressure and vortex shedding for different rates of coolant ejection through the trailing edge of a flat plate. The minimum base pressure for a slotted trailing edge with no ejection was slightly lower than the minimum base pressure for a solid trailing edge. For no blowing, the minimum base pressure occurred at the maximum Strouhal number, St (vortex shedding frequency×base height/mainstream flow velocity); the freestream Mach number for this case was 1.18. The trailing edge

shocks were found to oscillate at the frequency of the vortex shedding for zero bleed. At $M_\infty = 1.03$ a small amount of bleed air led to an increase in the base pressure and a rearward displacement of the confluence region. Upstream of this region, there was no evidence of vortex motion. At $M_\infty = 1.30$, the initial rise in base pressure was small compared with the transonic case; the Strouhal numbers were approximately 20% higher for this higher Mach number.

Sieverding [28] also studied the effects of trailing edge ejection on the base pressure and vortex shedding. He showed that the maximum base pressure rise from coolant ejection can be as high as 15% of the downstream dynamic head at transonic and low supersonic outlet Mach numbers. He mentions that the "maximum base pressure occurs when the momentum of the coolant flow is just about strong enough to overcome the adverse pressure gradient." [28] Three regimes of bleed air injection are identified: (i) low injection, the coolant is entrained by the trailing edge vortices; (ii) moderate injection, the vortex sheet is delayed downstream; (iii) high injection, the coolant rate is comparable to the main flow's rate, vortices are shed between the two streams. The effect of the density ratio of coolant to main fluid does not greatly change the base pressure level until relatively high amounts of coolant are ejected.

2.3.4 Remarks

At this point, no literature has been found in which the base pressure on an actual turbine profile has been measured with more than a single tap in the trailing edge (or two taps in the case of coolant ejection). Sieverding's [16,24] pressure distribution model (with 19 taps) represents a turbine profile with zero trailing edge wedge angle ($\delta=0$) downstream of the throat. Since most real turbine blades have a finite wedge

angle, the present experiment attempts to measure the base pressure on a typical turbine profile with more than one tap in the trailing edge. In addition, this experiment does not study the effects of coolant ejection on base pressure; however, it is recommended for future study.

3.0 EXPERIMENTAL METHOD

The following chapter describes the testing facility, the experimental setup, and the data reduction techniques to determine the important flow quantities.

3.1 The Wind Tunnel Facility

The cascade was tested at the VPI & SU transonic wind tunnel, a blow-down type facility. The important details of the wind tunnel have been included in this section; References [20], [27], [29], and [30] discuss the facility in further detail.

3.1.1 Overall Features

The air to the wind tunnel is supplied by two storage tanks; these storage tanks are fed with dry air by a four-stage, reciprocating compressor in line with a heat exchanger (to cool the air) and an activated-alumina dryer. The air is delivered to the tunnel section from the storage tanks through a 14 in. (35.6 cm) diameter pipe. A safety valve and a control valve allow the flow to enter into the cascade section at constant total pressure. Figure 6 shows the cascade tunnel section downstream of the valves. The flow coming from the valves passes through a 90 degree bend which is followed by a flow

straightener consisting of an array of 0.875 in. (22.2 mm) diameter tubes. Following the flow straightener, the transition piece reduces the tunnel width to the blade span of 6 in. (15.2 cm). The flow then passes through the test section and exits to the atmosphere through a diffuser and a muffler. Recently, a heat exchanger (shown in Figure 6) has been installed in line with the piping ahead of the test section so that the upstream total temperature can be varied in the cascade tunnel.

3.1.2 Supply Pressure Control

The time required to run the wind tunnel and collect the necessary data in a given run is approximately 18 seconds. In order to maintain a constant upstream total pressure during this time, a control valve with a computerized feedback circuit is used. This valve is a butterfly valve which opens and closes by means of a pneumatic system. A personal computer is used to supply a voltage signal to an electro-pneumatic converter, fed with pressurized air at 20 psig (138 kPa, gage); the electro-pneumatic converter produces a proportionate output pressure based on the input voltage arriving from the computer. The output pressure opens the valve in such a manner as to maintain constant upstream total pressure, p_{t1}, for the 18 second run time. The feedback circuit corrects the voltage output from the computer during this time to open or close the valve, as necessary, to maintain constant p_{t1}. The voltage signal from the computer is described with seven constants; some of these constants are changed with each run to generate a different downstream Mach number. Bertsch [27] discusses how these constants construct the voltage signal. The other valve used during the experiment, a safety valve, is simply opened and closed with an 8.0-volt source with each run.

3.2 Description of the Cascade

Due to the necessity for placing multiple static pressure taps in the trailing edge, a large scale model of the actual engine blade is required for the test. The design outlet Mach number for the engine blade is 1.20. The model turbine blade is five times the size of the actual blade and is based on its mid-span profile. Because of wind tunnel constraints, the model blade is designed for the flow to approach at zero relative inlet angle ($\beta_1 = 0$); the actual blade has an inlet angle of 55°. Both blades have the same exit angle: $\beta_2 = -67°$. The difference in the shapes of the two blade designs is shown in Figure 7. The rearward half of both blades are essentially the same.

The trailing edge thickness, *te*, of the large blade is 0.126 in. (3.20 mm), which is 1.94% of the chord. The trailing edge wedge angle, δ, for this blade is 8.5° and the suction side turning downstream of the throat, ϵ, is 9.6°. (These values are important for comparison with Sieverding's correlation.)

The dimensions of the large-scale blade are shown in Figure 8; the lower blade pictured displays the orientation of the blade as it is situated in the cascade. Figure 9 indicates the dimensions of the basic cascade parameters: pitch (P), chord (C), span (S), and throat (T). A more detailed list of the geometric features for the large-scale cascade is shown in Tables 1 and 2.

In order to evaluate the results obtained from the large-scale blade, it would be of interest to compare these results with cascade data from a blade more similar (in size) to the engine blade. For these reasons, data from previous wind tunnel tests on a smaller blade, referred to as "Baseline", are included in the results. The Baseline blade

has the same shape as the large-scale blade; the dimensions of the Baseline blade, however, are 0.30 times the dimensions of the large-scale blade. (Thus, the Baseline blade is 1.5 times the size of the engine blade).

The Reynolds number (based on the axial chord and the upstream conditions) for the large scale blade at the design exit Mach number ($M_2 = 1.2$) is 8.3×10^5. The Reynolds number for the Baseline blade at the same Mach number is 2.6×10^5.

Due to the large size of the blades, the experimental cascade contains only three blade passages. The frame of the cascade is two Plexiglass endwalls with the blades mounted in between them by a screw and a pin on each side. In addition, an endblock is placed above the top blade to help seal the cascade when placed in the wind tunnel. Although the top and bottom blades are not full blades, they are used to help form the blade passages. Figure 10 displays a profile of the fully-assembled cascade along with the x and y reference directions. The blades are numbered 1 to 4, starting from the bottom. To minimize shock reflections, a tailboard was not installed for the experiment. The blades do not contain any cooling passages.

3.3 Experimental Measurements

Doughty [17] provides a good summary of the data which is of interest for each run: the atmospheric pressure, p_{atm}; the upstream total pressure, p_{t1} (as a function of time); the total pressure difference, Δp_t (p_{t1}-p_{t2}); the downstream static pressure, p_2, at the beginning of each run; the upstream total pressure at the instant p_2 is measured, p_{t1i}; the static pressures on the blade surface; and the shadowgraph pictures. Two other variables are measured essentially for "monitoring" purposes: the upstream total

temperature and the upstream relative humidity. These conditions are checked to ensure they remain approximately constant from one run to the next (and, thus, are not a source of scatter in the data).

3.3.1 The Measurement System

A schematic of the entire measuring system is shown in Figure 11. A barometer is used to measure the atmospheric pressure at the beginning of the series of wind tunnel runs. The upstream total pressure, p_{t1}, is measured with a simple tube pointed into the flow and mounted upstream of the cascade in one of the test section doors. The probe is connected via plastic tubing to two transducers: a gage pressure transducer used for measuring p_{t1} and a differential pressure transducer for measuring p_{t1}-p_{t2} (Δp_t). The other input to the differential pressure transducer, p_{t2}, is measured with a traversing total pressure probe which traverses 1.5 blade passages during a run. The probe, which is driven upwards by a stepper motor, is placed at mid-span behind the cascade at the same axial position as the wall static pressure taps (Figure 10). The signals for p_{t1} and Δp_t are read simultaneously by a data acquisition computer, which records 800 data points for each of the two pressures during the 18 second run time. The two transducers are calibrated daily by applying pressure to each transducer with a deadweight tester and checking the voltage output with a calibration curve.

The downstream static pressure distribution, p_2, is measured at the endwall static pressure taps by a separate data acquisition system. These taps are located 0.828 in. (2.10 cm) or 16.7% of axial chord downstream of the cascade (Figure 10). A total of 31 pressures are measured at these endwall taps; the lower 21 taps are placed behind the second blade from the bottom (blade #2 in Figure 10) and the upper 10 taps are placed

behind the third blade (blade #3) from the bottom. The lower taps are spaced every 5% of the blade pitch (.245 in. or 6.2 mm) and the upper taps are spaced every 10% of the pitch (.490 in. or 12.4 mm). The data acquisition system which measures the 31 endwall pressures is referred to as the 32-channel PSI system. This system is self-calibrating and it is controlled by a personal computer (labeled "Control PC" in Figure 11) which records the gage pressures in a data file. The control PC also runs the stepper motor for the downstream traverse mechanism and records the data from the data acquisition PC. The first 31 channels in the PSI system measure the endwall static pressures and the 32nd channel measures the upstream total pressure, p_{t1i}, from the same probe used to measure p_{t1}. Five sets of the 32 pressures are recorded during each run; for each set, a particular static pressure reading is an average of 50 measurements taken over 0.5 seconds. The first set is used to calculate the isentropic Mach number behind each of the two blades for each run.

The upstream total temperature is measured with an OMEGA, type K thermocouple and the relative humidity is measured with an OHMICO polymer resistive humidity sensor. Both the temperature and humidity are measured well upstream of the blades.

3.3.2 Trailing Edge Instrumentation

A second 32-channel transducer in connection with the PSI system is used to measure static pressures on the blade surface. A total of ten static pressure taps were placed on the surface of the large-scale blade #2: five taps were placed on the rearward portion of the suction surface to measure isentropic Mach numbers approaching the trailing edge and five taps were placed around the trailing edge to measure the base pressure. From the tap positions, copper tubes were placed in the blade surface and led out

through the endwalls. The five suction side tap positions are shown in Figure 12 and the five trailing edge tap positions are shown in Figure 13.

The five trailing edge taps are not located at the same spanwise position; instead, they are spaced uniformly over the central one inch of the span. Each of the taps was drilled with a 0.020 inch (0.51 mm) diameter drill bit. When compared with the relative size of the trailing edge, each tap takes up 10.6% of the trailing edge arc length (about 18 degrees). For this reason, the pressure data reported from these taps are representative of an average pressure over that 18-degree interval.

3.3.3 Photography

Figure 14 displays the basic experimental setup for the shadowgraph method of flow visualization. A strobotac was used for the light source since it provided flashes with strong intensity. This is necessary in order to magnify the trailing edge region with a sufficient amount of light. The focal lengths of the first and second mirrors are, respectively, 6.56 ft. (2.0 m) and 2.50 ft (0.762 m). After the light passes through the cascade and refocuses onto a plane mirror, the light expands onto the film. The pictures are taken with the fast, type 57 Polaroid film.

3.4 Assumptions

The following assumptions are made in order to carry out the data reduction techniques described in the next section.

- The atmospheric pressure remains constant during the day in which the series of runs are carried out.

- The total temperature is constant throughout the blade row over the entire run. The assumed value is $T_t = 283$ K.

- The static pressures measured at the endwall are equivalent to the static pressures at mid-span of the cascade tunnel section.

- The traversing probe travels at constant speed throughout the run.

- In the case of supersonic downstream flow, the static pressure ahead of the bow shock on the traversing probe is equal to the endwall static pressure.

- The exit Mach number is calculated assuming isentropic flow through the blade passages ($M_2 = M_{2is}$).

- The flow is assumed to be two-dimensional and periodic behind the blade row at mid-span.

- The flow angle downstream of the blade row is assumed equal to the blade angle, $\beta_2 = -67^\circ$.

- The cascade flow is assumed to be that of dry air at standard conditions.

- The upstream relative humidity is constant throughout the run.

- The inlet conditions (p_{t1}, M_1) are uniform over time and space.

3.5 Data Reduction

Two base pressure coefficients are reduced from the raw data. Since the PSI system records the measured pressures as gage pressures, these coefficients are fairly easy to compute. The first coefficient, p_B/p_{t1}, is computed in the following manner: the atmospheric pressure is added to the average of the gage pressures measured from the three central trailing edge taps to find p_B; this result is divided by the sum of the atmospheric pressure and the gage pressure at the PSI port connected to the upstream total pressure probe. (The reason for averaging the three central trailing edge taps is discussed in Section 4.1.2.)

The second base pressure coefficient is a measure of the difference between the base pressure (p_B) and the exit pressure (p_2). This coefficient, Cp_B, has been defined by Kiock, et al. [21] as

$$Cp_B = \frac{p_B - p_2}{\frac{1}{2}\rho_2 U_2^2}$$

where p_2 is the area-averaged exit static pressure, averaged from the output of the 21 taps behind blade #2 in the cascade. The dynamic pressure in the denominator of the Cp_B expression can be simplified using the ideal gas law; the expression then becomes

$$Cp_B = \frac{2}{\gamma M_2^2}\left[\frac{p_B}{p_2} - 1\right]$$

where M_2 is determined from the isentropic relation: $M_2 = \text{fn}(p_2/p_{t1})$ and γ is the specific heat ratio for air. For the remainder of the thesis the first coefficient, p_B/p_{t1}, is referred to as the "normalized base pressure" and the second coefficient, Cp_B, is referred to as "the base pressure coefficient".

Since base pressure studies on turbine airfoils are typically carried out in the context of predicting and/or reducing the generated losses, an important part of this experiment is to quantitatively measure the aerodynamic losses. The data obtained from the methods described above is used to calculate the mass-averaged total pressure loss, L, as a function of the exit Mach number, M_2. Assuming uniform inlet flow conditions, the loss can be expressed by

$$L = \frac{\int_0^1 \frac{[p_{t1} - p_{t2}]}{p_{t1}} \rho_2 u_2 dy}{\int_0^1 \rho_2 u_2 dy}$$

where $0 \leq y \leq 1$ represents one blade pitch and the velocity, u_2, is the x-component of the velocity behind the blade row. Since 526 discrete measurements are taken over one blade pitch to compute the loss, a better representation of the above equation is

$$L = \frac{\sum_{ji}^{ji+526} \frac{[p_{t1j} - p_{t2j}]}{p_{t1j}} \rho_{2j} u_{2j}}{\sum_{ji}^{ji+526} \rho_{2j} u_{2j}}$$

where the j values represent the y-position of the traversing probe at an instant a measurement of Δp_t is made and ji is the initial starting position of the probe.

The first task in the computation is to determine a value of the wall static pressure, p_{2j}, which can be associated with each measured Δp_{tj}. Since five measurement sets of the wall static pressure are taken over the 18 second interval, the loss computation method presented here attempts to include variation in static pressure which may occur over time. Thus, the correct value of the local, instantaneous wall static pressure, p_{2j}, is estimated by interpolating in both time and distance. A portion of the output data of the traversing probe corresponds to *y*-locations below the lowest endwall tap. In this case, periodicity is assumed and the wall static pressures located at one pitch above these points are necessary for the computation.

In order to find the downstream total pressure at the traversing location, p_{t2j}, it is necessary to see if a bow shock exists at the probe inlet. If $p_{2j}/p_{t1j} > 0.528$, then the flow approaching the probe inlet is subsonic and p_{t2j} is simply $p_{t1j} - \Delta p_{tj}$. If the above inequality is not true, the flow is supersonic and a bow shock correction must be applied. At this point, the known values are the static pressure upstream of the bow shock (p_{2j}) and total pressure downstream of the shock (p_{t1j}-Δp_{tj}). Since the true downstream total pressure is the pressure ahead of the bow shock, an initial guess of this pressure must be made and an iterative solution applied until the normal shock relations hold true. This reveals the true downstream Mach number (M_{2j}) and the true downstream total pressure (p_{t2j}). This procedure is carried out for each value of *j*.

The density, ρ_{2j}, and the velocity, u_{2j}, can be evaluated once the static temperature, T_{s2}, is known. This is easily found from the Mach number relation:

$$T_{s2j} = \frac{T_{t1}}{\left[1+\frac{1}{2}(\gamma - 1) M_{2j}^2\right]}$$

where γ is the specific heat ratio of air. Then, the density and velocity are evaluated by the relations,

$$\rho_{2j} = \frac{p_{2j}}{RT_{s2j}}$$

and

$$u_{2j} = M_{2j} \cos(\beta_2) \sqrt{\gamma RT_{s2j}}$$

where R is the ideal gas law constant for air.

For convenience, an isentropic downstream Mach number is also computed for each run. This is obtained by spatially averaging the wall static pressures behind one of the blades for the first of the five data sets taken and dividing by the upstream total pressure to obtain p_2/p_{t1}. The instantaneous, isentropic downstream Mach number is then:

$$M_{2is} = \sqrt{\frac{2}{\gamma - 1}\left[\left(\frac{p_2}{p_{t1}}\right)^{\frac{\gamma-1}{\gamma}} - 1\right]}$$

The isentropic Mach number calculated behind blades 2 and 3, in addition to wake traverse plots, can be used as a check of the periodicity behind the blade row. The results for the loss are presented with the isentropic Mach number as the independent variable. From here on, the notation M_2 refers to the isentropic exit Mach number and is simply called the "exit Mach number" or the "downstream Mach number".

The loss measurements reported in this thesis were taken before the blades were instrumented with static pressure taps. The blade surface static pressures were

measured later in a separate series of runs and, due to time constraints, the loss measurements were not carried out in the same set of runs.

3.6 Comments on Data Presentation

The experimental method discussed above in Section 3.5 assumes that the loss coefficient, L, computed from the experimental data is essentially a function of the downstream Mach number, M_2. Similarly, most base pressure analyses (Section 4.1.2) assume that the base pressure, p_B, is also a function of M_2 (or p_2/p_{t1}). Since all of these variables (p_B, L, M_2) are essentially dependent upon p_{t1}/p_{atm} and the cascade geometric parameters, then it is possible to develop correlations where one of these variables is a function of one of the other two variables (for the same cascade geometry). For consistency with much of the literature, however, M_2 is treated as the major "independent" variable throughout this thesis.

4.0 EXPERIMENTAL RESULTS

The results for the measured blade surface pressures and the computed loss for various downstream transonic Mach numbers are presented in this chapter. Other experimental results are presented in order to check the validity of the important assumptions made in the experiment. The shadowgraph pictures are also discussed.

4.1 Base Pressure

The base pressure results are displayed in two basic forms: plots indicating the pressure at different positions around the trailing edge, and plots showing the overall base pressure as a function of a measured downstream parameter, such as pressure or Mach number. The numerical output for the normalized base pressures, p_B/p_{t1}, for each angular position and Mach number is shown in Tables 3 and 4.

4.1.1 Base Pressure Distribution

Five pressure measurements were taken at various positions (Figure 13) around the trailing edge of blade #2 in the cascade. These pressures were measured simultaneously at the beginning of each run. Figures 15 through 17 summarize the output of

these measurements with plots of the measured pressure as a function of the angular position around the trailing edge. Negative angular values shown in the figures correspond to the pressure side of the blade.

The pressures measured from the central three taps are nearly equal to one another for each of the downstream Mach numbers. This pattern remains true for nearly all of the downstream Mach numbers tested. These results are in basic agreement with the pressure distribution studies of Sieverding, et al [16,24] in which they found a nearly constant pressure around a large portion of the trailing edge. Their different pressure distribution curves arise from changes in the "gauging angle" which is correlated to the suction surface Mach number near the trailing edge. For convenience, the base pressure curves in Figures 15 through 17 are referenced to different downstream isentropic Mach numbers, M_2.

Figure 15 shows the base pressure distribution curves for subsonic exit Mach numbers. The shape of each curve remains consistent with the increasing values of M_2. The approaching flow from the pressure side increases its pressure in order to meet the base pressure. A "smaller" pressure rise is measured from the two tap positions on the suction side; this does not necessarily say that the pressure rise near the suction side is smaller than the pressure-side pressure rise for the taps are not uniformly spaced. The angular difference between the two taps near the pressure side (38°) is slightly larger than the angular difference between the taps on the suction side (32°). These pressure rises are most likely a result of the separation shocks on both sides of the trailing edge.

As the downstream Mach number is increased into the supersonic range, the pressure distributions observed in Figure 15 slowly begin to change. This is shown in Figure 16.

Near $M_2=1.15$, the pressure rise measured from the two pressure side taps begins to diminish and by the time $M_2=1.22$, a small drop in pressure is observed. Thus, near $M_2=1.2$, the pressure-side flow appears to expand to the base pressure without recompression. The suction side pressure rise to the base pressure remains nearly the same as in the subsonic case. The pressure distribution measured from the central three taps continues to be uniform as the exit Mach number is increased. The base pressure remains constant for exit Mach numbers just above 1.0, which is when the trailing edge shock system is being formed.

Figure 17 indicates the pressure distributions around the trailing edge for cases where the exit Mach number exceeds its design value of 1.2. For values of M_2 greater than 1.25, the base pressure level no longer continues to fall with increasing exit Mach numbers. Figure 17 also shows the base pressure level (from the three central taps) well below the pressure measured from the -83° tap position. In fact, the measured p/p_{t1} at this position has appeared to reach a minimum value near 0.37 (corresponds to an isentropic Mach number of 1.28). Any further increases in the downstream Mach number do not lower the measured pressure at this position. Figure 18 displays how the pressure measured at -83° continues to drop until exit Mach numbers above 1.2 are obtained. This position on the blade may correspond to a point near the throat of the choked flow in the cascade.

In summary, the above results indicate a uniform pressure distribution around at least the central 90 degrees of the trailing edge. The level of this pressure falls with increasing downstream Mach number until M_2 is near 1.25. The outer tap on the suction side consistently measures a pressure lower than the pressures measured by the central three taps. The outer tap on the pressure side (-83°) measures a pressure lower

than that measured by the central three taps for exit Mach numbers below 1.2. Above this Mach number, the base pressure falls below the value measured by this tap, which remains constant at $p/p_{t1} \cong 0.37$.

4.1.2 Base Pressure Plots

Most of the experiments concerning trailing edge flows have not been concerned with base pressure distribution. This is partly due to the difficulty in placing multiple taps in the trailing edge region. Moreover, the works of Sieverding [16,24], as well as this experiment, have indicated a nearly constant base pressure around much of the trailing edge. For these reasons, it is common to identify the "base pressure" as the average pressure around most of the trailing edge and it is typically measured with a single tap. Since the central three taps indicated nearly equal pressures in this experiment, the average of these three pressures will be termed the "base pressure", p_B, for the figures cited in this section.

Figure 19 displays one common way of presenting base pressure data, in which the normalized base pressure, p_B/p_{t1}, is assumed to be a function of the downstream pressure, p_2/p_{t1}. This plot can be compared with Sieverding's [16] correlation in Figure 5. The value of the parameter, $\frac{1}{2}(\epsilon + \delta)$, for the large scale blade is 9°. The curve corresponding to this value is included in Figure 19. Sieverding's correlation does not indicate the variations in the base pressure occurring in the domain, $0.3 < p_2/p_{t1} < 0.4$, in Figure 19. The figure also indicates that, for most of the exit Mach numbers tested, the experimental results display base pressures higher than those given by the correlation. Thus, some of the parameters which Sieverding left out of the correlation may be important for base pressure prediction.

In order to compare the base pressure results with the downstream Mach number, Figure 20 replots the data of Figure 19 with the isentropic exit Mach number as the abscissa. Using Figure 20 the behavior of the base pressure can be seen for different M_2 regimes. In the range $0.70 < M_2 < 1.00$, the base pressure falls almost linearly from $p_B/p_{t1} \simeq 0.71$ to $p_B/p_{t1} \simeq 0.54$. The base pressure remains nearly constant at this value until $M_2 \simeq 1.05$; at this point, the flow on the suction surface near the trailing edge is becoming supersonic. For $1.05 < M_2 < 1.20$, p_B falls rapidly to $p_B/p_{t1} \simeq 0.35$; during this time a reflected oblique shock is increasing in strength as it moves down the blade suction surface away from the throat. Increasing the exit Mach number, the base pressure falls slowly to its minimum value at $p_B/p_{t1} \simeq 0.30$ at $M_2 = 1.30$. A further increase in the exit Mach number results in a base pressure increase to $p_B/p_{t1} \simeq 0.35$ at $M_2 = 1.38$. The results of the suction surface pressure distribution in section 4.3 may help explain this base pressure behavior.

Another common method of presenting the base pressure data (Kiock, et al. [21]) is to plot the base pressure coefficient, Cp_B, as a function of the downstream Mach number, M_2. A plot of the base pressure coefficient as a function of the downstream Mach number is shown in Figure 21. Since the difference between p_B and p_2 is small compared to the magnitudes of these pressures, the effect of scatter in the data becomes more pronounced on this type of plot. In spite of the data scatter, a base pressure correlation may be easier to determine with this plot than with the previous two types. The plot shows essentially two regimes: a region of constant Cp_B for subsonic exit Mach numbers and a nearly sinusoidal curve for the range of supersonic exit Mach numbers tested. An approximate fit of the data could be represented by:

$Cp_B = 0.040$ for $0.70 < M_2 < 1.00$

and

$$Cp_B = 0.14\cos(16.53\ M_2 - 5.15) \text{ for } 1.00 \leq M_2 \leq 1.37$$

where the argument of the cosine term is in radians. If this model is converted back into the coordinates of Figure 19, a fairly good correlation results. A comparison of the fitted line and the data points is shown in Figure 22. The agreement between the fitted values and the data is good; the data scatter (defined by the standard deviation) about the fitted line is 1.5% of the locally measured values.

Figures 19 through 21 also display the base pressure measured on the Baseline blades. The base pressure was measured on the Baseline blades with a single tap placed in the trailing edge. Ten data points have been included on each figure. With the exception of the data point near $M_2 = 1.10$ (see Figure 20), the Baseline pressures compare well with the large scale pressures.

4.1.3 Computational Base Pressure Study

Since one of the purposes of this study is to provide experimental data on trailing edge flows to improve the prediction capability of various computational models, it is of interest to compare the experimental results for the base pressure distribution to the numerical output of one of these models. Fortunately, Kiss [31] has studied the flow over the Baseline profile using a two-dimensional, time-averaged Navier-Stokes solver and some of his results are applicable to this study. The program has also been recently applied to a flow study of the large-scale blade at the design exit Mach number. The fundamentals of the computational method are summarized here; reference [31] discusses the method in further detail.

The computer code used for these studies, "ANSERS", was developed at Virginia Tech by R.W. Walters and A.C. Taylor. It is capable of solving the two-dimensional, cell-centered finite volume formulation of the complete Navier-Stokes equations. The program requires a single grid which is non-adaptive; coupled solutions from different zones are not possible. Kiss uses a C-type grid for the computation. The C-type grid starts at a point well downstream of the blade, approaches the blade, wraps around the blade in clockwise fashion, and returns to the same axial location as its starting position. At the starting position one coordinate direction, j, points axially toward the blade. The other coordinate direction, k, always points away from the blade surface; k=0 represents the blade surface and a "splitter" boundary downstream of the blade. Figure 23 displays the j and k coordinate directions at the j=0, k=0 point. Kiss notes that with this type of grid, some distortion of the grid may occur in the trailing edge region. The computational domain extends to 67% axial chord ahead of the blade and 119% axial chord behind the blade. Care is taken to place denser arrays of grid points in regions of high flow gradients, such as near the blade surface and in the downstream wake region. The grid size used for this study is 219 × 23 (j × k); the grid points defining the corners of the finite volumes are shown in Figure 24. A total of 10,870 iterations were carried out for the large-scale cascade flow computation.

Figure 23 also summarizes the turbulence modeling used in the numerical simulation. The pressure side boundary layer and its trailing edge separation are assumed to be laminar. From shadowgraph studies the turbulent transition location on the suction side occurs at 65% of axial chord (85% for Baseline blades). No separation on either the suction or pressure sides upstream of the trailing edge is assumed. A compressible extension of the Clauser eddy viscosity model is applied to the suction side boundary

layer after transition. The Baldwin-Lomax turbulence model is used near the suction side trailing edge region and in the entire wake region.

The results of the computed base pressure distribution are shown in comparison with experimental values at M_2=1.2 in Figure 25. Both the numerical and experimental results indicate a falling pressure in moving away from the center of the trailing edge in either direction. The falling pressure is more drastic for the computational case. The computed results also indicate a large pressure drop ($\Delta p/p_{t1} \simeq 0.19$) near the -80 degree position. The experimental results show this characteristic for slightly higher downstream Mach numbers (Figure 17). The average base pressure level of the computational results (not including the high value on the pressure side) are 14% lower than the average of the measured values.

Kiss has studied the trailing edge flow of the Baseline profile using this computational method. The size of the grid for this study was 437 × 45. The results of a flow visualization of the trailing edge velocity vectors at M_2 = 1.2 are shown in Figure 26. He notes that the asymmetry in the flow is due to the laminar separation on the pressure side and the turbulent separation on the suction side.

The computational results for the blade surface pressures are compared to the experimental values in Section 4.2.2.

4.2 Suction Surface Mach Numbers

This secion summarizes the experimental and computational results obtained for the isentropic suction surface Mach numbers.

4.2.1 Experimental Results

The static pressure data from the five taps on the suction surface are presented in Figures 27 through 29 in terms of an isentropic Mach number. The output from the two trailing edge taps near the suction side are also included in these figures. Tables 5 and 6 present the data in the pressure ratio form, p/p_{t1}, for each downstream Mach number.

Figure 27 displays the rearward suction surface Mach number distributions for subsonic downstream Mach numbers. For most of these cases, the flow is slowly decelerating towards the trailing edge. Yet, at some point within the last 3% axial chord, the flow actually accelerates before reaching the base region. This is most likely occurring at the overexpansion near the start of the trailing edge curvature. At $M_2 = 0.988$, the flow begins to show signs of acceleration well upstream of the trailing edge.

The suction surface Mach distributions for low supersonic exit Mach numbers are displayed in Figure 28. Near $M_2 = 1.11$ the accelerating nature of the flow becomes predominant over this portion of the blade. The flow continues to accelerate for higher downstream Mach numbers. For $M_2 = 1.112$ and $M_2 = 1.145$, the Mach number is drastically reduced in approaching the trailing edge. For higher M_2, the base pressure lowers and this effect is less noticeable.

As the downstream Mach number is increased from 1.23 to 1.39, a variety of flow patterns occur on the suction side near the trailing edge. These Mach number distributions can be seen in Figure 29. The $M_2 = 1.225$ curve acts much like the previous higher curves in Figure 28: an increasing surface Mach number until a slight drop at the trailing edge. The case of $M_2 = 1.251$ has an increasing Mach number all the way

to the trailing edge. Beyond this case, the Mach distribution curves begin to drastically change. The measured Mach number near the 84% axial chord position increases suddenly from 1.18 (at $M_2 = 1.25$) to 1.45 (at $M_2 = 1.31$); apparently, a shock has passed the 84% C_{ax} near $M_2 = 1.3$. The Mach number measured at this 84% position continues to rise until $M = 1.70$ for $M_2 = 1.36$. At $M_2 = 1.386$ the shock has moved down below the 87% C_{ax} position where the Mach number just ahead of the shock is almost 1.9. The base Mach number, M_B, appears to have risen until the appearance of the shock in the vicinity of the trailing edge. From then on, M_B falls slowly (p_B increases) as the suction side shock approaches the trailing edge. Since the shock comes closer and closer to the trailing edge and since it increases the pressure behind it, we can expect the base pressure to begin to rise (i.e. the shock is close enough to influence the base pressure). Another consideration is that, as the shock approaches the trailing edge, the flow turning from the blade curvature is reduced and thus the expansion downstream of the shock becomes weaker.

4.2.2 Computational Results

The computational method discussed in Section 4.2 has been used to determine the pressure distribution on both surfaces of the large scale blade for $M_2 = 1.2$. Figure 30 displays a plot of the distributions in terms of the isentropic surface Mach number. The five suction surface data points for $M_2 = 1.206$ have been included in the figure. The actual surface Mach number is shown to increase more rapidly than the computed Mach number over the rearward suction surface. The computation indicates the suction surface shock location near 77% of C_{ax}.

4.3 Measured Total Pressures

Sample outputs of the measured total pressures, p_{t1} and Δp_t, are included in Figures 31 through 34 for different exit Mach numbers. Although the abscissa indicates blade pitch, it also represents time. Since p_{t1} is measured at a fixed location upstream of the blade row, its output is a function of time only. Thus, the p_{t1} curve provides an indication of how the upstream total pressure varies over the 18 second interval of taking measurements. Generally, the upstream total pressure is more difficult to control when the tunnel is run at higher pressures. This can be seen in the figures for higher downstream Mach numbers. A plot of the mean total pressure, normalized by the atmospheric pressure, for each exit Mach number tested is shown in Figure 35. As a quantitative indicator of the pressure control within the wind tunnel, the standard deviation of the upstream total pressure for each of the exit Mach numbers is shown in Figure 36. For all of the exit Mach numbers tested, the standard deviation is within 0.9% of p_{t1}.

The output from the traversing downstream probe, Δp_t, provides an indicator of the flow periodicity behind the cascade. Unfortunately, since the cascade contains only three blade passages, good periodicity cannot be expected. In Figures 31 through 34, the Δp_t output displays the wake pattern behind blades #2 (left wake) and #3 (right wake). The pressure drop in the wake behind blade #3 is typically higher than the pressure drop behind blade #2; the difference between these pressure drops appears to change from run to run. Typically, the maximum pressure drop behind blade #3 is 20% to 30% more than the maximum pressure drop behind blade #2. Thus, the periodicity assumption is not well justified in this experiment; this topic is taken up in more detail in Section 4.5.2.

For the cases of supersonic outlet flow, the magnitude of the bow shock correction has been included in Figures 32 through 34. The corrected total pressure drop is shown by the dotted curve below the Δp_t curve (most clearly seen in Figure 34).

4.4 Endwall Static Pressures

In order to compute the losses for the blade being studied, the static pressure distribution downstream of the blade row must be obtained. This pressure distribution also allows the periodicity to be quantitatively checked for each exit Mach number.

4.4.1 General Results

Plots of the endwall static pressure distribution over two blade pitches are shown in Figures 37 through 40 for various downstream Mach numbers. In the figures, $0 \leq y/P \leq 1$ represents the pitchwise measurements taken behind blade #2 and $1 \leq y/P \leq 2$ represents the measurements taken behind blade #3. The positions $y/P = 0$ and $y/P = 1$ approximately represent the wake centerlines behind blades #2 and #3, respectively.

At exit Mach numbers greater than 1.1, the static pressure increases in moving upwards from $y/P = 1$, reaching a maximum near $y/P = 1.3$; similarly, p/p_{t1} decreases in moving downward from $y/P = 1$, reaching a minimum near $y/P = 0.5$. As M_2 is lowered, the data for the pressure distribution near $y/P = 1$ becomes more scattered. The scatter may arise from the presence of vortices in the wake.

4.4.2 Flow Periodicity

In Figures 37 through 40, the static pressure distributions, like the downstream total pressure plots, do not appear to indicate good flow periodicity. At this point, the flow periodicity has essentially been studied qualitatively for individual exit Mach numbers. The calculation of the average Mach number behind each blade (based on the area-averaged pressure) provides a simple way to quantitatively analyze the flow periodicity. If the Mach number behind blade #3 (M_3) is compared with the Mach number behind blade #2 (M_2) in a plot of the form, $M_3/M_2 = fn(M_2)$ then the variation of the experimental data about the line $M_3/M_2 = 1$ allows the periodicity to be checked over the range of Mach numbers of interest. This plot is shown in Figure 41. The figure indicates that near $M_2 = 0.95$ the Mach number behind blade #3 drops below the Mach number behind blade #2 and continues to drop until $M_2 \simeq 1.2$. Unfortunately, the maximum aperiodicity ($M_3/M_2 - 1 \simeq -7\%$) occurs near the design exit Mach number ($M_2 = 1.2$). The overall variation in the periodicity, $(M_3/M_2)_{max} - (M_3/M_2)_{min}$, is approximately 10%. It should be noted that the errors in computing M_3 are higher than the errors in computing M_2 since twice as many static pressure measurements are taken behind blade #2.

4.5 Loss Results

From the results of Sections 4.4 and 4.5, the mass-averaged total pressure loss behind blade #2, L, is computed for each value of M_2. The results of this computation along with some results for the Baseline blade are shown in Figure 42. The losses for both the Baseline profile and the large scale profile are nearly the same for $M_2 < 1.2$. At higher Mach numbers, the large scale losses do not appear to increase as fast as the Baseline

losses. The Baseline losses reported in the figure are the average losses behind two blades.

If the average loss behind two of the large scale blades (blade #2 and #3) is computed, periodicity must be assumed because the downstream probe traverses approximately 1.5 pitch lengths. In addition, at higher Mach numbers ($M_2 > 1.2$), changes in the flow angle behind the blades causes the wake behind blade #3 to shift out of the range where Δp_t is measured; this is seen in Figure 34 where the right wake, representing blade #3, is not fully caught by the downstream traversing probe. This effect tends to lower the loss computed behind blade #3. The results for the average loss behind the two blades are shown in Figure 43. The average loss is nearly the same as the blade #2 loss for most Mach numbers, except for $M_2 > 1.2$, where the effect of the wake shift begins to lower the average loss. The averaging of the losses behind each blade, however, appears to reduce the scatter in the data.

Figure 44 shows a plot of the profile loss as a function of the base pressure. Since the loss measurements and the base pressure measurements were taken in separate runs, the base pressures shown in Figure 44 are estimated from the Cp_B correlation discussed in Section 4.1.2. The results show the expected trend of lower loss with increasing base pressure. The loss appears to be most strongly influenced by the base pressure in the case of sonic exit flow. Outside of this portion of the graph, the loss drops uniformly with the increasing base pressure. (Note: the exit Mach number is varying between 0.7 and 1.4 in Figure 44)

4.6 Shadowgraphs

Figures 45 through 51 display the shadowgraph pictures of the trailing edge region of blade #2 for different exit Mach numbers. Due to the trailing edge instrumentation, portions of the blade near the trailing edge cannot be clearly seen. The most notable case is just upstream of the trailing edge on the suction side, where the tubes are led out from the endwalls. A channel is drilled in the endwalls to allow the measurement tubes to come through and the exposed portion of this channel is filled with sealant after the cascade is put together. The region where the sealant is applied, however, forms a dark region on the suction surface of the blade in the shadowgraph pictures. Fortunately, this dark region is sufficiently upstream of the trailing edge so that it does not obscure the important regions of the flow.

The shadowgraph pictures allow the location of the trailing edge shocks to be revealed. The angle between the two trailing edge shocks slowly decreases as the exit Mach number is increased. At $M_2 > 1.1$ the separation shock and the reattachment shock off the pressure side of the blade meet near the centerline of the blade passage to form a stronger shock leading to the suction side of the adjacent blade. On the suction side, the two shocks merge near the axial location where the endwall measurements are taken. For lower Mach numbers, the reattaching compression does not occur through a shock. For all of the exit Mach numbers tested, the free shear layers (see Figure 1) off the trailing edge do not converge to form the closed triangular base region. It appears difficult to resolve the downstream vortex shedding from the shadowgraph pictures.

The shadowgraphs for $M_2 > 1$ show a shock generated on the suction side about a half inch upstream of the trailing edge. This shock is most likely the shock off of one of the taps. (Shadowgraphs of the cascade before instrumentation do not reveal this shock).

Figure 52 displays a shadowgraph picture for the Baseline cascade at $M_2 = 1.17$. The separation and reattachment shocks from the pressure side merge at a point closer to the trailing edge. With this exception, the Baseline shadowgraphs compare well with the large scale shadowgraphs.

4.7 Additional Considerations

The following section documents results for additional flow variables which were measured or calculated for each run. Certain flow variables which were not measured are briefly discussed.

4.7.1 Upstream Total Temperature

In computing the losses for the large scale profile, the upstream total temperature, T_{t1}, is assumed to remain constant for each run at $T_{t1} = 283$ K. The measured upstream total temperature, however, typically varies from one run to the next as well as within each run. The upstream total temperature variation from run to run is shown in Figure 53. The maximum variation of T_{t1} over the time of each run is characterized by ± 3 standard deviations, shown by the upper and lower dotted curves in the figure. Approximately 880 measurements of T_{t1} were taken during each run. Figure 54 shows the measured output of T_{t1} for a typical run ($M_2 = 0.94$).

4.7.2 Upstream Relative Humidity

In previous studies at the Virginia Tech (Kiss [31]), the variations in the relative humidity within the wind tunnel were found to be correlated to the scatter in the computed loss data. For this reason, the relative humidity is monitored for each run with a humidity sensor placed upstream of the cascade. Thirty-five measurements are taken with each run; the mean and the standard deviation of the humidity for several runs are displayed in Figure 55. For most runs, the mean relative humidity fluctuates between 6% and 7%.

4.7.3 Reynolds Number

The definition of the Reynolds number for this study is based on the axial chord length, C_{ax}, and the upstream conditions. Thus, the equation for the Reynolds number can be written as

$$Re = \frac{\rho_1 U_1 C_{ax}}{\mu}$$

where μ is the viscosity of air at the assumed value of the upstream total temperature, T_{t1} = 283 K. Since a tailboard is not used in this experiment, the Reynolds number cannot be varied independently from the downstream Mach number. At all values of M_2, the Reynolds number for the Baseline blade is well below the Reynolds number for the large scale blade (due to the smaller C_{ax}); thus, dynamic similarity is not assured for a true comparison of the results of the two flow models. Figure 56 shows the results of the computation of Re for the large scale profile.

4.7.4 Freestream Turbulence

The freestream turbulence was not measured in this experiment.

4.7.5 Flow Angle

The flow angle downstream of the blade row is not directly measured during the experiment; instead, the angle is assumed to be equal to the blade exit angle (β_2 = -67°). This cannot be true for all downstream Mach numbers since the shadowgraph pictures indicate changing trailing edge shock angles. It is possible to estimate the change in the flow angle in increasing to higher downstream Mach numbers. This can be done by studying the output of the downstream traversing probe (Figures 31 through 34) for two different values of M_2. Assuming that the maximum value of Δp_t represents the wake centerline, then the pitchwise distance between the wake centerline for the exit Mach number of interest and the wake centerline for the reference exit Mach number is measured. Knowing the initial pitchwise and axial probe position, the change in the downstream flow angle, $\Delta\beta_2$, can be computed from geometric relations. Using this method β_2 changed from -67.6° at M_2 = 0.89 to -55.9° at M_2 = 1.33. Thus, the trailing edge flow turns nearly 12° toward the suction surface in increasing the downstream Mach number from 0.89 to 1.33.

4.7.6 Flow Uniformity

An additional concern for testing the enlarged blade is the effect of the lower aspect ratio, S/C_{ax}, on the flow pattern over the blade. The aspect ratio of the large scale blade is 1.21 (compared to 4.00 for the Baseline profile). For low aspect ratio blades,

the secondary flows (horseshoe and passage vortices) induce less spanwise uniformity at the trailing edge plane. Since the trailing edge region of the tested blade contains the base pressure measurement taps, it is important to ensure that the flow is uniform over the central span at the trailing edge (in particular, the central 17% of the span in which the taps are placed). A flow visualization over the large scale blade reveals uniform streamlines over the central portion of the span all the way to the trailing edge. This visualization is shown for the suction and pressure sides in Figures 57 and 58. The flow is from left to right in these figures.

5.0 UNCERTAINTY ANALYSIS

An important part of reporting test results is the analysis of experimental uncertainties. Baines, et al. [32] provides a critical summary of the commonly accepted methods for determining uncertainties of various measured and calculated quantities. In this chapter, some of the individual uncertainties of the measured quantities are based on the manufacturer's specification for those instruments. In cases where it is possible to determine the variation of the measurements taken with the instrument, then two standard deviations will represent the uncertainty of that measured quantity.

The following chapter describes the basic methods used in determining the uncertainties of the important measured and computed quantities. Uncertainties related to the base pressure measurements are treated first; this is followed by an analysis of the uncertainty in the loss and in the exit Mach number.

5.1 Uncertainty in the Base Pressure Measurements

The uncertainty in the surface pressure measurements come in two forms: an uncertainty in the measured pressure and an uncertainty in the location of the taps. Since this experiment is essentially a single-sample experiment, in which the static

pressures are measured at one point in time and the same run is not repeated, the uncertainty in the static pressure measurement is based on the manufacturer's specification for the 32-channel transducer and on the calibration errors of the PSI system. Doughty [17] has estimated the variation in most of the measured quantities; he reports a value of $\delta p = \pm 0.03$ psi for the individual static pressures measured with the PSI system. Thus, the error in an individual surface tap measurement is $\pm$ 0.03 psi; the error in the average base pressure is $\pm$ 0.017 psi.

The second source of error in the surface pressure measurements is determining the exact location of the taps placed in the surface. Unfortunately, the location of the trailing edge taps were measured after they had been machined. Due to the difficulty in determining a reference point to make these angular measurements and due to the small trailing edge diameter, the uncertainty in the trailing edge tap locations is relatively high. The tap positions were measured by placing a 0.020-inch drill bit into each hole and measuring the angular position of the drill bit with a protractor. The estimated uncertainty for these trailing edge tap locations (shown in Figure 13) is $\pm$ 3 degrees. Another implication of a thin trailing edge is that each of the drilled taps covers 10.5% of the trailing edge arc length. Thus, the pressure measured by a particular tap should be considered as the average pressure over that 10.5% of the trailing edge. The uncertainty in the location of the suction surface taps is $\pm$ 0.004 inches ($\pm$ 0.10 mm) or $\pm$ 0.081% of axial chord.

5.2 Uncertainty in the Computed Loss and Mach Number

The method discussed here for determining the uncertainty in the profile loss, L, is suggested by Baines, et al. [32] and is equivalent to the uncertainty analysis of Doughty

[17]. The major difference between this analysis and that of Doughty is that an attempt is made to include the relative humidity in the calculations of the uncertainty for the loss and exit Mach number. Bias errors in the instruments are assumed to be small compared to the precision errors.

In order to determine the uncertainty in the loss and Mach number computation, the measured variables which affect the loss and Mach number must first be identified. The profile loss is assumed to be a function of six variables, namely,

$$L = L(p_{atm}, p_{t1}, p_2, \Delta p_t, T_{t1}, RH)$$

and the exit Mach number is assumed to be a function of three variables:

$$M_2 = M_2(p_{atm}, p_{t1}, p_2).$$

The first five variables in the loss equation above are assumed since they are all necessary in the data reduction routine; the upstream relative humidity, RH, has been included because experimental evidence (Kiss [31]) has indicated that the loss and humidity are correlated. With these assumptions, the formulae used for the uncertainties in the loss and exit Mach number are:

$$\delta L = \sqrt{\left[\left(\frac{\partial L}{\partial p_{atm}}\right)\delta p_{atm}\right]^2 + \left[\left(\frac{\partial L}{\partial p_{t1}}\right)\delta p_{t1}\right]^2 + \ldots + \left[\left(\frac{\partial L}{\partial RH}\right)\delta RH\right]^2}$$

and

$$\delta M_2 = \sqrt{\left[\left(\frac{\partial M_2}{\partial p_{atm}}\right)\delta p_{atm}\right]^2 + \left[\left(\frac{\partial M_2}{\partial p_{t1}}\right)\delta p_{t1}\right]^2 + \left[\left(\frac{\partial M_2}{\partial p_2}\right)\delta p_2\right]^2}$$

The values δL and δM_2 represent the estimated uncertainties of the computed loss and Mach number based on the individual precision errors of the measured variables. Doughty [17] has determined the values of the individual uncertainties for each measured variable: $\delta p_{t1} = \pm 0.036$ psi (± 0.248 kPa), $\delta(\Delta p_t) = \pm 0.012$ psi (± 0.082 kPa), $\delta p_2 = \pm 0.009$ psi (± 0.062 kPa), and $\delta p_{atm} = \pm 0.15$ psi (± 1.034 kPa). An estimate of δT_{t1} can be obtained from the standard deviation of the temperature output over the time of each run. This value, based on two standard deviations of the measured data (Figure 52), is assumed to be $\delta T_{t1} = \pm 2.0$ K. The value of the variation in the relative humidity measurement is based on the humidity sensor accuracy specification, $\delta RH = \pm 3\%$. The variation of loss with relative humidity ($\partial L/\partial RH$) is estimated from previous experimental data (Reference 31). The other partial derivatives in the above equations are estimated by a "jitter" method, in which the value of one of the six variables of interest is slightly changed and the resulting change in L or M_2 is found. These derivatives are evaluated for three different exit Mach numbers: 0.83, 1.01, and 1.22.

The results of the uncertainty estimates for δL are:

$\delta L = \pm 0.165\%$ at $M_2 = 0.83$

$\delta L = \pm 0.162\%$ at $M_2 = 1.01$

$\delta L = \pm 0.178\%$ at $M_2 = 1.22$

The results of the uncertainty estimates for δM_2 are:

$\delta M_2 = \pm 0.005$ at $M_2 = 0.83$

$\delta M_2 = \pm 0.006$ at $M_2 = 1.01$

$\delta M_2 = \pm 0.008$ at $M_2 = 1.22$

Kiss [31] has carried out a more extensive uncertainty analysis for the wind tunnel facility in which the instrument bias errors are partially taken into account. His results indicate $\delta L = \pm 0.12\%$ and $\delta M_2 = \pm 0.01$ for higher values of M_2.

The results of these analyses should be compared with the scatter in the loss data shown in Figure 42. Using an exponential curve through the loss data, the scatter is estimated to be $\delta L = \pm 0.314\%$ (two standard deviations). After the variability of the exit Mach number (± 0.01) is taken into account, then, $\delta L = \pm 0.306\%$. Thus, the measured variability in the loss data is about 1.8 times the calculated uncertainty in the loss. A number of factors may be responsible for this deviation, for example, one or more of the derivative terms in the uncertainty calculation may have been poorly estimated. A more probable source of the data scatter is that many of the bias errors (which may change from day to day) in the measuring instruments have been neglected.

6.0 CONCLUSIONS AND RECOMMENDATIONS

A summary of the important results discussed in Chapter 4 are provided here. Some recommendations for an improved study of the base pressure have also been included.

6.1 Conclusions

6.1.1 Summary of Results

A uniform pressure has been measured over at least the central 90° of the trailing edge for each downstream Mach number tested.

The base pressure (averaged from the central three trailing edge taps) falls with increasing exit Mach numbers from $p_B/p_{t1} \simeq 0.72$ (at $M_2 = 0.73$) to a minimum value $p_B/p_{t1} \simeq 0.30$ (at $M_2 = 1.30$). The fall is linear for subsonic exit Mach numbers. For $M_2 > 1.3$, the base pressure increases to $p_B/p_{t1} \simeq 0.35$ at M2 = 1.38.

The base pressures measured from the large scale and Baseline blades are high compared to Sieverding's correlation for geometrically similar blades at most of the exit Mach numbers tested.

The results of a viscous computational method predict a base pressure 14% lower than the average of the experimental values at $M_2 = 1.2$.

The shadowgraph pictures reveal the pressure-side separation shock extending well out into the flow, where it joins the reattaching shock nearly halfway through the blade passage. These two shocks join closer to the trailing edge on the Baseline blade. With this exception, the shadowgraphs for the large scale and Baseline blades compare very well.

The maximum isentropic Mach number measured on the pressure side near the trailing edge is $M \simeq 1.28$, which is measured at the -83° position and is independent from exit Mach number for $M_2 > 1.2$. The measured trailing edge pressures near the suction surface, however, do not reach a minimum for all values of M_2 tested.

The large-blade profile losses, characterized by the loss coefficient, L, increase exponentially from $L = 0.8\%$ at $M_2 = 0.68$ to $L = 3.0\%$ at $M_2 = 1.20$. Increasing to higher exit Mach numbers, the loss increases only up to 3.4% at $M_2 = 1.33$.

Periodicity is quantified by the parameter, M_3/M_2. The Mach number behind blade #3 (M_3) dropped below the Mach number behind blade #2 (M_2) by as much as 7% of M_2.

6.1.2 General Conclusions

The base pressure on a turbine blade has been experimentally determined for exit Mach numbers between 0.7 and 1.4. The relatively high base pressure measured

indicates that, for minimizing aerodynamic losses, the experimental blade is well designed. The experiment has also demonstrated, however, that two current methods of base pressure prediction (experimental correlation, computational model) appear to be limited in their accuracy.

6.2 Recommendations

Several recommendations are suggested for an improved study of the base pressure distribution. More taps with a smaller hole diameter are suggested to be placed around the trailing edge. It is believed that at least ten taps can be placed in the trailing edge, where each of these taps can have a diameter as small as 0.010 inch.

The use of a CNC milling machine to drill the taps in the trailing edge can greatly increase the accuracy of determining the angular location of each tap. Thus, for future base pressure study, the CNC milling machine is recommended for tap drilling.

Since the present study has indicated uniform pressure around the central portion of the trailing edge, additional studies should focus on placing more taps in the regions near the start of the trailing edge curvature on either side of the blade.

The effects of coolant ejection on the base pressure should be investigated with several taps around the coolant slots.

A special downstream probe for measuring the flow angle may be useful for studying the deflection of the fluid at the trailing edge at each downstream Mach number.

REFERENCES

1. White, F.M., *Fluid Mechanics*, 2nd ed., McGraw-Hill, New York, 1986, pp.412-414.

2. Moulden, T.H., *Fundamentals of Transonic Flow*, John Wiley & Sons, New York, 1984, p.4.

3. Denton, J.D., and Xu, L., "The Trailing Edge Loss of Transonic Turbine Blades", *ASME Journal of Turbomachinery*, Vol.112, No.2, 1990, pp.277-285, paper No. 89-GT-278.

4. Tanner, M., "Theoretical Prediction of Base Pressure for Steady Flows", *Progress in Aerospace Sciences*, Vol.14, 1973, pp.177-225.

5. Nash, J.F., "An Analysis of Two-dimensional Turbulent Base Flow, Including the Effect of the Approaching Boundary Layer", *ARC R&M* 3344 (1963).

6. McDonald, H., "Turbulent Shear Layer Reattachment With Special Emphasis on the Base Pressure Problem", *Aero. Quart.*, Vol.15, 1964, pp.247-280.

7. Tanner, M., "Steady Base Flows", *Progress in Aerospace Sciences*, Vol.21, 1984, p.81-157.

8. Inoue, M., Hayashi, H., Yamaguchi, S., and Takefumi, I., "Compatibility of Transonic Flows at Thick Trailing Edge in Turbine Blade Row", *Bulletin of JSME*, Vol.26, No.221, 1983, pp.1877-1883.

9. Amana, O.M., Demuren, H.O., Louis, J.F., Sieverding, C., and Chauvin, J., "Aerodynamics and Heat Transfer at the Trailing Edge of Transonic Blades", *ASME paper* No. 76-GT-95 (1976).

10. Korst, H.H., "A Theory for Base Pressures in Transonic and Supersonic Flow", *ASME Journal of Applied Mechanics*, Vol.23, 1956, pp.593-600.

11. Gostelow, J.P., "Trailing Edge Flows Over Turbomachine Blades and the Kutta-Joukowsky Condition", *ASME paper* No. 75-GT-94 (1975).

12. Bogod, A.B., Granovskii, A.V., and Ivanov, M.Ya., "Numerical Investigation of Some Special Features of Transonic Flows in Plane Turbine Cascades", *Fluid Dynamics*, Vol.11, No.2, 1976, pp.293-299.

13. MacMartin, I.P., and Norbury, J.F., "The Aerodynamics of a Turbine Cascade with Supersonic Discharge and Trailing Edge Blowing", *ASME paper* No. 74-GT-120 (1974).

14. Horstman, C.C., "Prediction of Separated Asymmetric Trailing-Edge Flows at Transonic Mach Numbers", *AIAA Journal*, Vol.21, No.9, 1983, pp.1255-1261.

15. Dawes, W.N., Camus, J-J, Xu, L.P., and Graham, C.G., "Measured and Predicted Loss Generation in Transonic Turbine Blading", *AGARD CP 401*, Paper No.8, 1987.

16. Sieverding, C.H., Stanislas, M., and Snoeck, J., "The Base Pressure Problem in Transonic Turbine Cascades", *ASME Journal of Engineering for Power*, Vol.102, No.3, 1980, pp.711-718, paper No. 79-GT-120.

17. Doughty, R.L., "The Effect of Blade Solidity on the Aerodynamic Loss of a Transonic Turbine Cascade", *VPI Thesis*, 1991.

18. Xu, L., and Denton, J.D., "The Base Pressure and Loss of a Family of Four Turbine Blades", *ASME Journal of Turbomachinery*, Vol.110, No.1, 1988, pp.9-17, paper No. 87-GT-202.

19. Denton, J.D., "A Survey and Comparison of Methods for Predicting the Profile Loss of Turbine Blades", *Heat and Fluid Flow in Steam and Gas Turbine Plants Conference*, Inst. of Mech. Engr., 1974, pp.204-212, paper No. C76/73.

20. Zeidan, O., "An Experimental Examination of the Effect of Trailing Edge Thickness on the Aerodynamic Performance of Gas Turbine Blades", *VPI Thesis*, 1989.

21. Kiock, R., Lehthaus, F., Baines, N.C., and Sieverding, C.H., "The Transonic Flow Through a Plane Turbine Cascade as Measured in Four European Wind Tunnels", *ASME Journal of Engineering for Gas Turbines and Power*, Vol.108, No.2, 1986, pp.277-284, paper No. 85-IGT-44.

22. Motallebi, F., and Norbury, J.F., "The Effect of Base Bleed on Vortex Shedding and Base Pressure in Compressible Flow", *Journal of Fluid Mechanics*, Vol.110, 1981, pp.273-292.

23. Paige, R.W., "A Computational Method for the Aerodynamic Design of Transonic Turbine Blades", *PhD Thesis*, University of Cambridge, United Kingdom, 1983.

24. Sieverding, C., Decuyper, M., Colpin, J., and Amana, O., "Model Tests for the Detailed Investigation of the Trailing Edge Flow in Convergent Transonic Turbine Cascades", *ASME paper* No. 76-GT-30, (1976).

25. Mee, D.J., Baines, N.C., Oldfield, M.L.G., and Dickens, T.E., "An Examination of the Contributions to Loss on a Transonic Turbine Blade in Cascade", *ASME Journal of Turbomachinery*, Vol.114, No.1, 1992, pp.155-162.

26. Bölcs, A., and Sari, O., "A New Base Pressure Correlation for Transonic and Supersonic Flows", *ASME paper* No. 91-GT-324, (1991)

27. Bertsch, R., "An Experimental Examination of the Influence of Trailing-Edge Coolant Ejection on Blade Losses in Transonic Turbine Cascades", *VPI Thesis*, 1990.

28. Sieverding, C.H., "The Influence of Trailing Edge Ejection on the Base Pressure in Transonic Turbine Cascades", ASME Journal of Engineering for Power, Vol.105, No.2, 1983, pp.215-222.

29. Zaccaria, M.A., "Development of a Transonic Cascade Facility", *VPI Thesis*, 1988.

30. Singer, R.T., "An Experimental Examination of the Effect of Trailing Edge Injection on the Aerodynamic Performance of Gas Turbine Blades", *VPI Thesis*, 1988.

31. Kiss, T., "Experimental and Numerical Investigation of Transonic Turbine Cascade Flow", *VPI Dissertation*, 1992.

32. Baines, N.C., Mee, D.J., and Oldfield, M.L.G., "Uncertainty Analysis in Turbomachine and Cascade Testing", *International Journal of Engineering Fluid Mechanics*, Vol.4, No.4, 1991, pp. 375-401.

APPENDIX A. TABLES

Table 1. Main Characteristics of the Baseline and Large Scale Blade (1)

Profile	Large-Scale	Baseline
True Chord Length, C	6.485 in. 16.47 cm	1.947 in. 4.95 cm
Pitch, P	4.906 in. 12.46 cm	1.467 in. 3.73 cm
Span, S	6.000 in 15.24 cm	6.000 in. 15.24 cm
Axial Chord, Cax	4.960 in. 12.60 cm	1.500 in. 3.81 cm
Throat Height, T	1.603 in. 4.07 cm	0.517 in. 1.31 cm
Solidity, Cax/P	1.011	1.025
Aspect Ratio, S/Cax	1.210	4.000
Trailing Edge Thickness	0.126 in. 3.20 mm	0.038 in. 0.97 mm
Stagger	38.5 deg	38.5 deg

Table 2. Main Characteristics of the Baseline and Large Scale Blade (2)

Profile	Large-Scale	Baseline
Trailing Edge Wedge Angle	8.5 deg	8.5 deg
Suction Side Turning Downstream of Throat	9.6 deg	9.6 deg
Number of Blade Passages	3	10
Design Inlet Mach Number (choked)	0.1941	0.2091
Design Outlet Mach Number	1.20	1.20
Inlet Relative Flow Angle	0 deg	0 deg
Exit Relative Flow Angle	-67 deg	-67 deg
Suction Side Transition Location (Percent Axial Chord)	65 %	85 %
Inlet Reynolds Number Based on Cax At Design Mach Number, M2=1.2	830000	260000
Blade Material	Aluminum	Stainless Steel

Table 3. Normalized Pressures (p/p_{t1}) Around the Trailing Edge (1)

Exit Mach Number	Angular Position (Degrees: +/SS, -/PS)				
	78	47	2	-44	-83
0.729	0.7002	0.7132	0.7168	0.7149	0.6689
0.761	0.6734	0.6920	0.6952	0.6938	0.6399
0.796	0.6484	0.6687	0.6755	0.6681	0.6073
0.815	0.6386	0.6617	0.6612	0.6596	0.5979
0.829	0.6349	0.6494	0.6550	0.6534	0.5935
0.859	0.6105	0.6256	0.6324	0.6261	0.5575
0.865	0.6064	0.6272	0.6322	0.6260	0.5615
0.874	0.6021	0.6187	0.6263	0.6221	0.5506
0.881	0.5959	0.6148	0.6190	0.6162	0.5469
0.883	0.5921	0.6159	0.6147	0.6154	0.5417
0.910	0.5836	0.5982	0.6035	0.6006	0.5322
0.920	0.5732	0.5910	0.5914	0.5924	0.5179
0.928	0.5611	0.5827	0.5903	0.5827	0.5085
0.930	0.5654	0.5820	0.5878	0.5838	0.5109
0.947	0.5642	0.5690	0.5793	0.5782	0.5126
0.957	0.5489	0.5626	0.5652	0.5612	0.5020
0.969	0.5364	0.5589	0.5650	0.5556	0.4900
0.972	0.5347	0.5554	0.5541	0.5491	0.4922
0.988	0.5322	0.5532	0.5560	0.5491	0.4858
1.005	0.5293	0.5426	0.5452	0.5367	0.4876
1.018	0.5263	0.5422	0.5432	0.5378	0.4837
1.039	0.5323	0.5476	0.5495	0.5466	0.4811
1.054	0.5231	0.5385	0.5478	0.5391	0.4656
1.060	0.5331	0.5456	0.5507	0.5461	0.4786
1.075	0.5163	0.5191	0.5189	0.5243	0.4574
1.112	0.4890	0.4970	0.4904	0.4943	0.4364
1.130	0.4671	0.4777	0.4755	0.4811	0.4204
1.143	0.4503	0.4579	0.4687	0.4498	0.4031
1.145	0.4518	0.4616	0.4655	0.4614	0.4111

Table 4. Normalized Pressures (p/p_{t1}) Around the Trailing Edge (2)

Exit Mach Number	Angular Position (Degrees: +/SS, -/PS)				
	78	47	2	-44	-83
1.183	0.3882	0.4071	0.4105	0.4077	0.3753
1.189	0.4059	0.3972	0.3991	0.4095	0.3779
1.194	0.3715	0.3870	0.3923	0.3905	0.3715
1.206	0.3714	0.3945	0.4017	0.3897	0.3712
1.209	0.3421	0.3600	0.3663	0.3649	0.3703
1.216	0.3294	0.3584	0.3518	0.3564	0.3693
1.219	0.3371	0.3574	0.3578	0.3576	0.3677
1.221	0.3355	0.3474	0.3507	0.3512	0.3703
1.223	0.3268	0.3384	0.3471	0.3455	0.3668
1.225	0.3468	0.3604	0.3618	0.3694	0.3684
1.228	0.3229	0.3386	0.3436	0.3440	0.3686
1.236	0.3158	0.3179	0.3211	0.3219	0.3688
1.251	0.2987	0.3286	0.3319	0.3338	0.3657
1.289	0.2920	0.3207	0.3286	0.3208	0.3677
1.296	0.2864	0.3002	0.3042	0.3044	0.3674
1.305	0.2915	0.3064	0.3074	0.3075	0.3671
1.313	0.2935	0.3057	0.3123	0.3121	0.3655
1.317	0.2885	0.3025	0.3060	0.3098	0.3665
1.328	0.2988	0.3122	0.3149	0.3162	0.3654
1.330	0.3034	0.3154	0.3170	0.3194	0.3676
1.332	0.2997	0.3137	0.3180	0.3204	0.3663
1.342	0.3091	0.3248	0.3286	0.3329	0.3670
1.351	0.3110	0.3294	0.3359	0.3371	0.3672
1.363	0.3129	0.3283	0.3313	0.3307	0.3677
1.364	0.3103	0.3310	0.3347	0.3365	0.3662
1.380	0.3211	0.3426	0.3452	0.3463	0.3682
1.386	0.3028	0.3256	0.3293	0.3300	0.3673
1.388	0.3004	0.3089	0.3152	0.3166	0.3675

Table 5. Normalized Pressures (p/p_{t1}) on the Suction Surface (1)

Downstream Mach Number M2	Percent Axial Chord 83.7	87.3	90.6	93.7	96.9
0.729	0.6706	0.6739	0.6879	0.6961	0.7100
0.761	0.6618	0.6545	0.6711	0.6818	0.6861
0.796	0.6280	0.6251	0.6467	0.6565	0.6670
0.815	0.6170	0.6147	0.6292	0.6390	0.6570
0.829	0.6091	0.6086	0.6219	0.6271	0.6363
0.859	0.5802	0.5845	0.5887	0.5975	0.6226
0.865	0.5909	0.5815	0.5906	0.6172	0.6282
0.874	0.5621	0.5725	0.5750	0.5926	0.5957
0.881	0.5800	0.5827	0.5867	0.6012	0.6051
0.883	0.5802	0.5759	0.5936	0.6017	0.6072
0.910	0.5502	0.5486	0.5629	0.5808	0.5940
0.920	0.5428	0.5392	0.5510	0.5653	0.5688
0.928	0.5331	0.5363	0.5538	0.5645	0.5734
0.930	0.5240	0.5186	0.5468	0.5616	0.5758
0.947	0.5085	0.5008	0.5331	0.5594	0.5644
0.957	0.5117	0.5188	0.5385	0.5509	0.5692
0.969	0.4926	0.4721	0.5403	0.5497	0.5547
0.972	0.5055	0.5065	0.5221	0.5488	0.5591
0.988	0.4865	0.4534	0.5106	0.5487	0.5503
1.005	0.4823	0.4487	0.4659	0.5010	0.5535
1.018	0.4830	0.4426	0.4420	0.4764	0.5302
1.039	0.4748	0.4378	0.4382	0.4458	0.5222
1.054	0.4720	0.4293	0.4262	0.4302	0.5038
1.060	0.4603	0.4240	0.4207	0.4210	0.4599
1.075	0.4490	0.4094	0.3985	0.3955	0.3964
1.112	0.4432	0.4024	0.3946	0.3897	0.3954
1.130	0.4358	0.3966	0.3855	0.3779	0.3688
1.143	0.4302	0.3931	0.3812	0.3718	0.3664
1.145	0.4348	0.3881	0.3781	0.3694	0.3540

Table 6. Normalized Pressures (p/p_{t1}) on the Suction Surface (2)

Downstream Mach Number M2	Percent Axial Chord 83.7	87.3	90.6	93.7	96.9
1.183	0.4266	0.3785	0.3686	0.3553	0.3343
1.189	0.4254	0.3815	0.3653	0.3547	0.3348
1.194	0.4312	0.3798	0.3639	0.3503	0.3315
1.206	0.4265	0.3834	0.3682	0.3541	0.3341
1.209	0.4318	0.3884	0.3670	0.3484	0.3309
1.216	0.4236	0.3811	0.3635	0.3473	0.3284
1.219	0.4272	0.3790	0.3598	0.3410	0.3237
1.221	0.4311	0.3872	0.3688	0.3447	0.3196
1.223	0.4381	0.3888	0.3735	0.3449	0.3135
1.225	0.4279	0.3798	0.3614	0.3437	0.3248
1.228	0.4341	0.3875	0.3689	0.3440	0.3179
1.236	0.4309	0.3953	0.3741	0.3445	0.3099
1.251	0.4292	0.3841	0.3676	0.3419	0.3135
1.289	0.4290	0.3855	0.3659	0.3430	0.3155
1.296	0.2785	0.3532	0.3698	0.3839	0.3501
1.305	0.2929	0.3577	0.3651	0.3797	0.3494
1.313	0.2793	0.3577	0.3583	0.3700	0.3497
1.317	0.2481	0.3561	0.3717	0.3797	0.3488
1.328	0.2094	0.3401	0.3430	0.3545	0.3540
1.330	0.2139	0.3297	0.3517	0.3741	0.3520
1.332	0.2082	0.3362	0.3407	0.3492	0.3568
1.342	0.2017	0.3083	0.3333	0.3401	0.3554
1.351	0.2038	0.2939	0.3337	0.3368	0.3404
1.363	0.2023	0.2673	0.3210	0.3266	0.3311
1.364	0.2025	0.2268	0.3214	0.3192	0.3176
1.380	0.2027	0.1692	0.3027	0.3111	0.3158
1.386	0.2041	0.1511	0.2480	0.2976	0.2854
1.388	0.2041	0.1506	0.2463	0.2963	0.2896

APPENDIX B. FIGURES

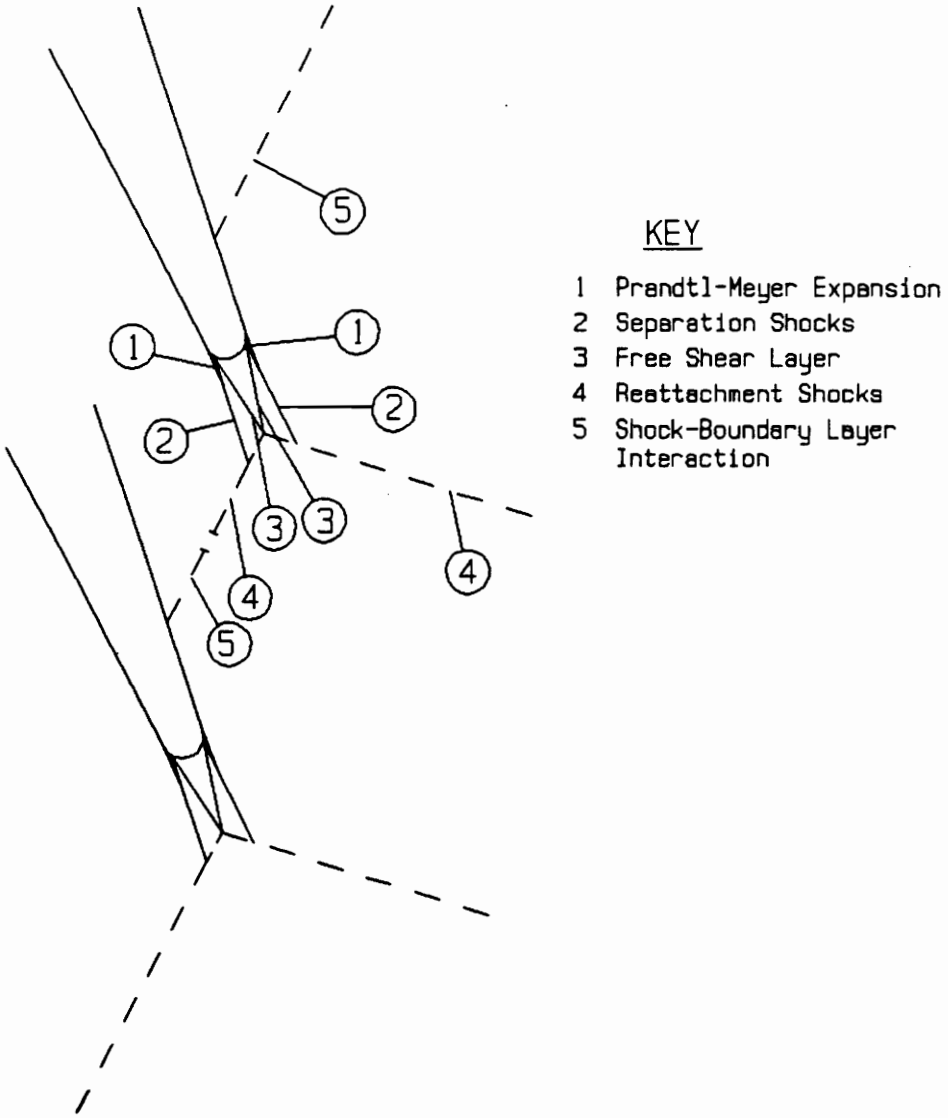

Figure 1. Trailing Edge Flow Field

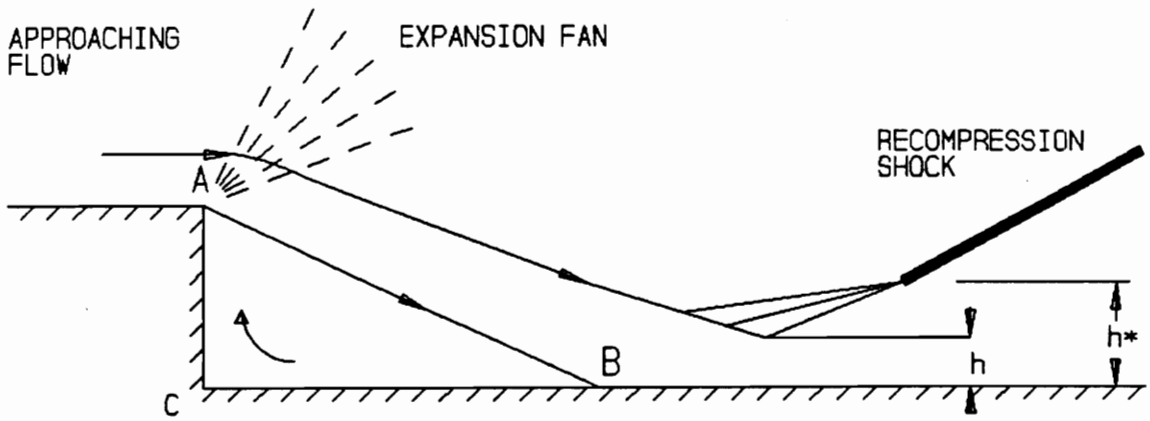

DIVIDING STREAMLINE: AB
SEPARATION POINT: A
REATTACHMENT POINT: B
SHEAR LAYER THICKNESS: h
SUBSONIC RECOMPRESSION HEIGHT: h*

Figure 2. Backward Step Flow Model

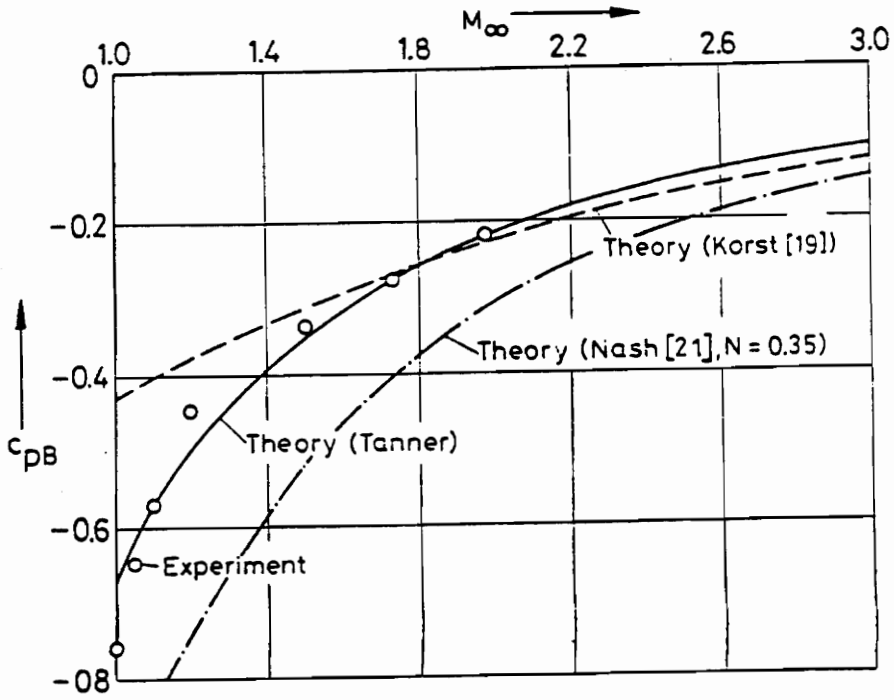

Figure 3. Results of Backward Step Flow Models from Ref. [7]

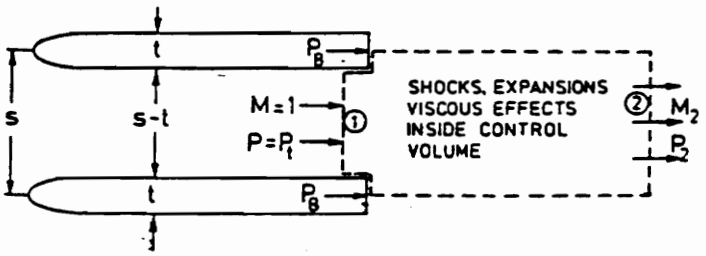

Control volume analysis of an unstaggered cascade

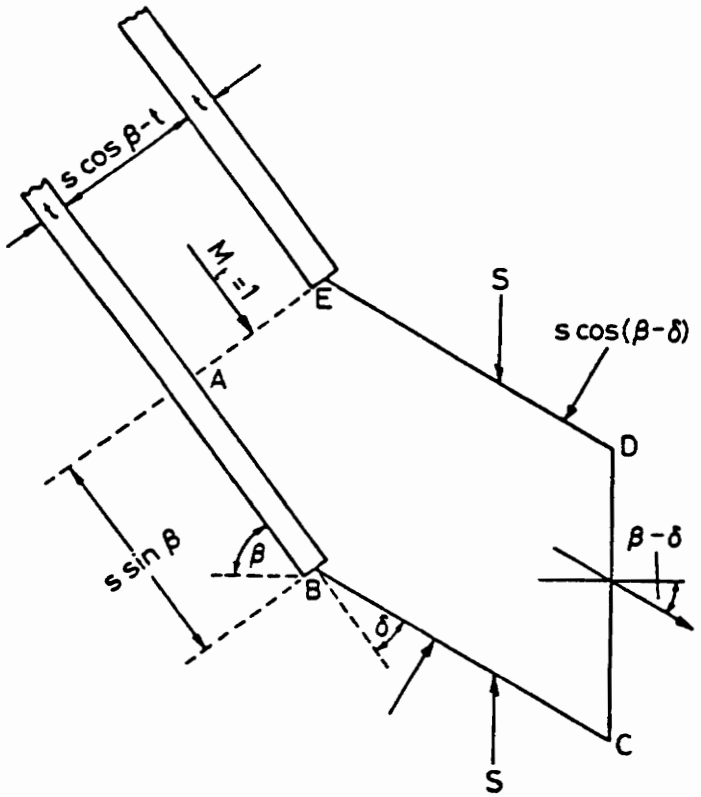

Control volume for a staggered trailing edge

Figure 4. Control Volume Model of Denton & Xu from Ref. [3]

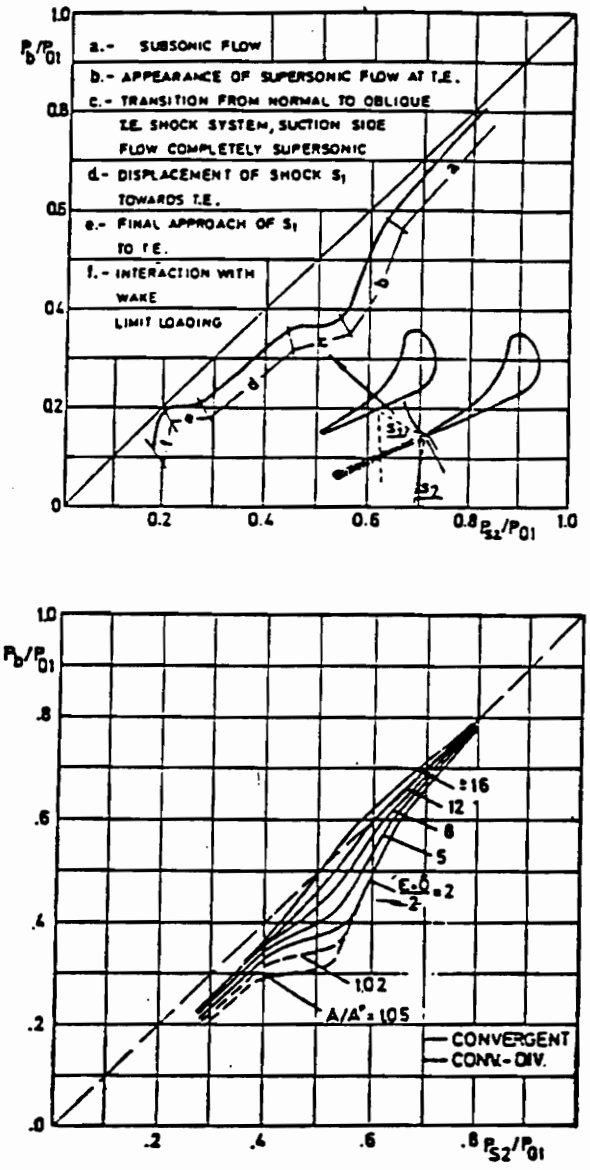

Figure 5. Base Pressure Correlation of Sieverding from Ref. [16]

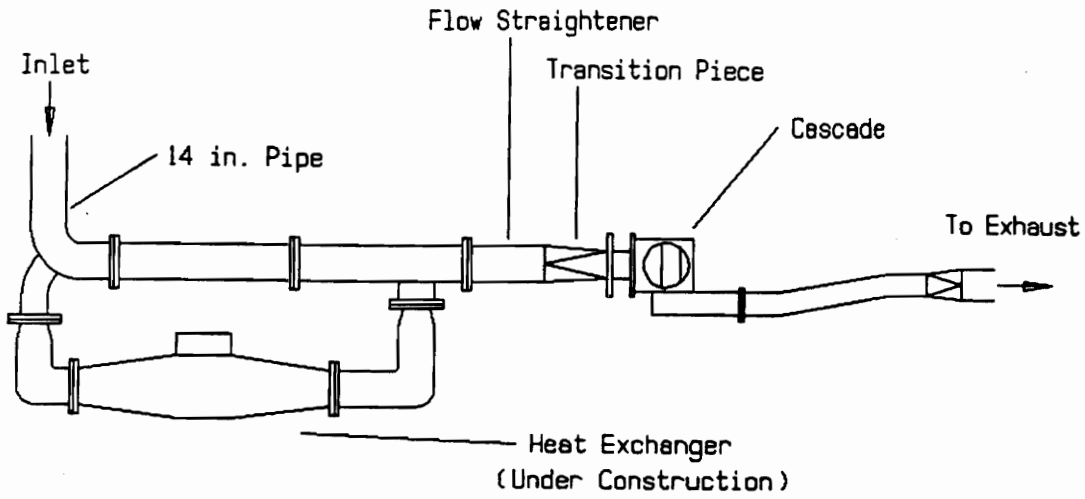

Figure 6. Schematic of the Wind Tunnel

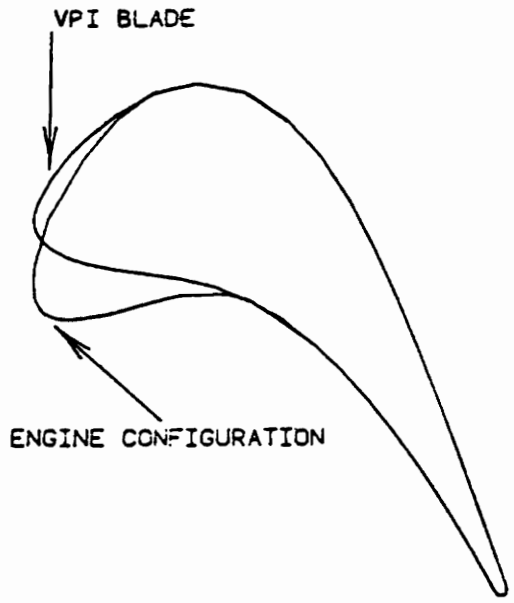

Figure 7. Comparison of Engine Blade and VPI Blade from Ref. [17]

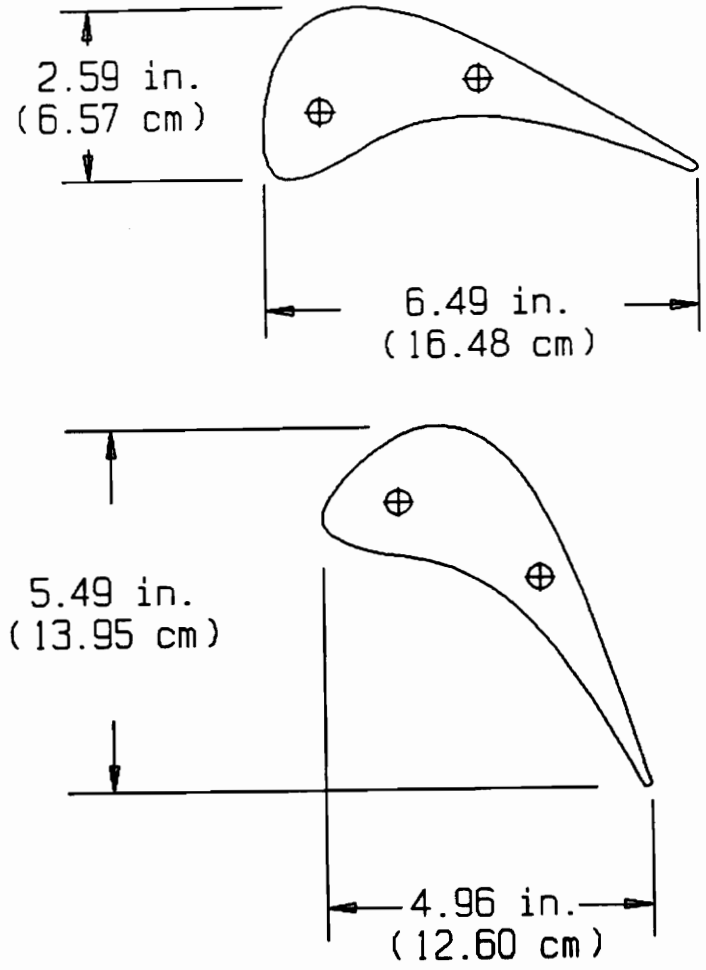

Figure 8. Dimensions of the Large Scale Blade

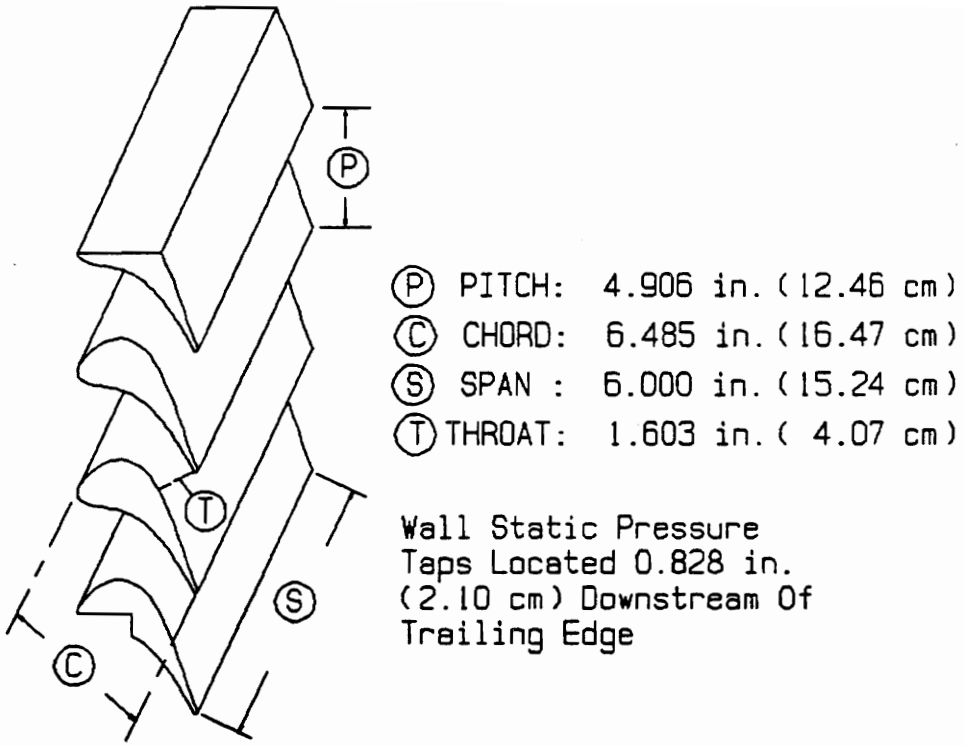

Figure 9. Basic Cascade Dimensions

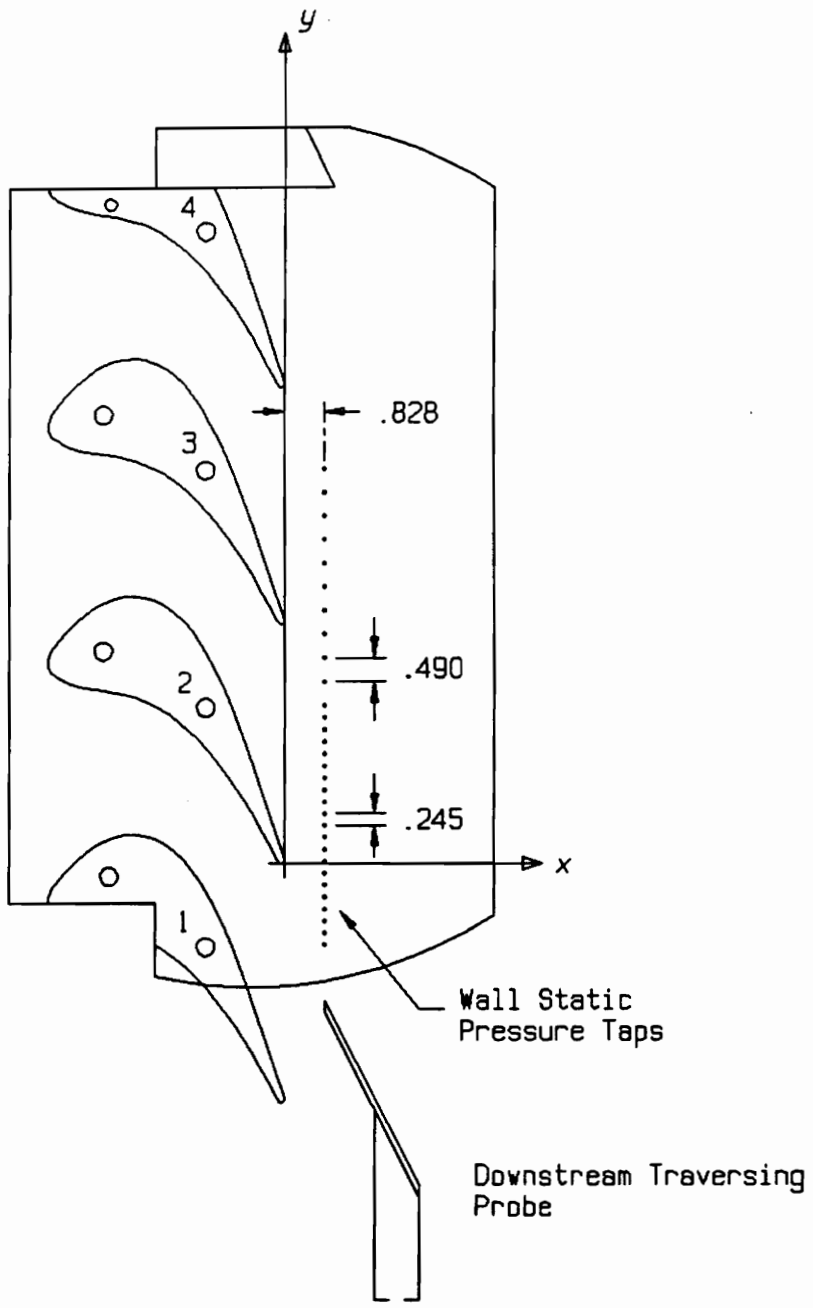

Figure 10. Profile of the Cascade

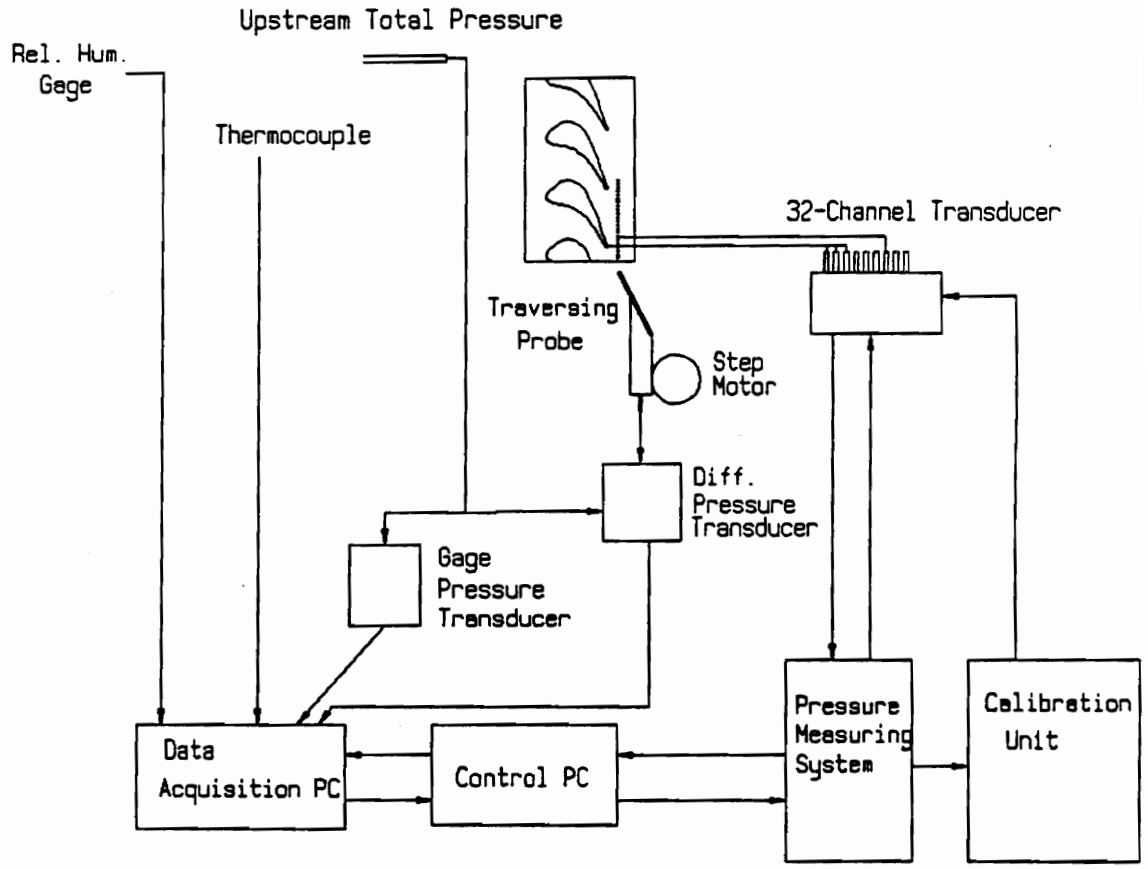

Figure 11. Schematic of the Measuring System

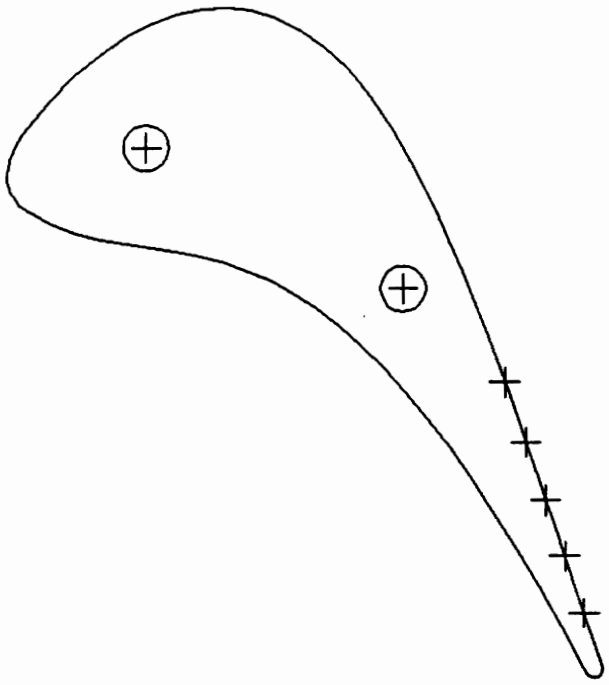

DISTANCE FROM FIRST TRAILING
EDGE TAP ON SUCTION SIDE

1	2.47" (6.27 cm)	83.7% AXIAL CHORD
2	1.95" (4.95 cm)	87.3%
3	1.45" (3.68 cm)	90.6%
4	0.97" (2.46 cm)	93.7%
5	0.47" (1.19 cm)	96.9%

Figure 12. Suction Side Tap Positions

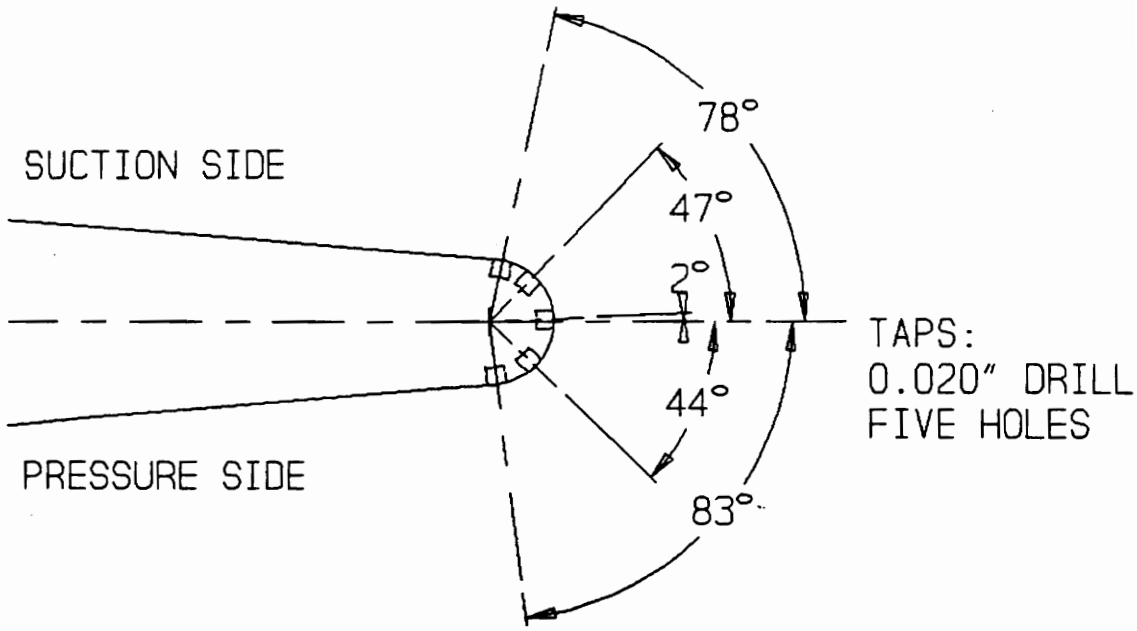

Figure 13. Trailing Edge Tap Positions

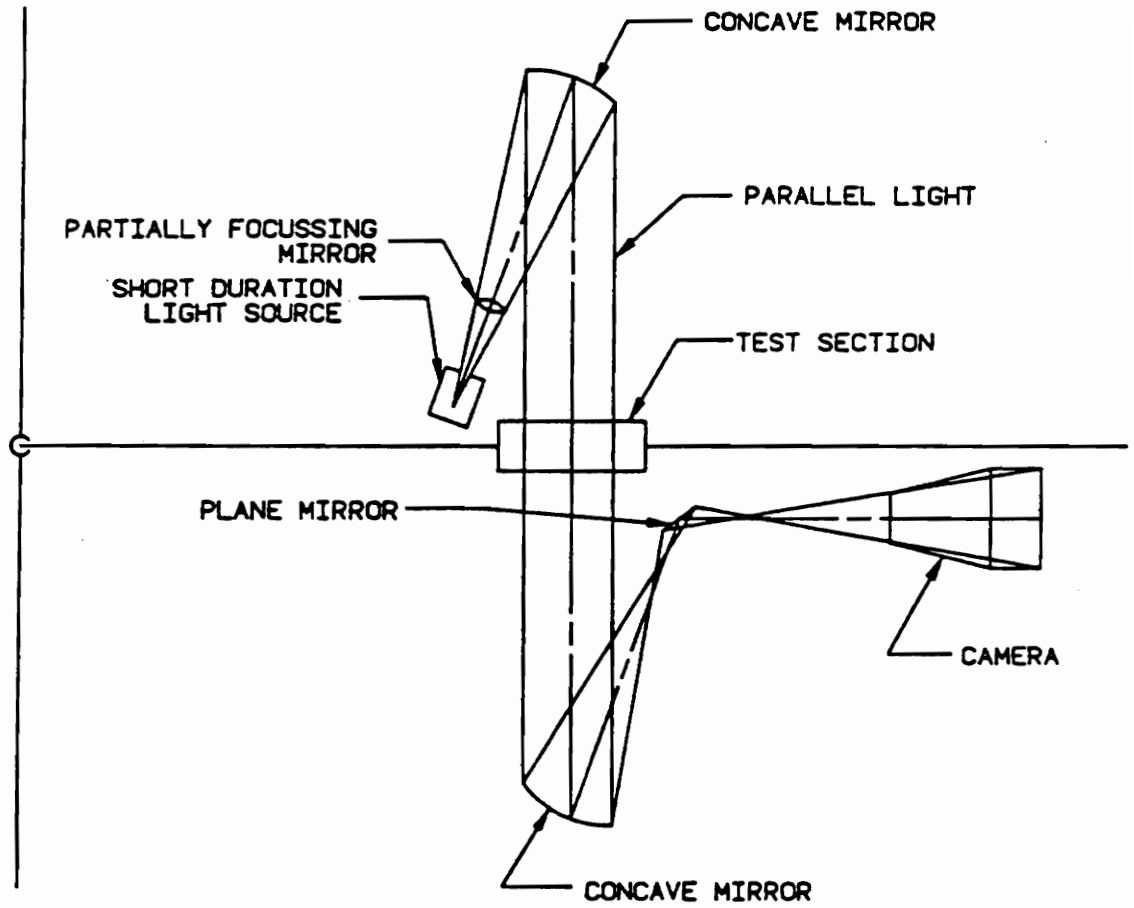

Figure 14. Schematic of the Shadowgraph Setup from Ref. [30]

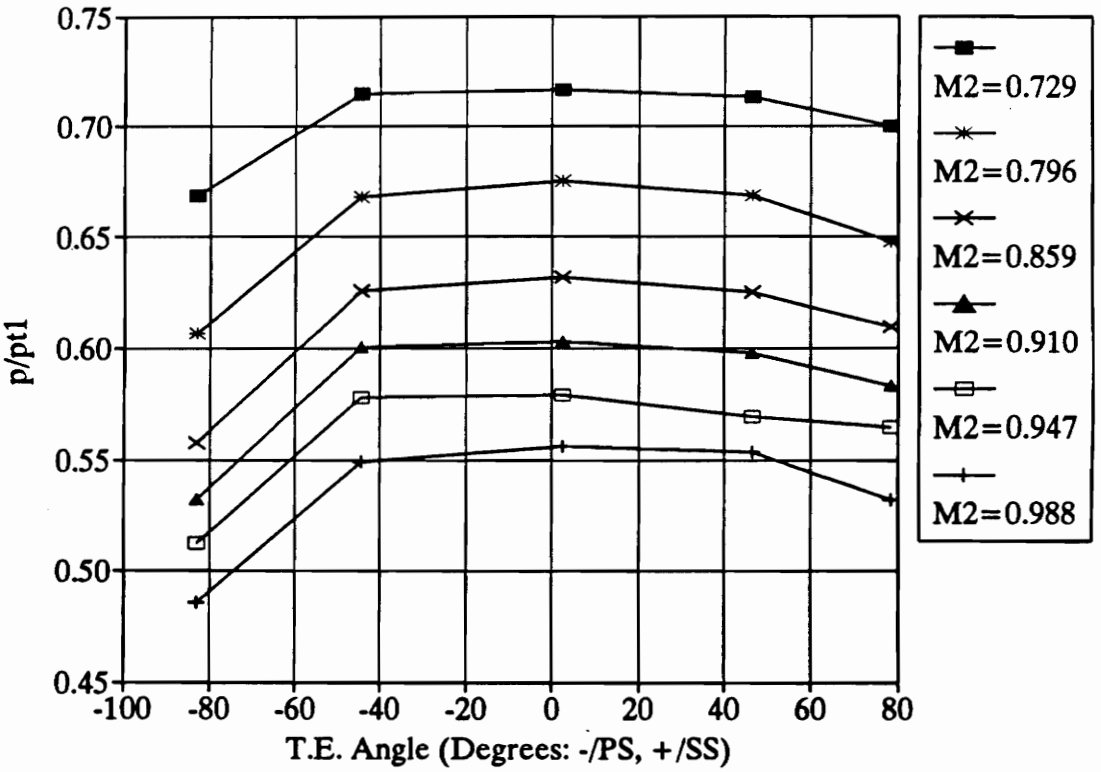

Figure 15. Base Pressure Distribution for Subsonic Exit Mach Numbers

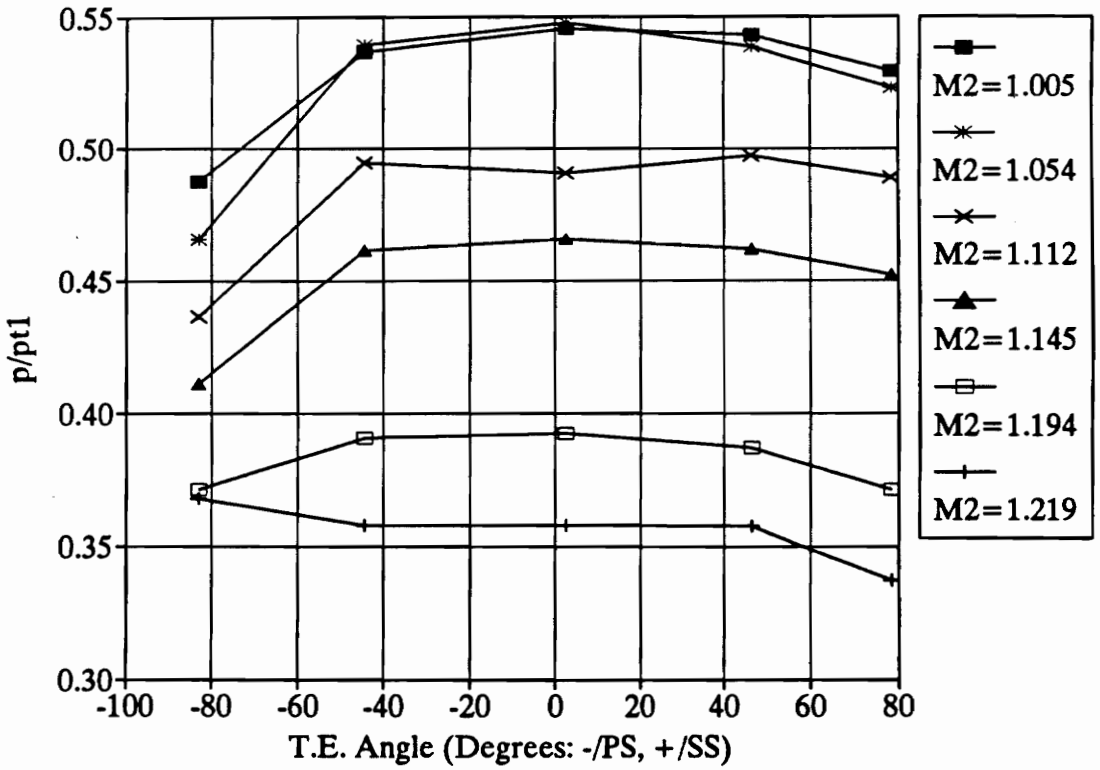

Figure 16. Base Pressure Distribution for Low Supersonic Exit Mach Numbers

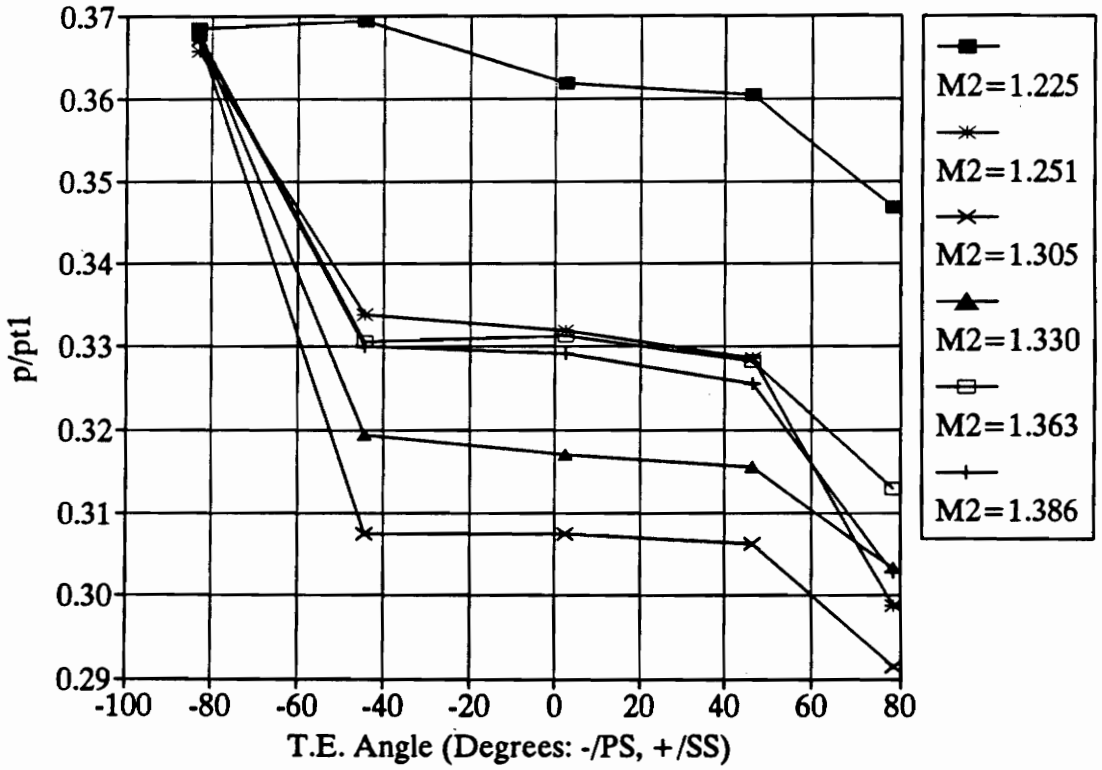

Figure 17. Base Pressure Distribution for Higher Exit Mach Numbers

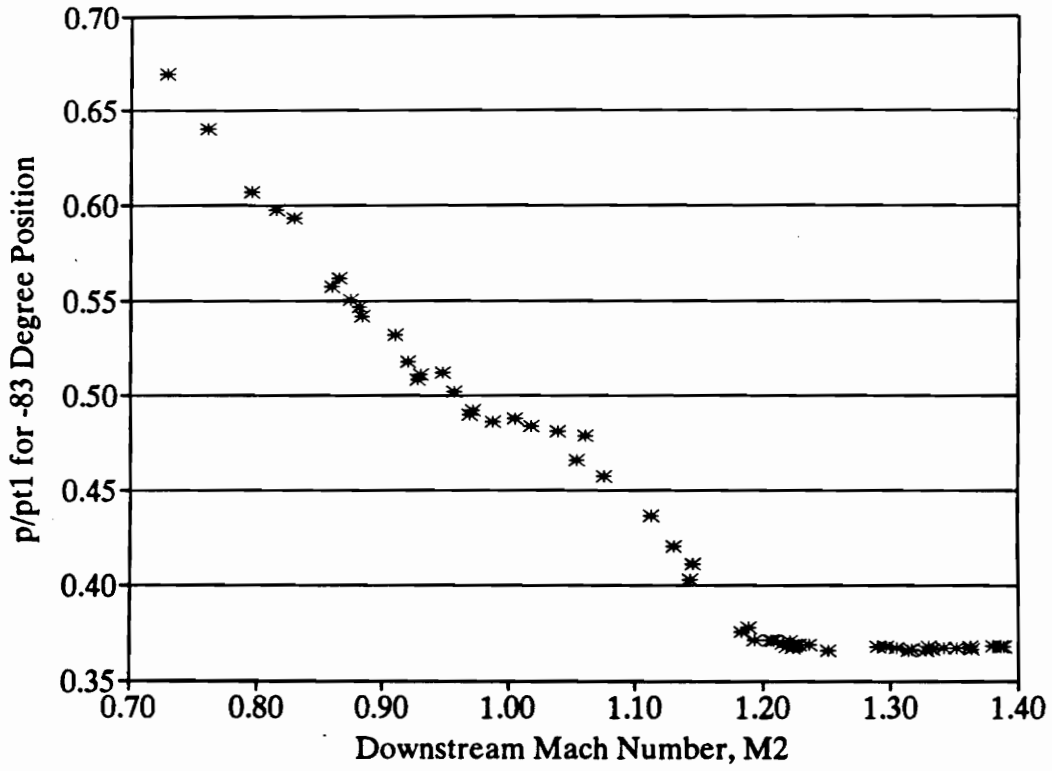

Figure 18. Pressure at the -83° Position Versus Exit Mach Number

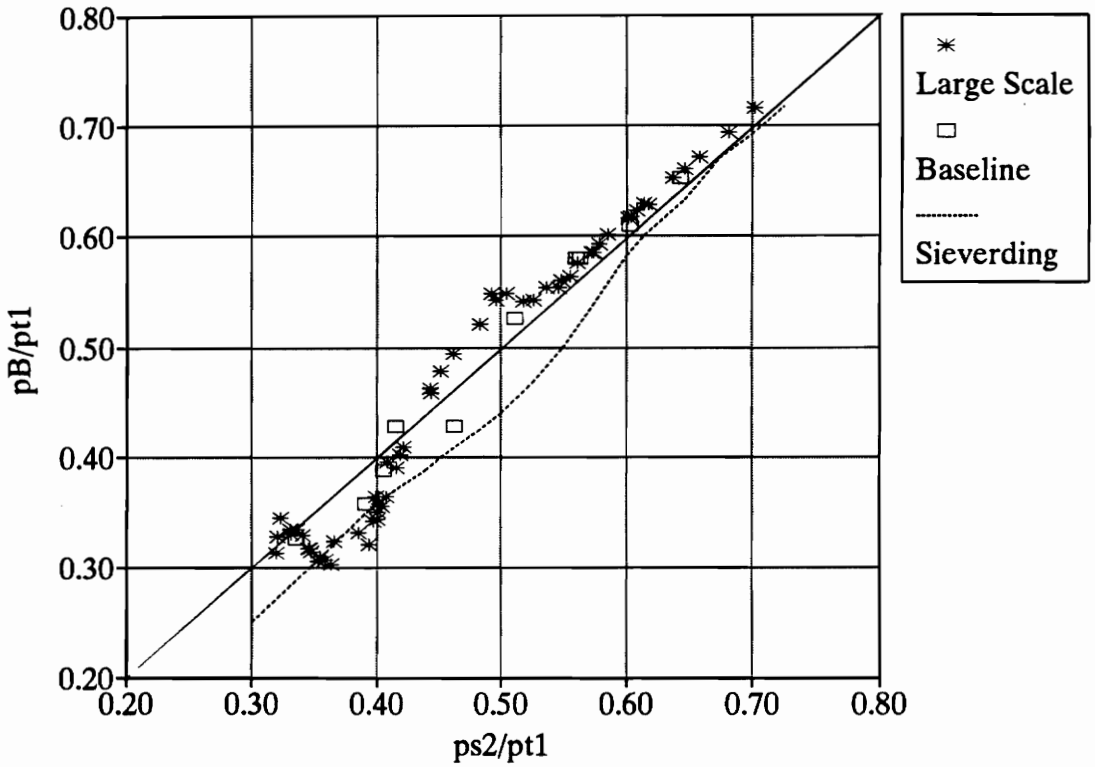

Figure 19. Base Pressure Versus Downstream Pressure

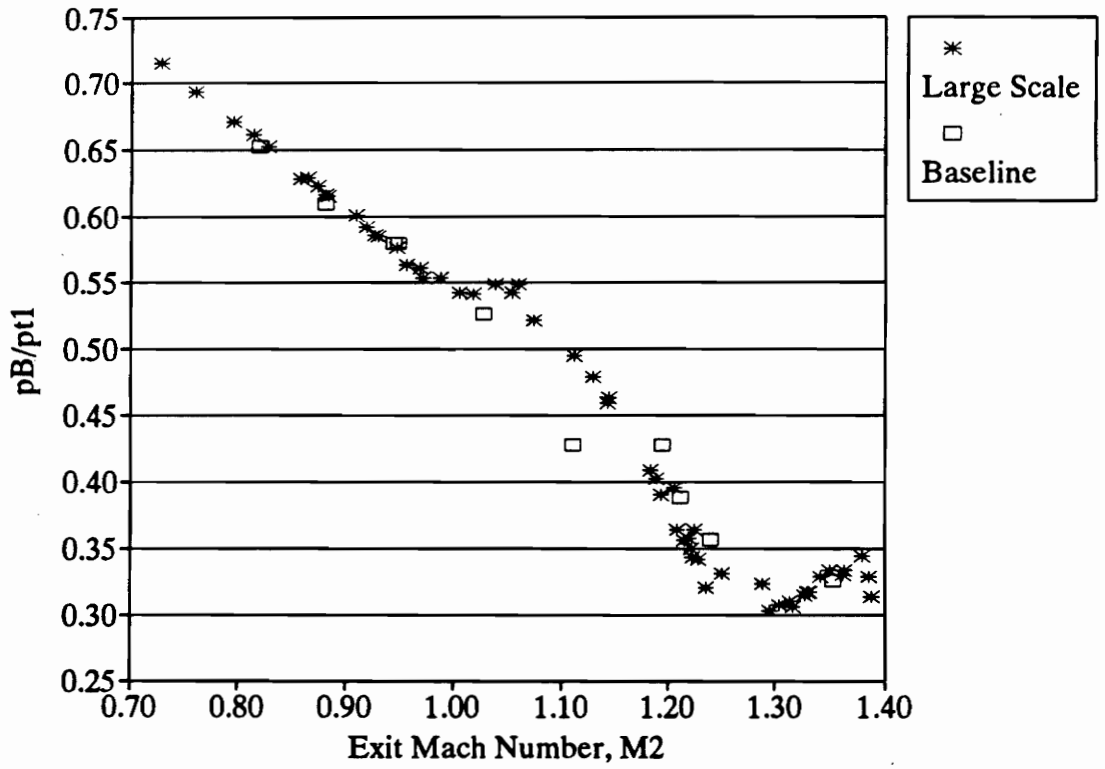

Figure 20. Base Pressure Versus Downstream Mach Number

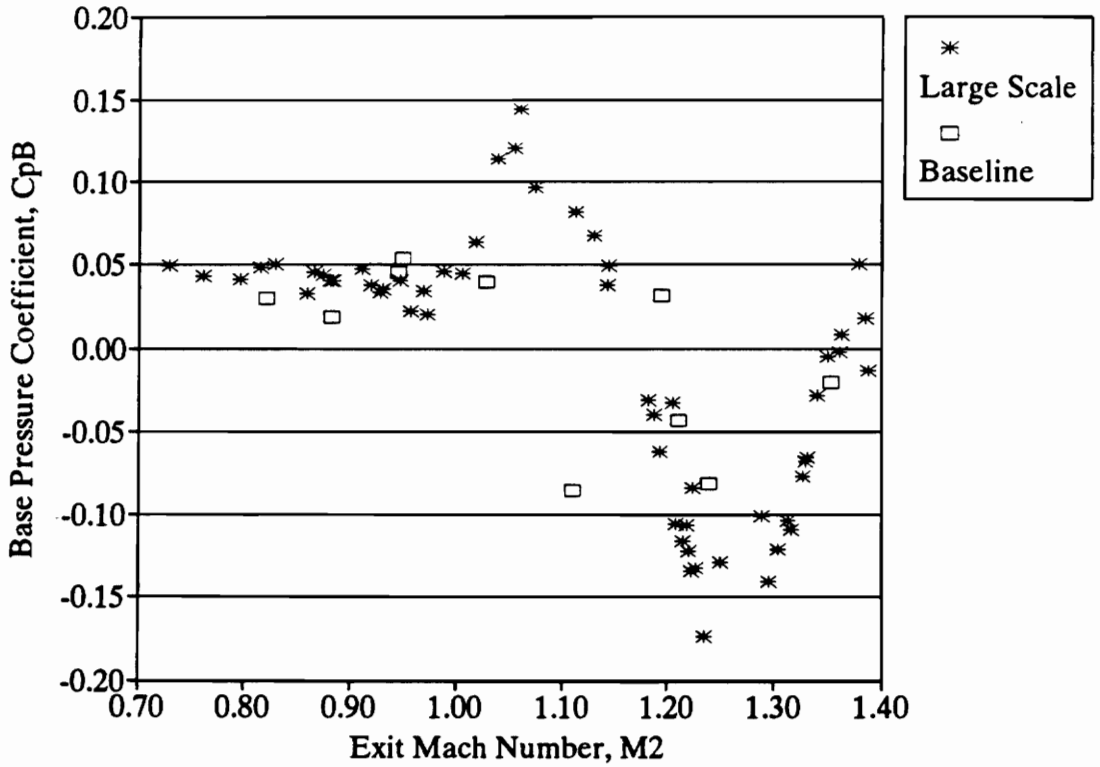

Figure 21. Base Pressure Coefficient Versus Downstream Mach Number

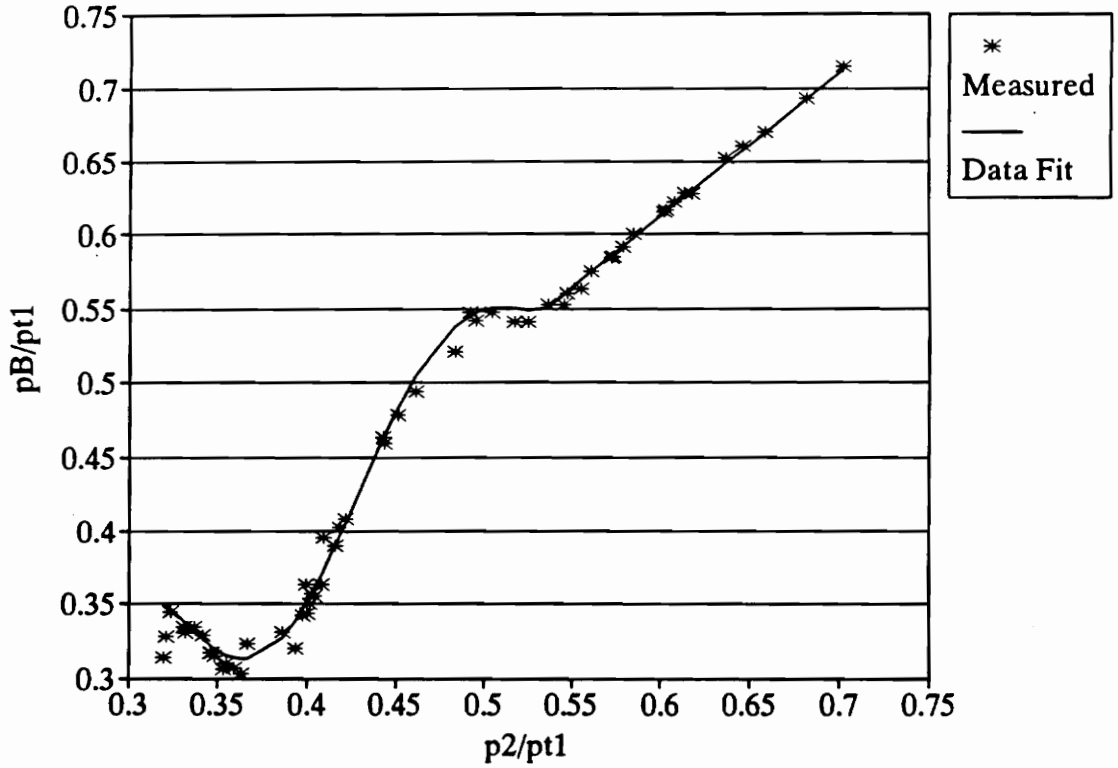

Figure 22. Data Fit of the Measured Base Pressures

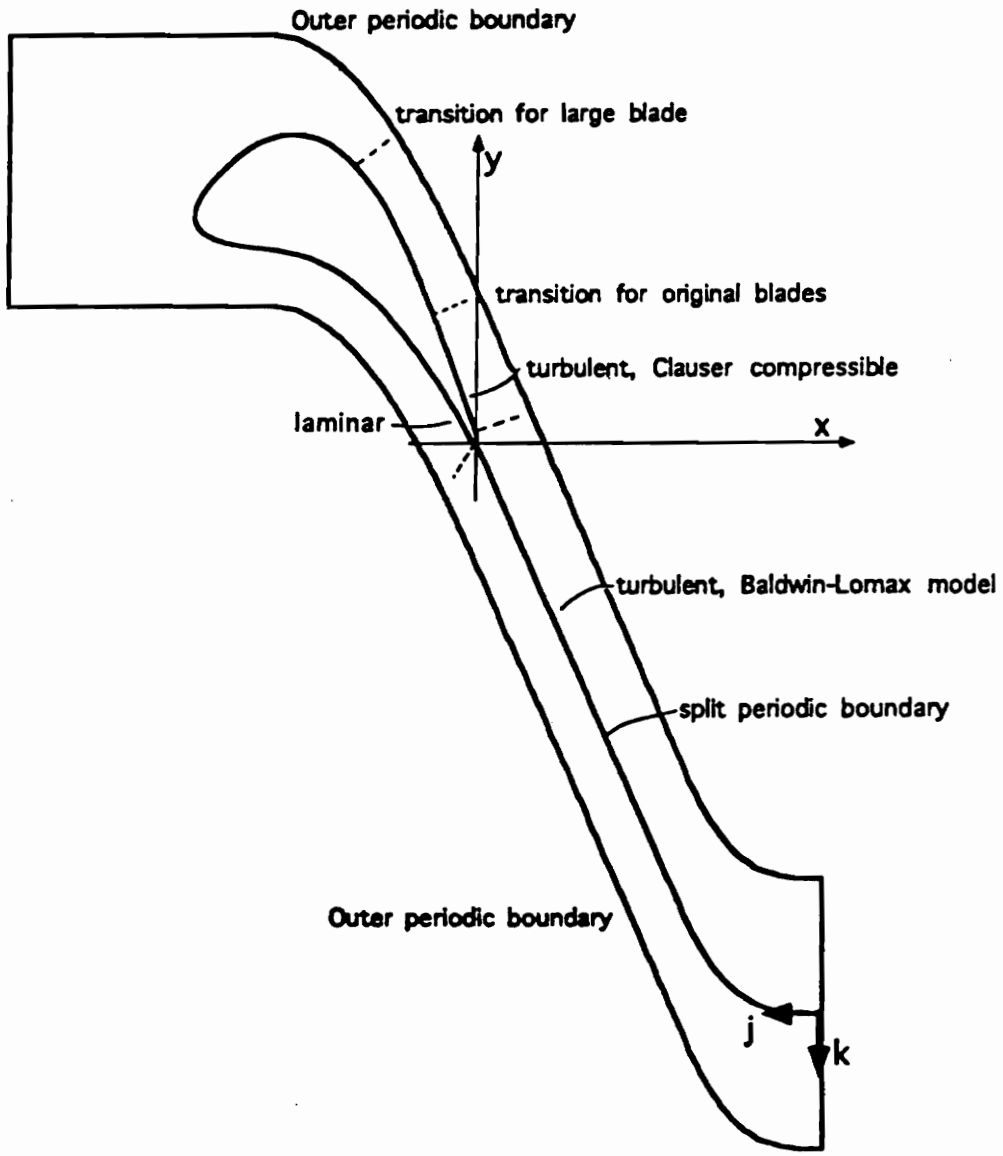

Figure 23. Computational Domain and Turbulence Model of Kiss [31]

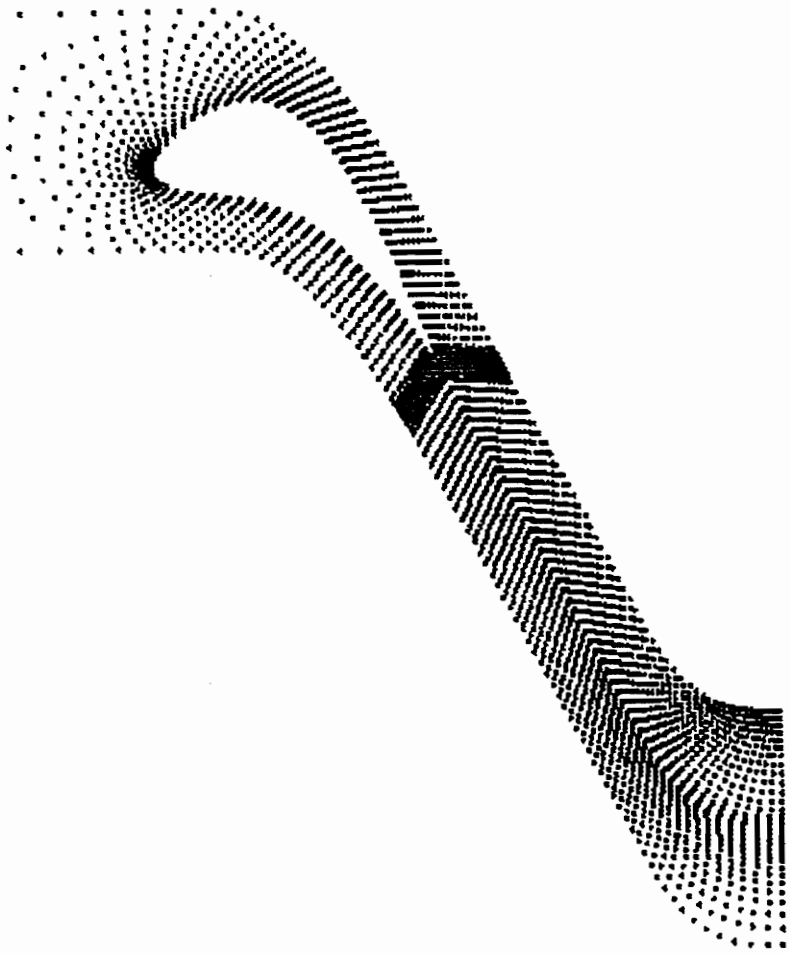

Figure 24. Grid Points Used in Large Scale Cascade Flow Computation

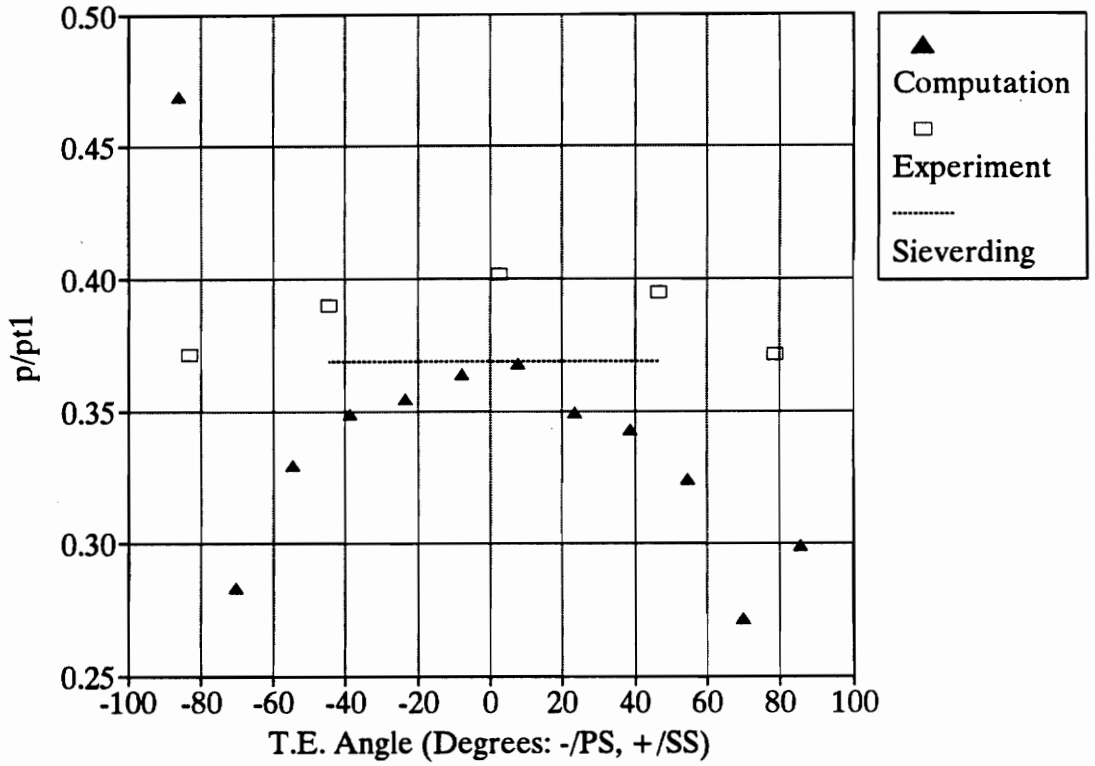

Figure 25. Computed Base Pressure Distribution for M_2 = 1.2

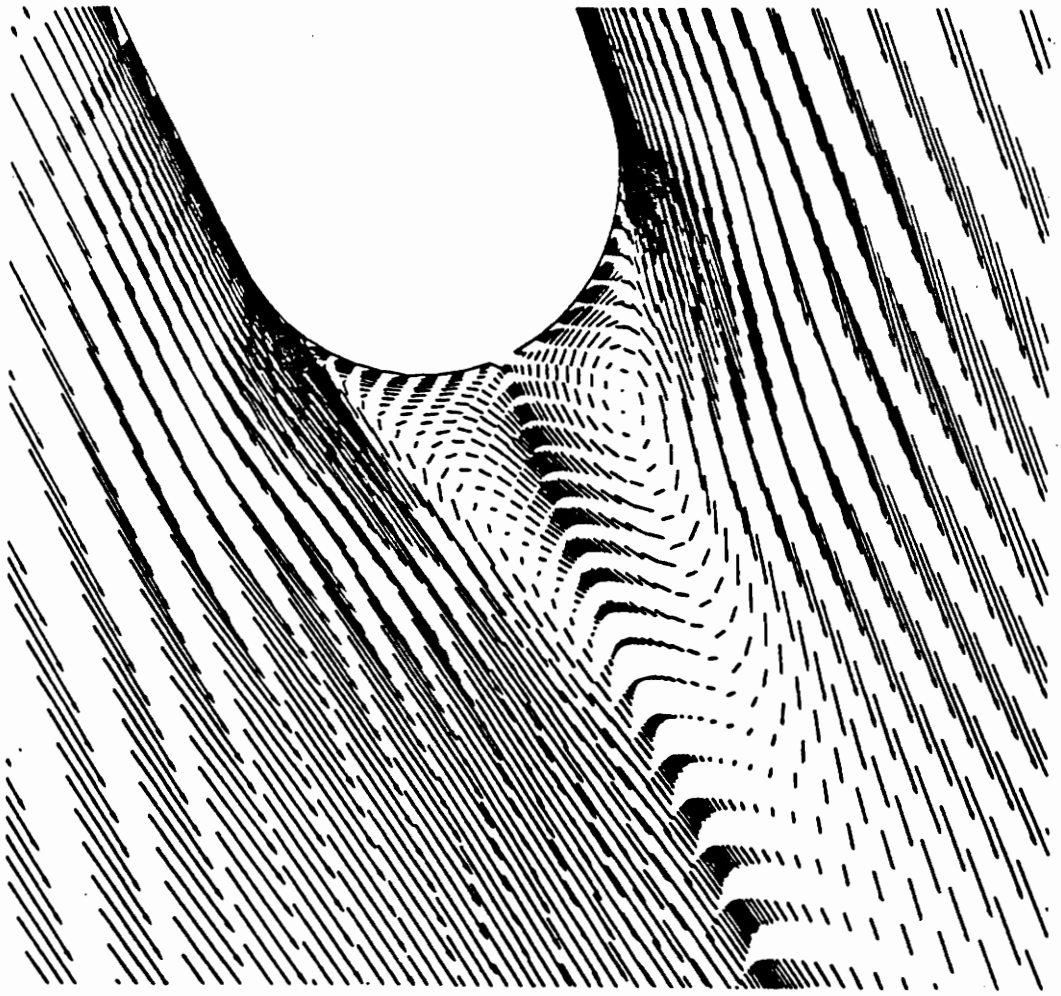

Figure 26. Computed Velocity Vectors at the Trailing Edge (Baseline Blade) from Ref. [31]

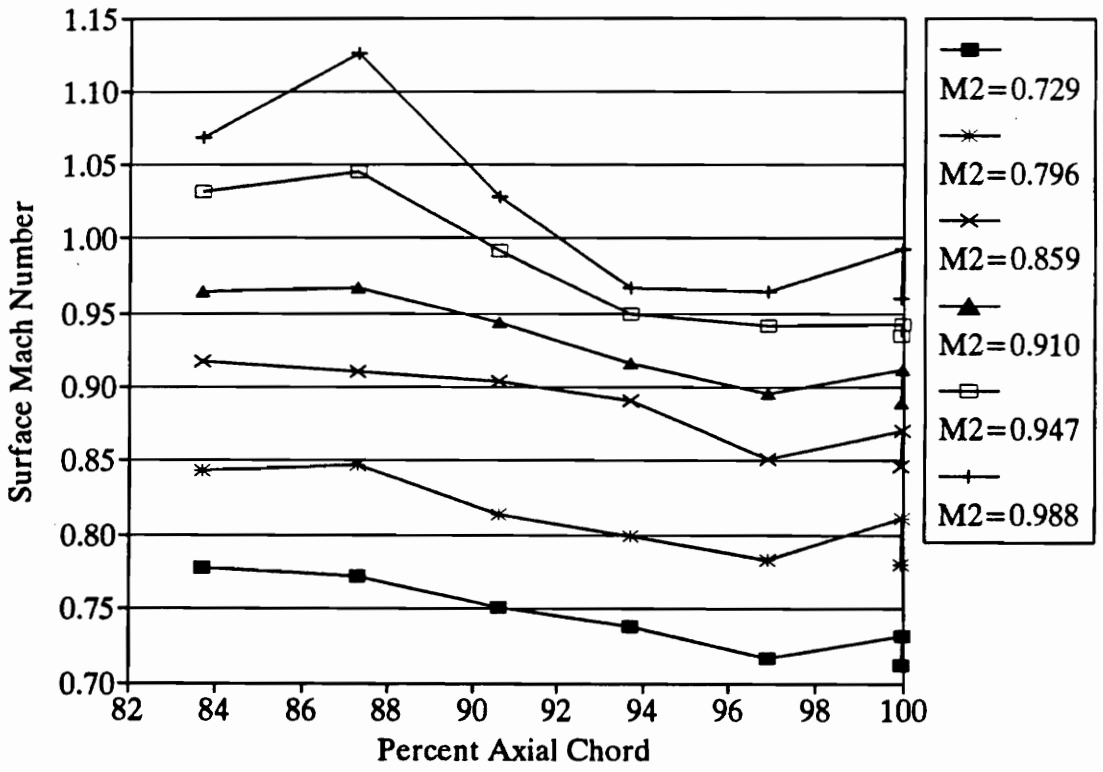

Figure 27. Suction Surface Mach Numbers for Subsonic Exit Mach Numbers

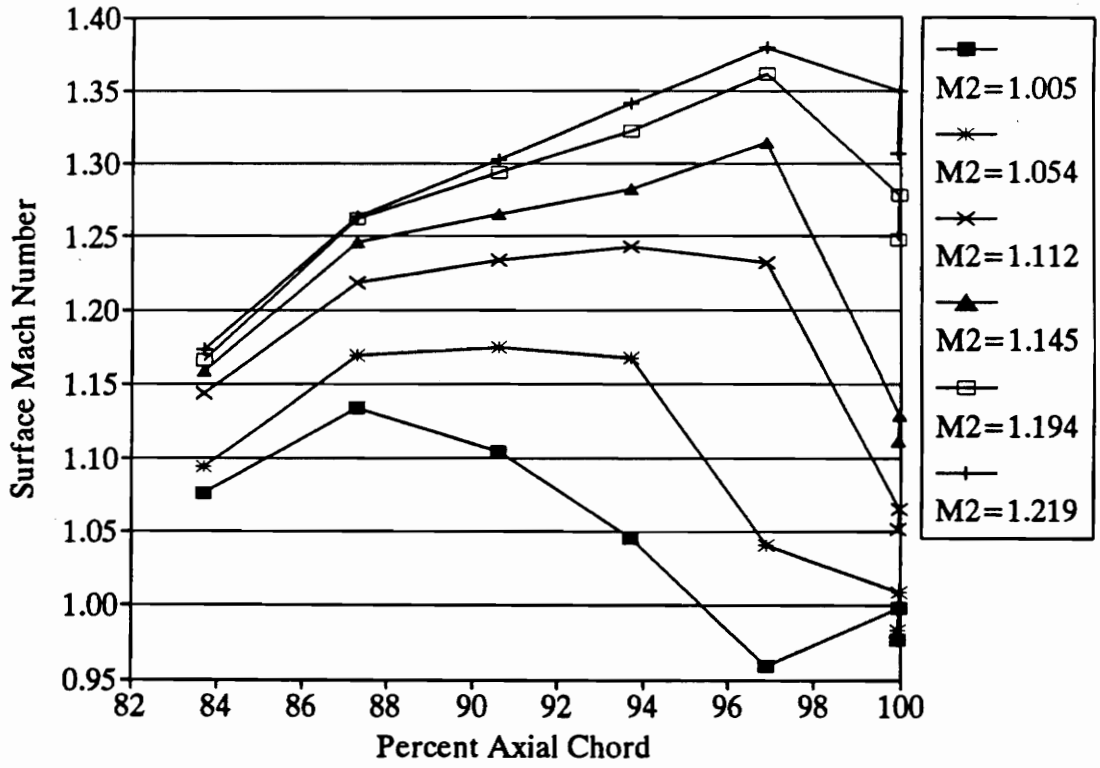

Figure 28. Suction Surface Mach Numbers for Low Supersonic Exit Mach Numbers

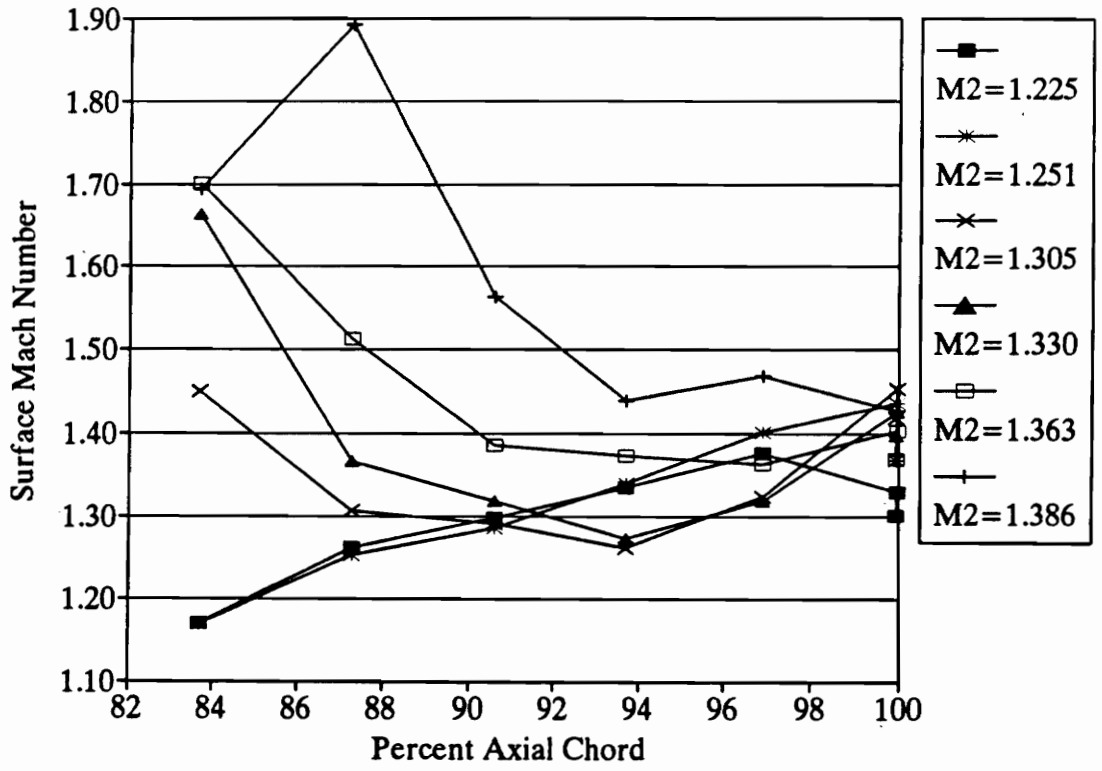

Figure 29. Suction Surface Mach Numbers for Higher Supersonic Exit Mach Numbers

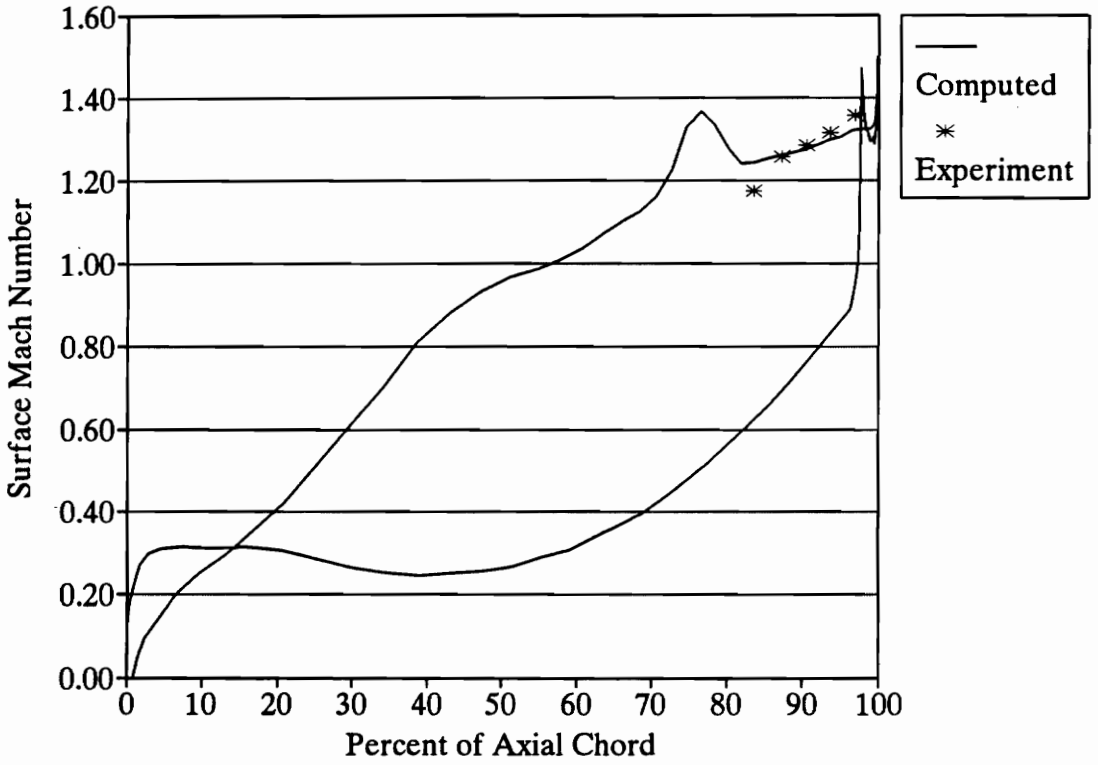

Figure 30. Computed Blade Mach Number Distribution for M_2 = 1.2

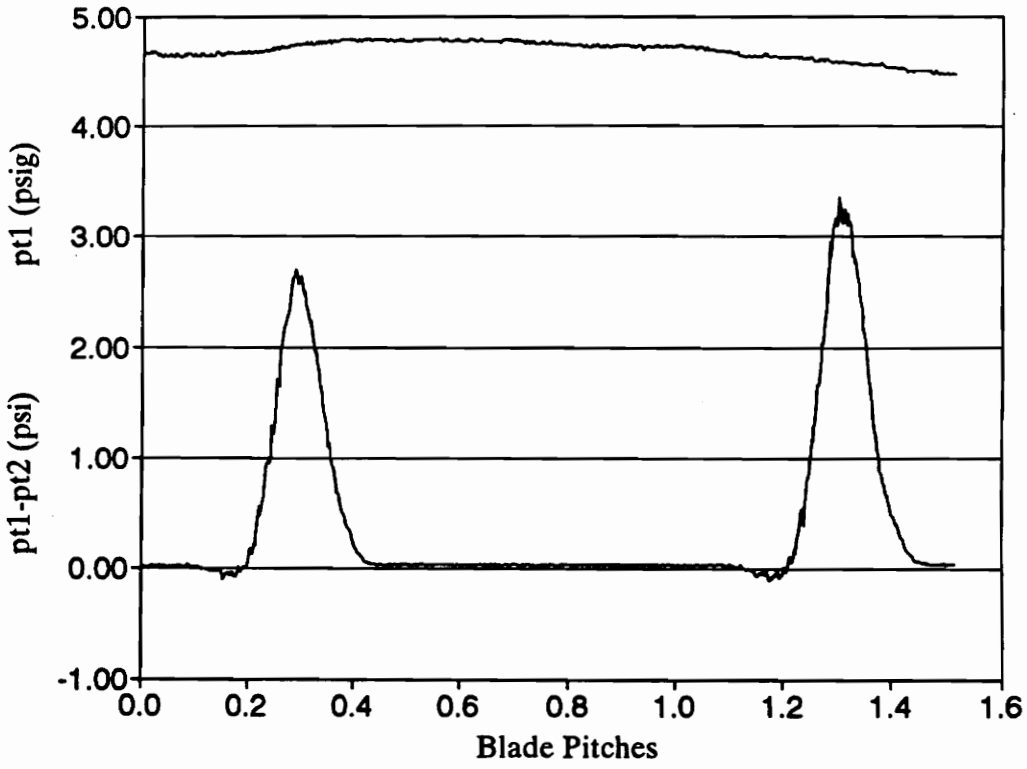

Figure 31. Output from Total Pressure Probes at M_2 = 0.89

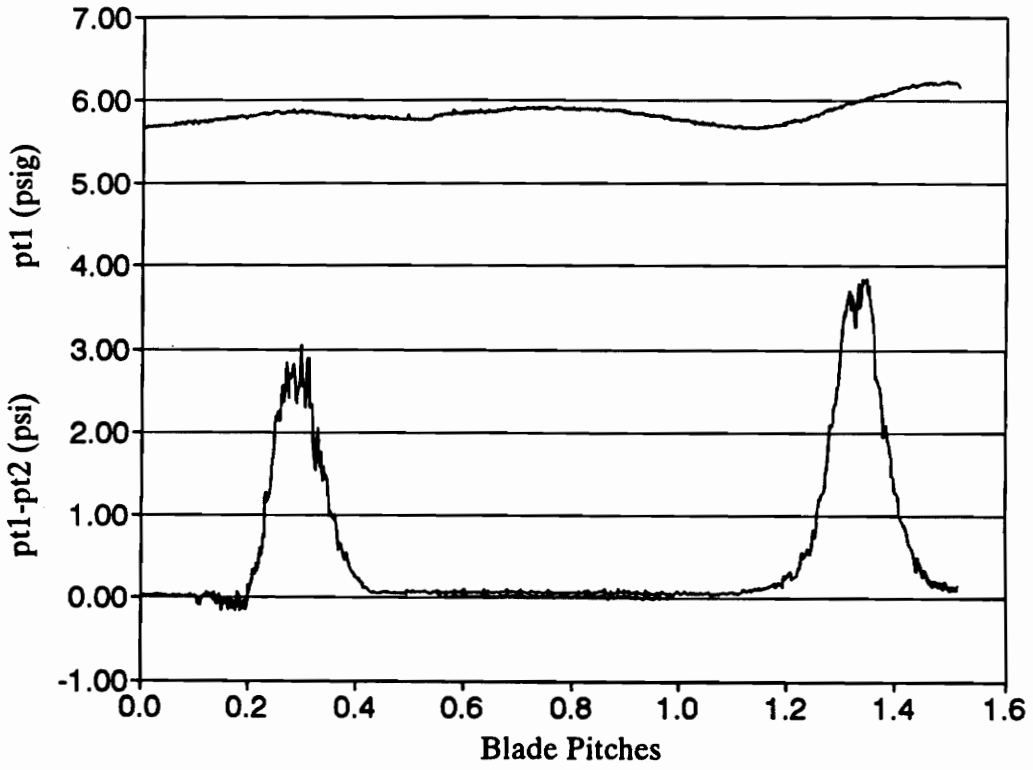

Figure 32. Output from Total Pressure Probes at M_2 = 1.01

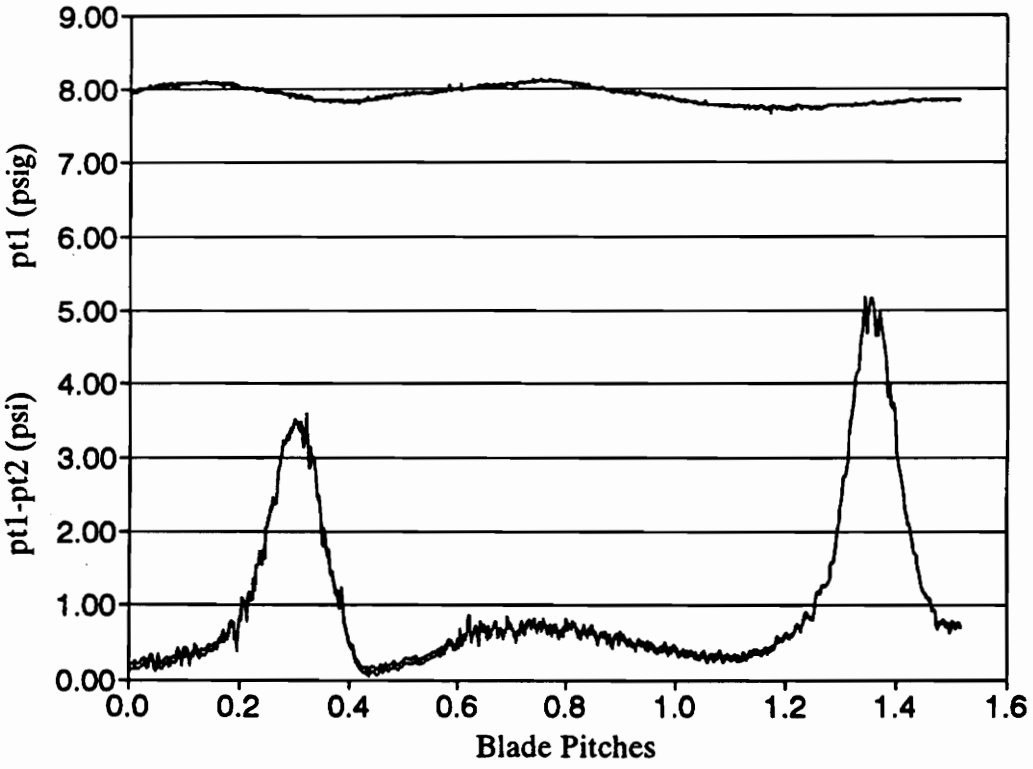

Figure 33. Output from Total Pressure Probes at M_2 = 1.17

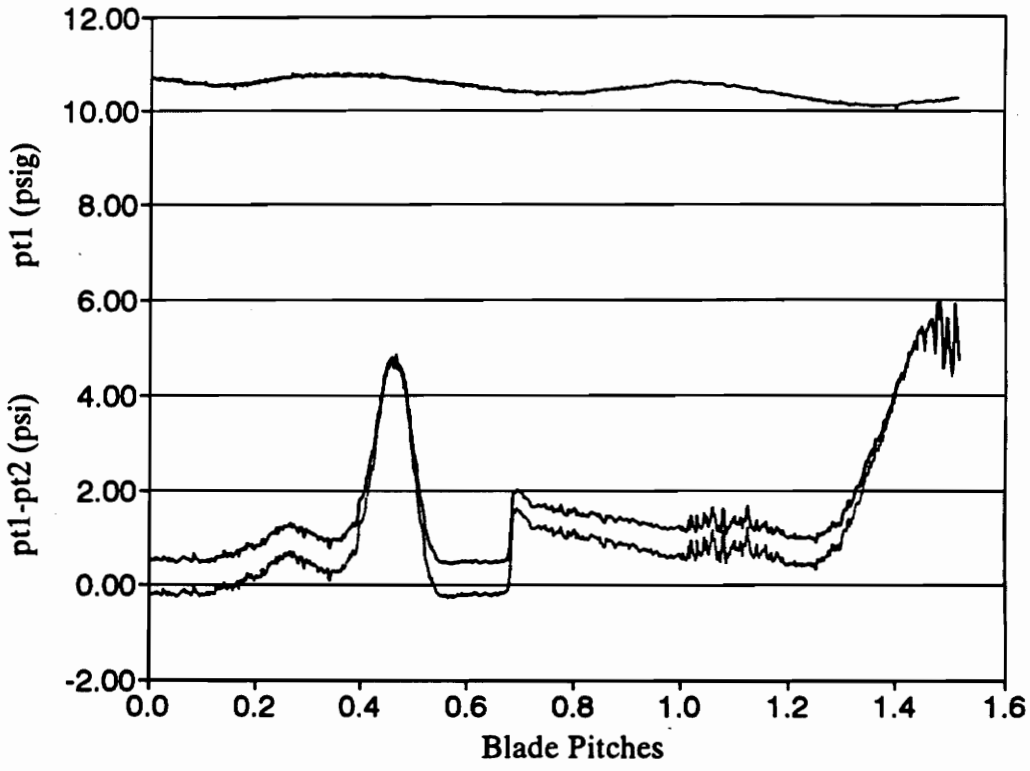

Figure 34. Output from Total Pressure Probes at M_2 = 1.33

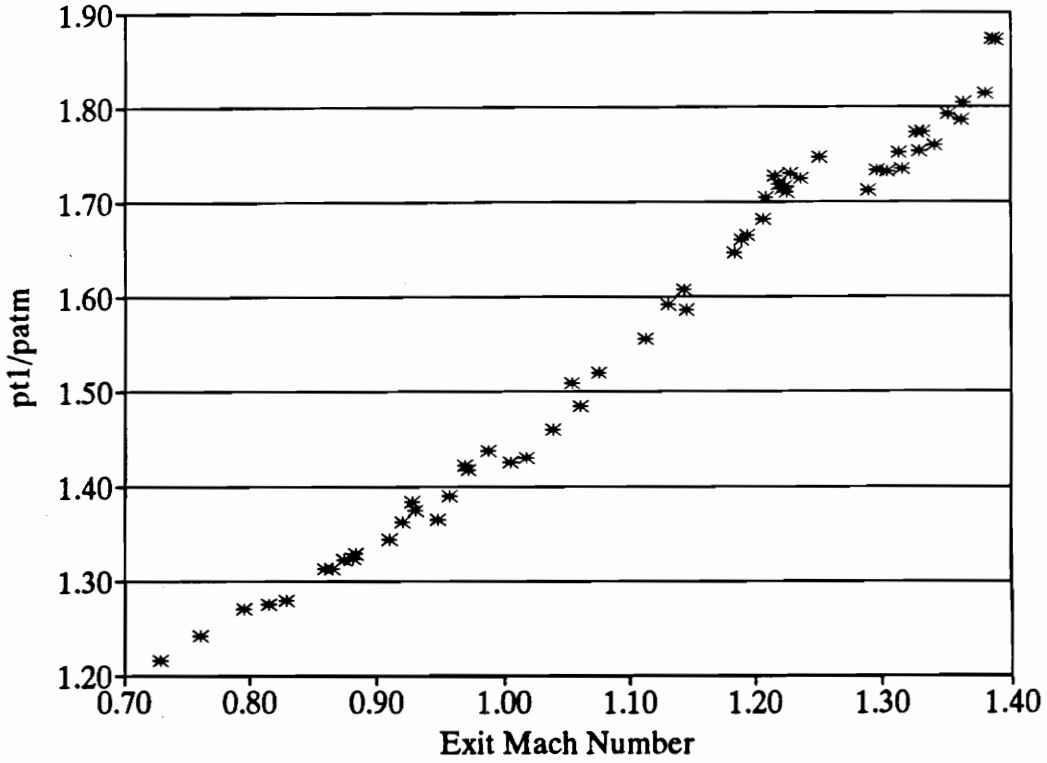

Figure 35. Mean Upstream Total Pressure Versus Exit Mach Number

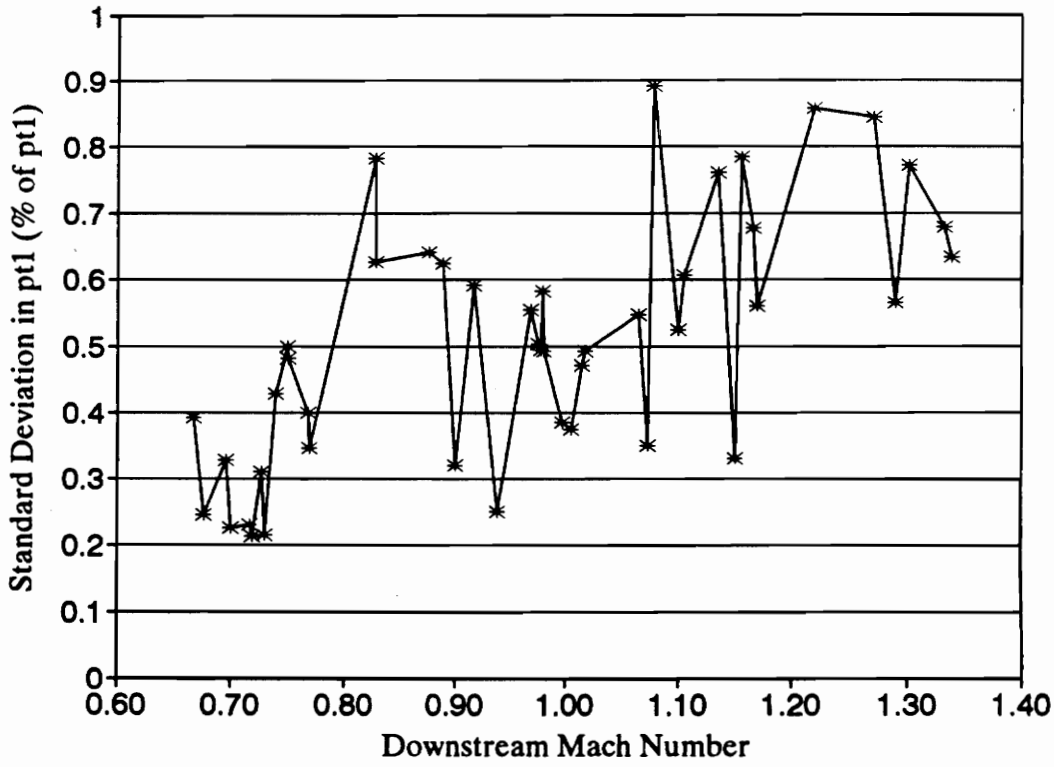

Figure 36. Standard Deviation in Upstream Total Pressure Versus Exit Mach Number

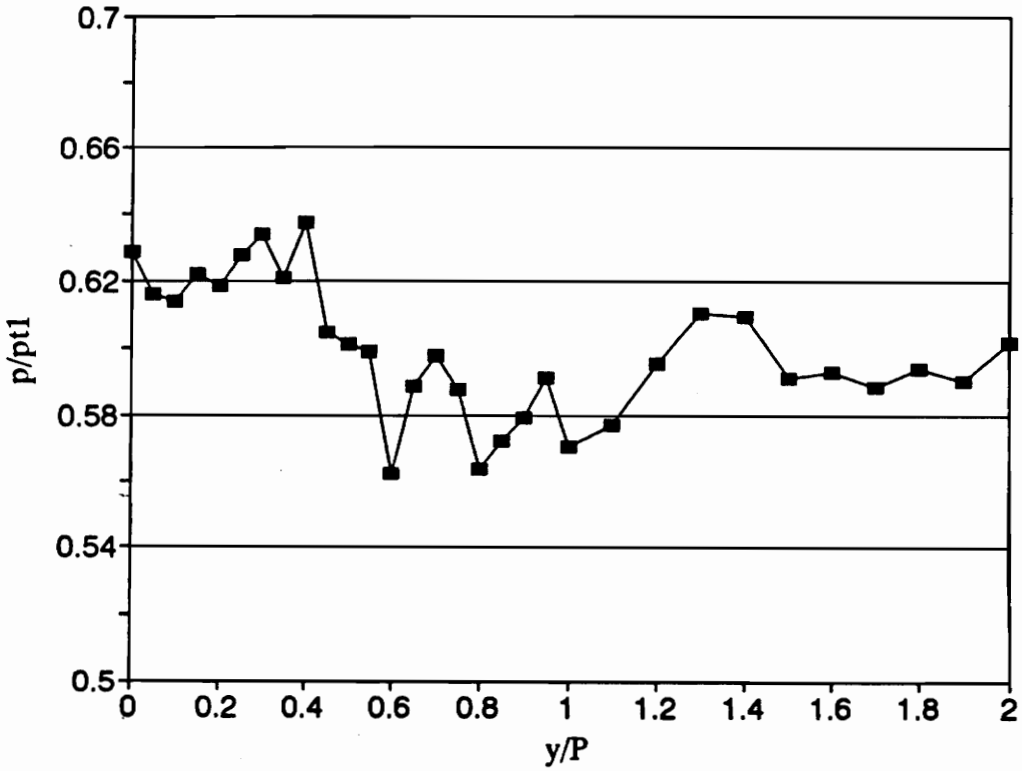

Figure 37. Endwall Static Pressure Distribution for $M_2 = 0.88$

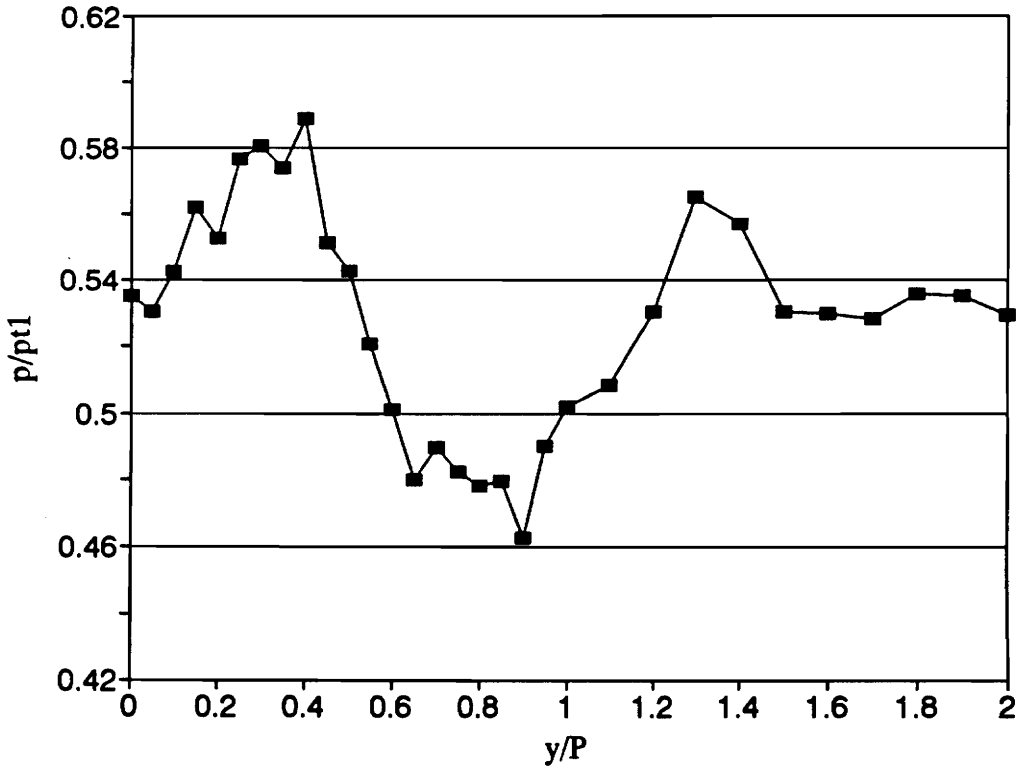

Figure 38. Endwall Static Pressure Distribution for M_2 = 1.01

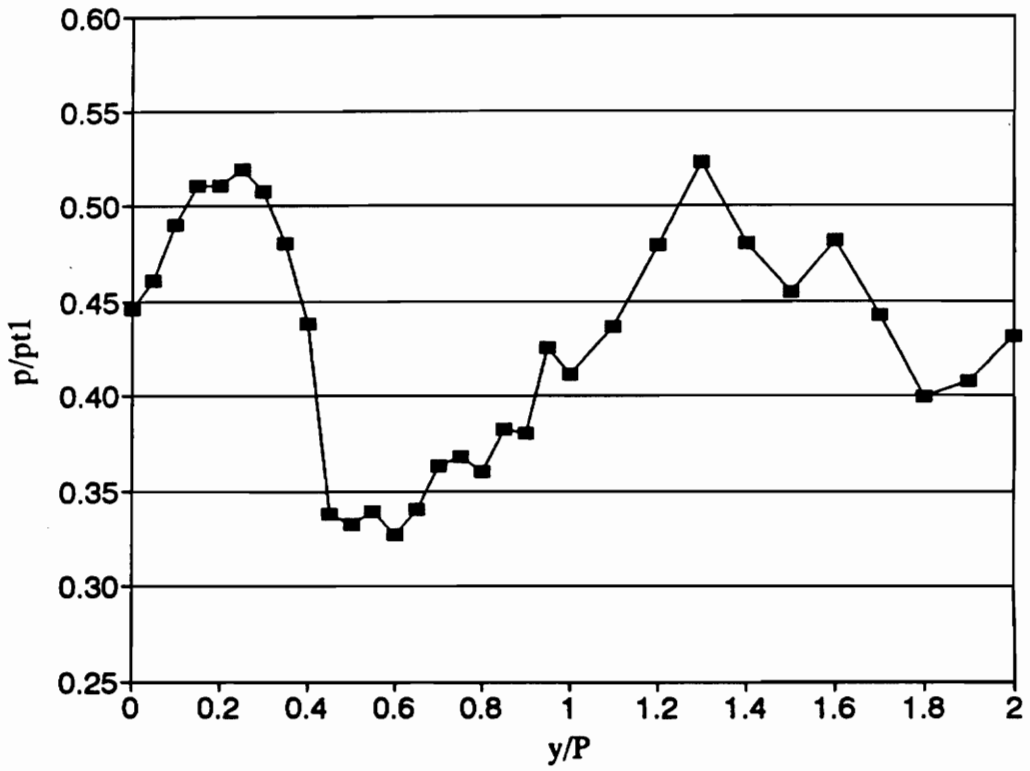

Figure 39. Endwall Static Pressure Distribution for $M_2 = 1.19$

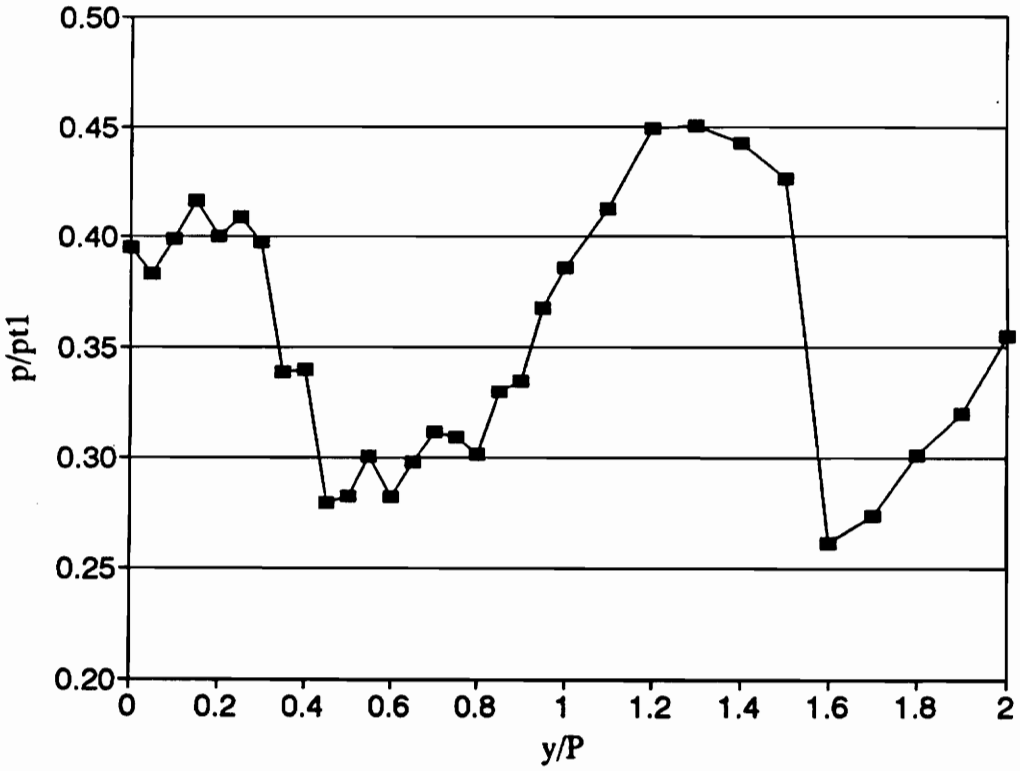

Figure 40. Endwall Static Pressure Distribution for M_2 = 1.33

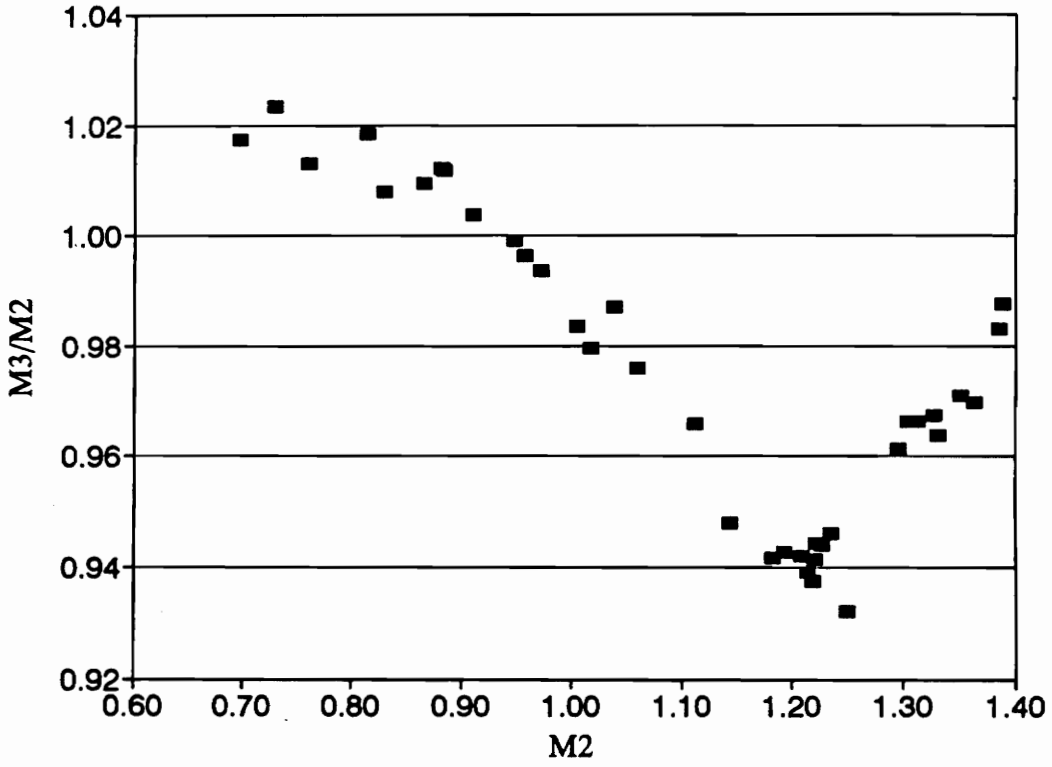

Figure 41. Mach Number Ratio, M_3/M_2, Versus Mach Number Behind Blade #2, M_2

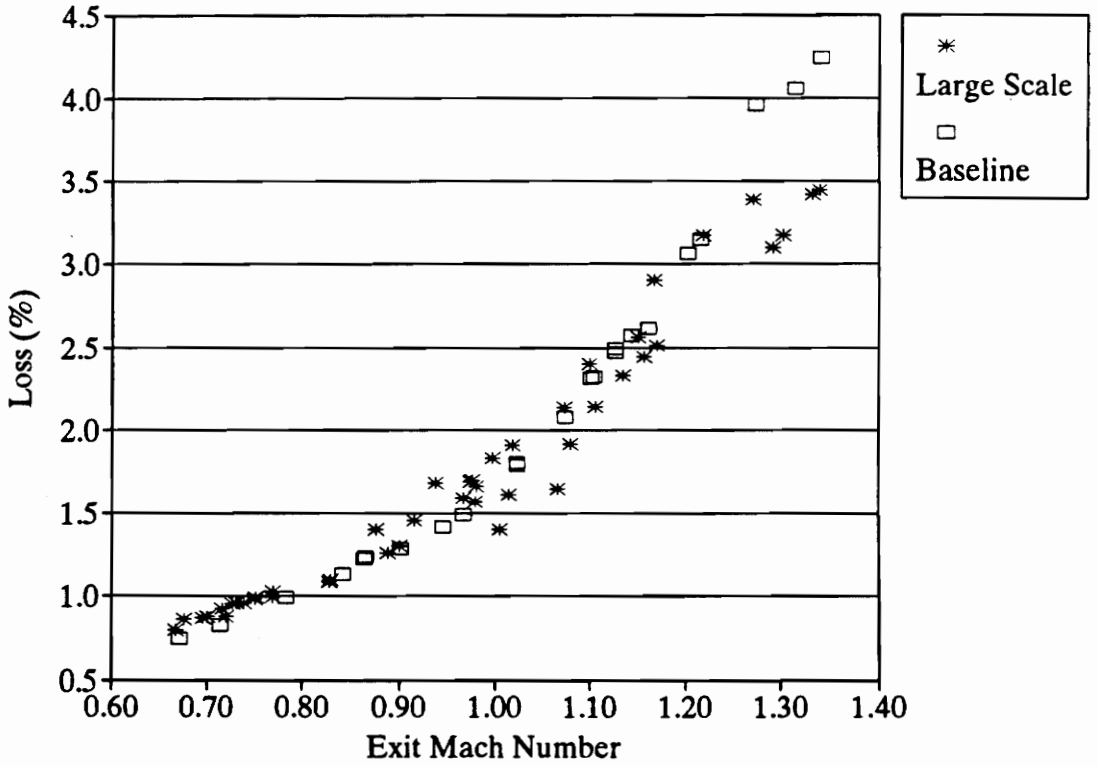

Figure 42. Loss Behind Blade #2 Versus Exit Mach Number

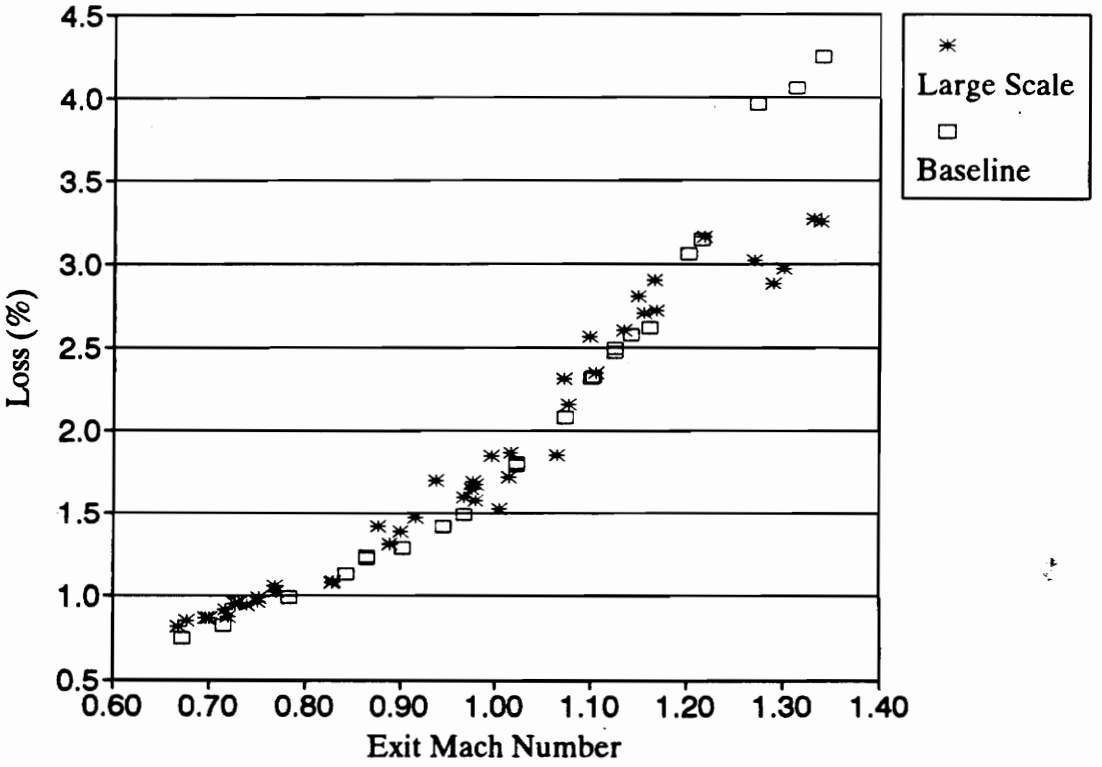

Figure 43. Average Loss Behind Blade #2 and #3 Versus Exit Mach Number

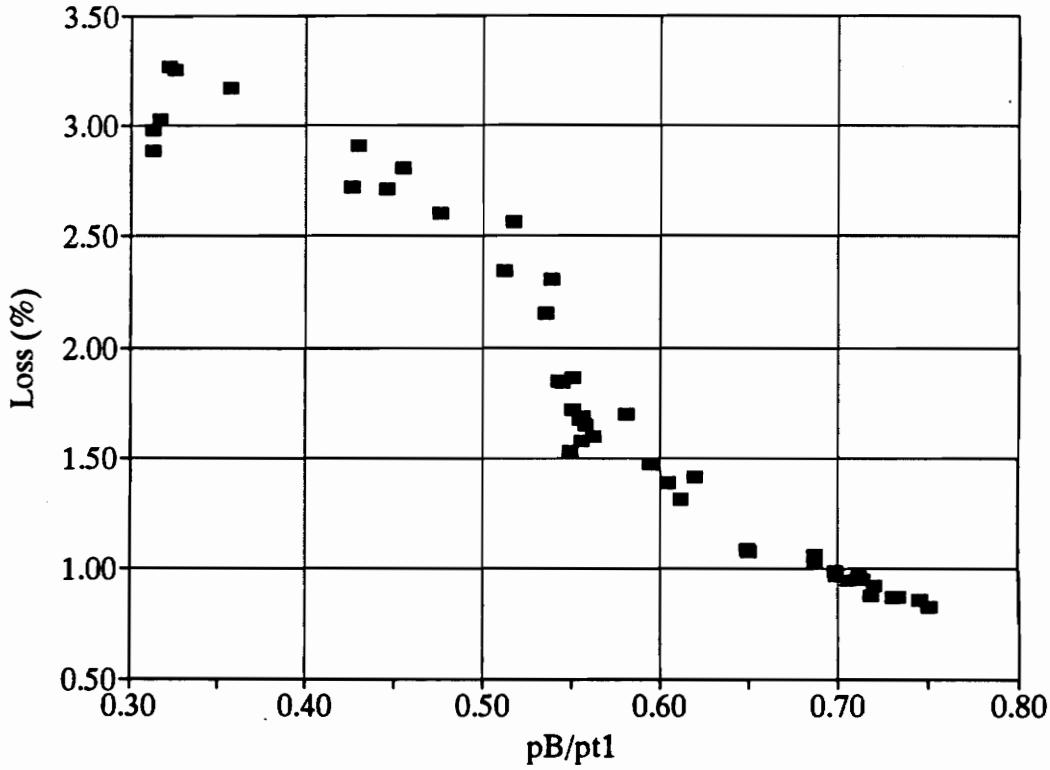

Figure 44. Profile Loss Behind Blade #2 Versus Base Pressure

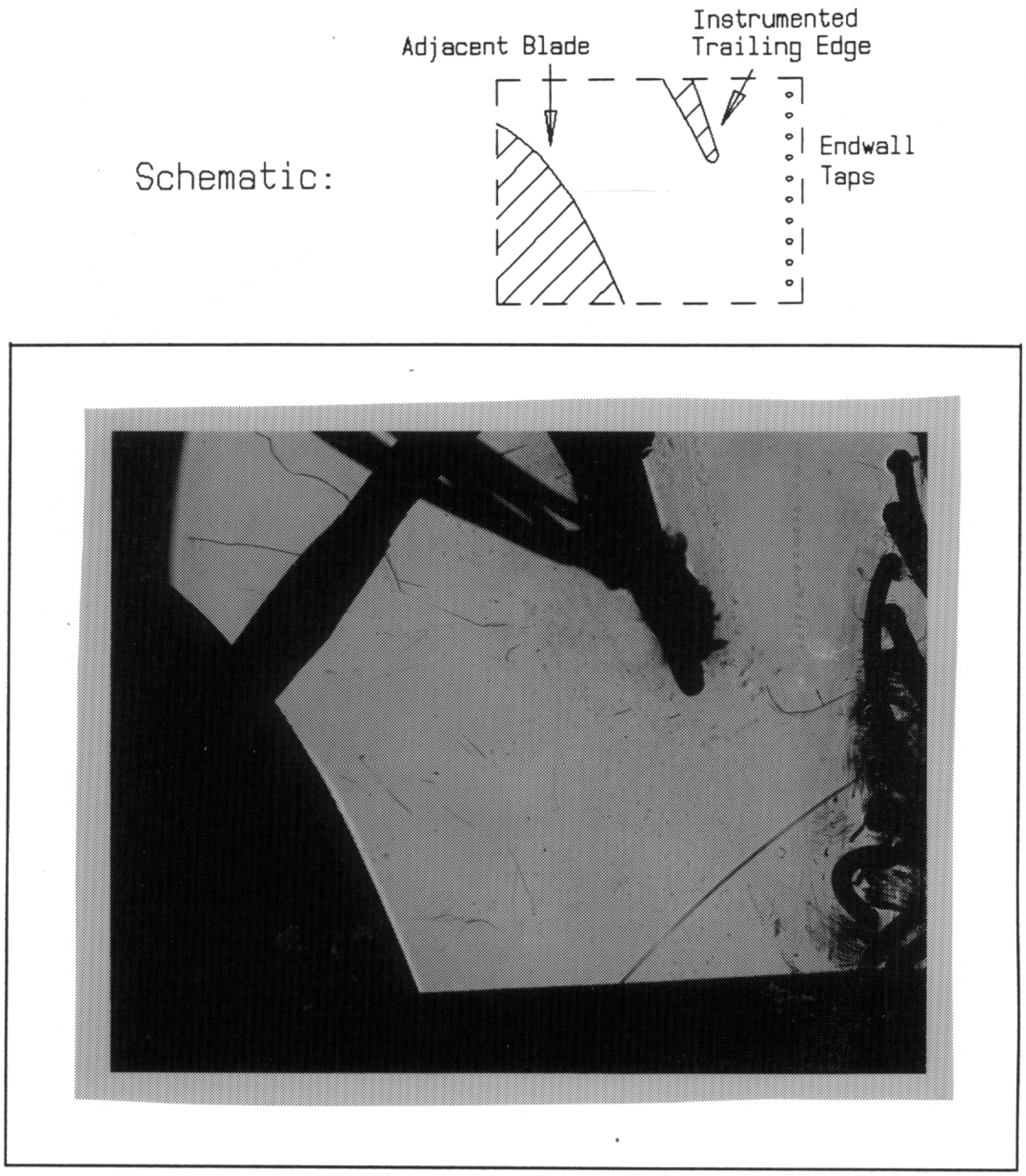

Figure 45. Large Scale Shadowgraph Picture for No Flow

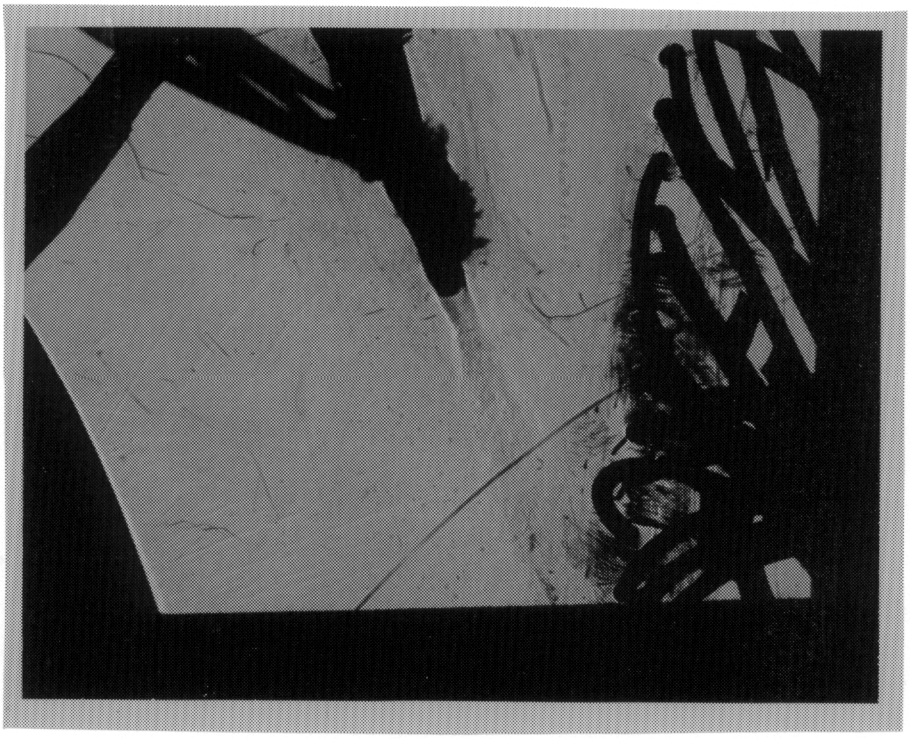

Figure 46. Large Scale Shadowgraph Picture for $M_2 = 0.80$

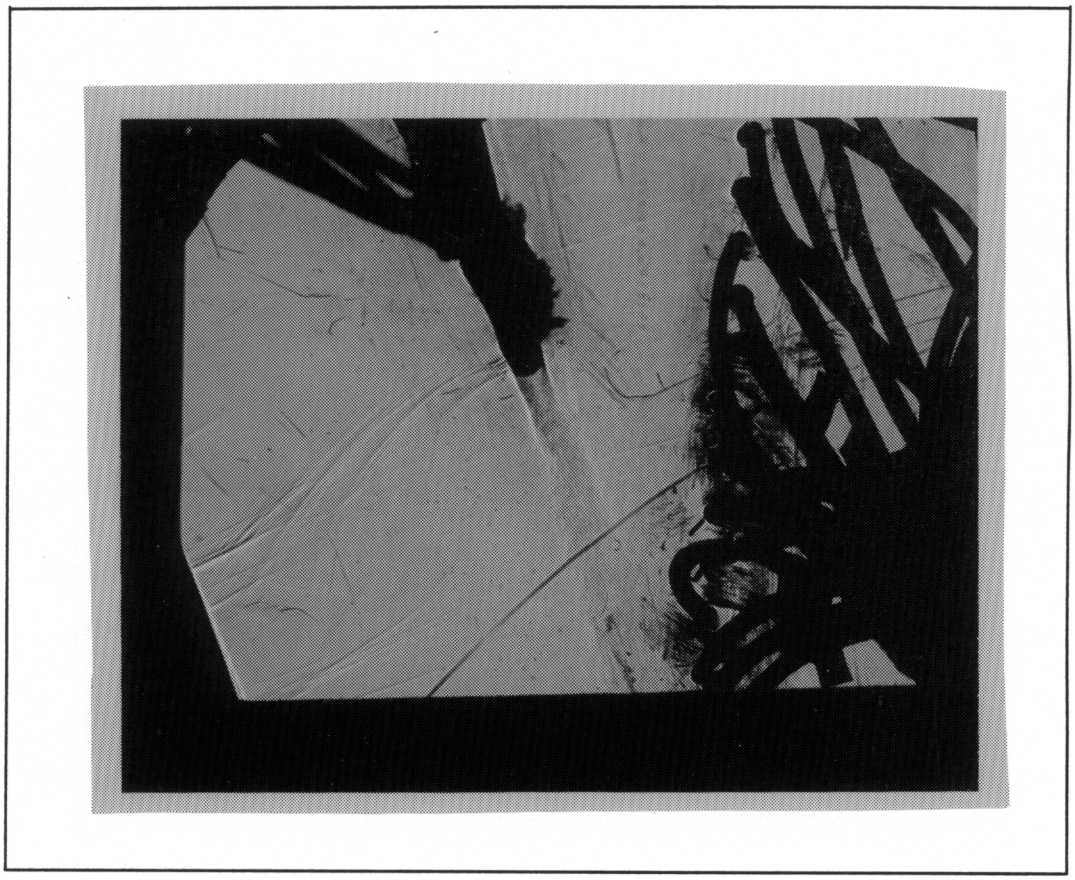

Figure 47. Large Scale Shadowgraph Picture for $M_2 = 0.92$

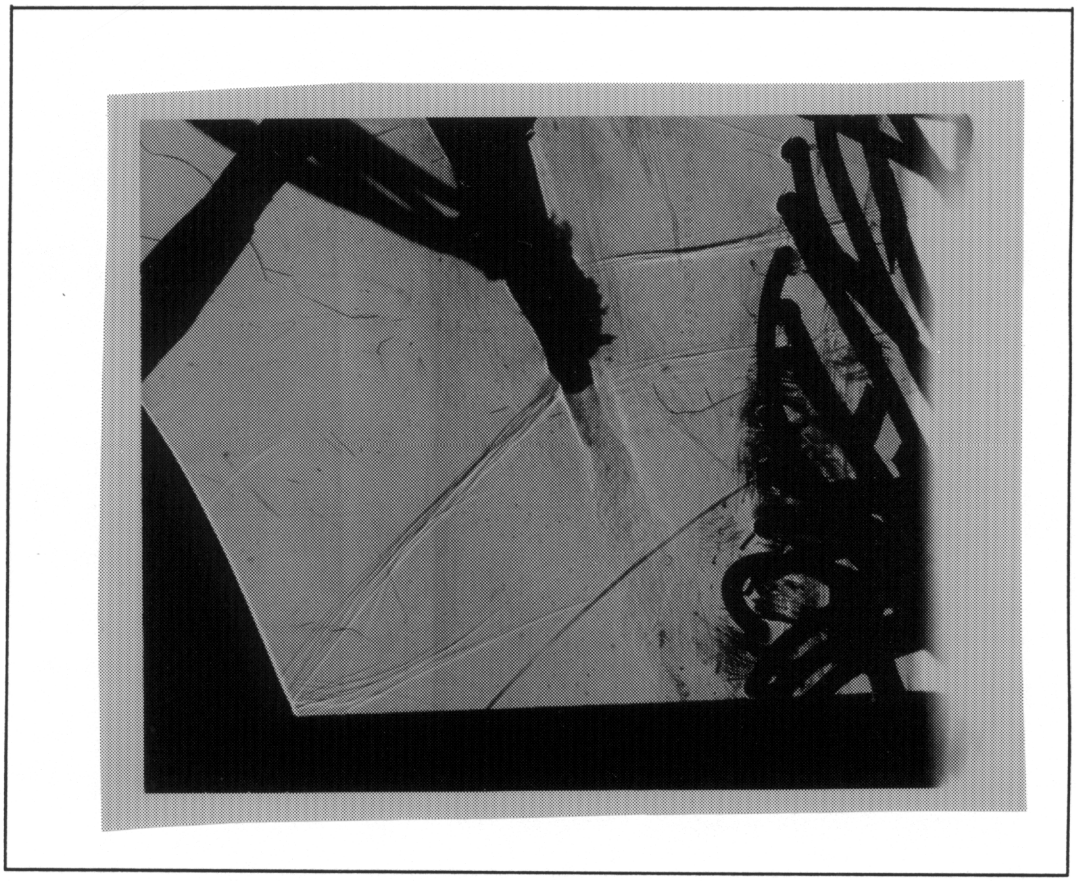

Figure 48. Large Scale Shadowgraph Picture for M_2 = 1.05

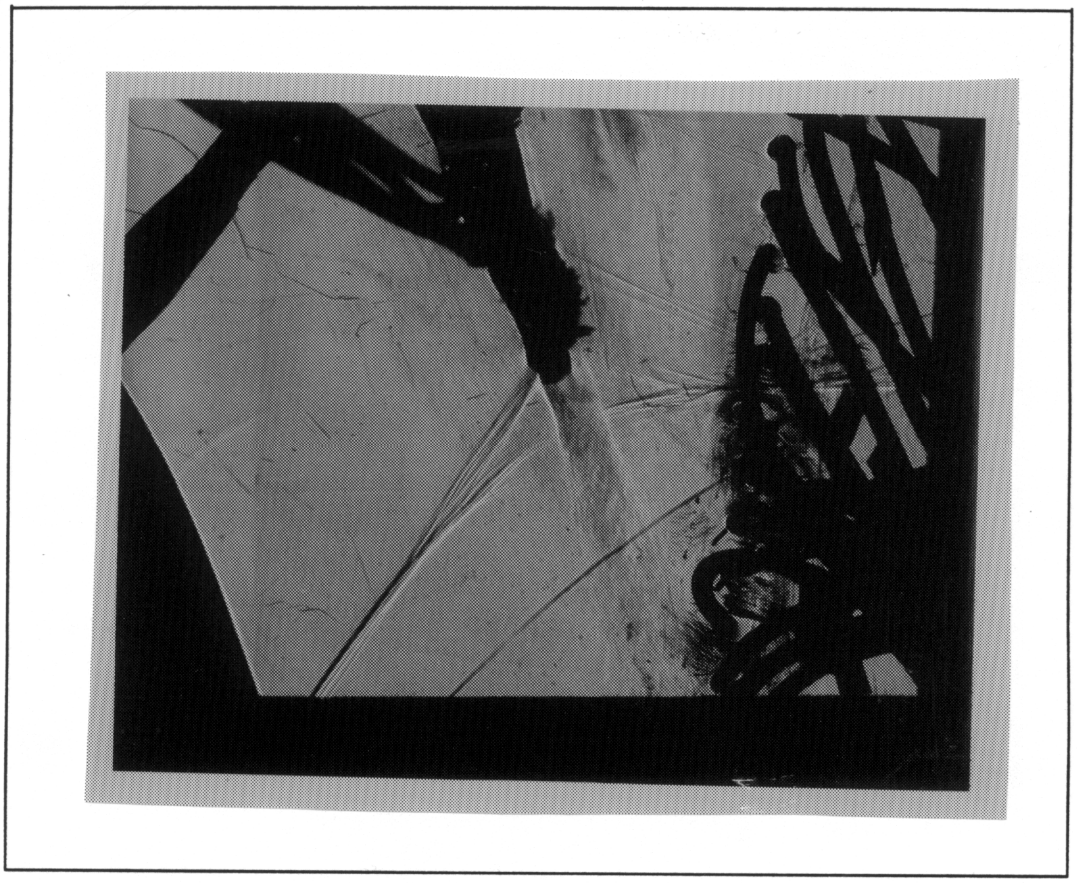

Figure 49. Large Scale Shadowgraph Picture for M_2 = 1.13

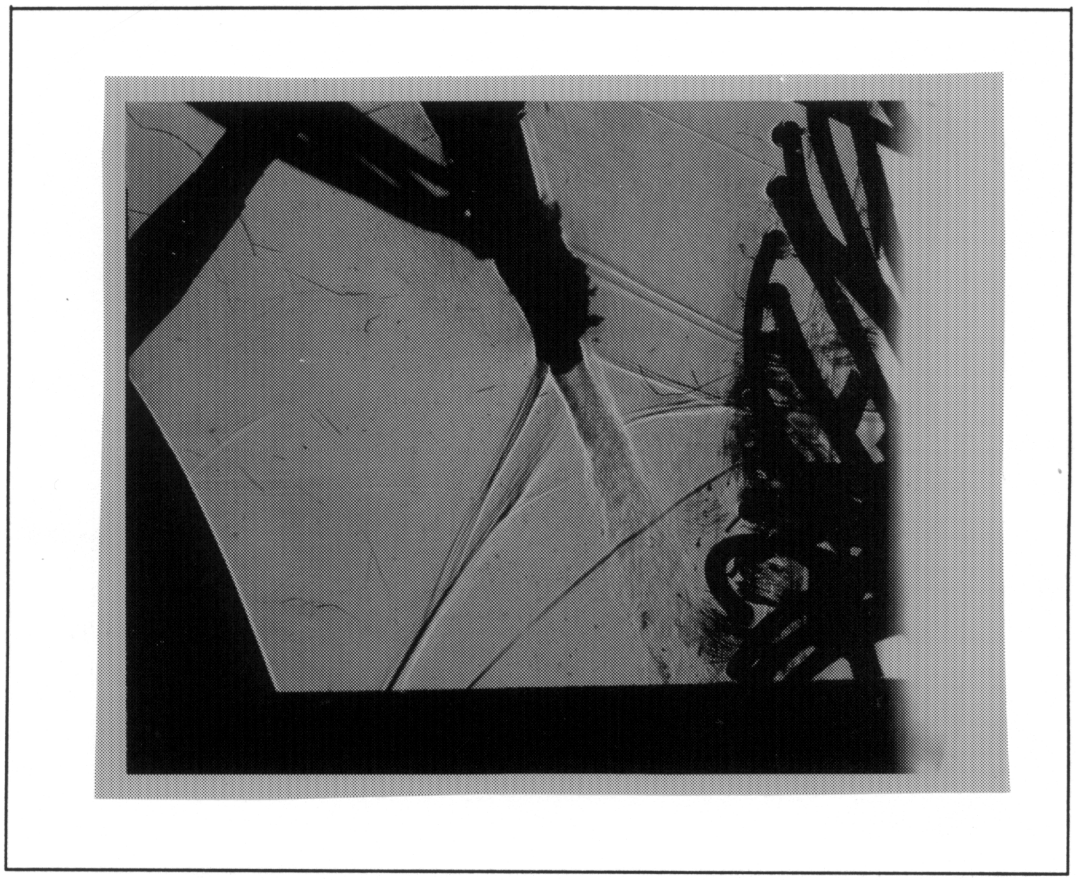

Figure 50. Large Scale Shadowgraph Picture for $M_2 = 1.20$

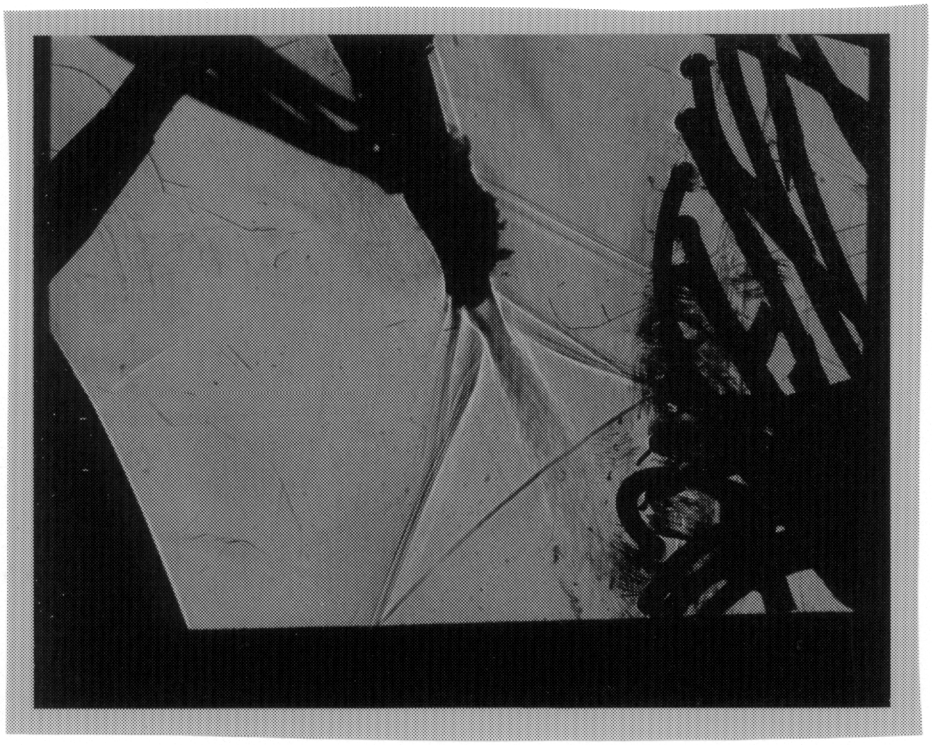

Figure 51. Large Scale Shadowgraph Picture for $M_2 = 1.32$

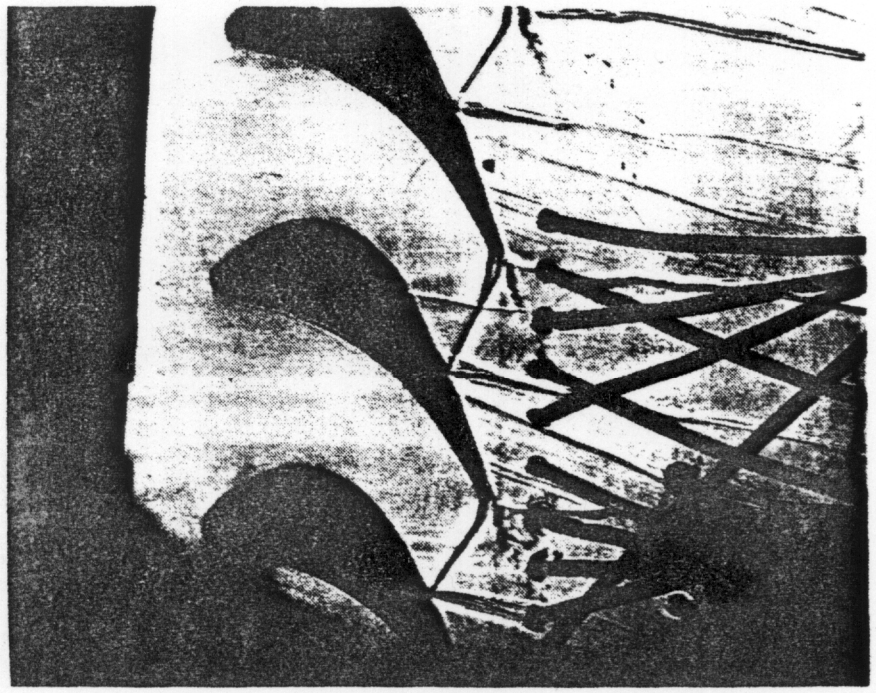

Figure 52. Baseline Shadowgraph Picture for M_2 = 1.17 from Ref. [27]

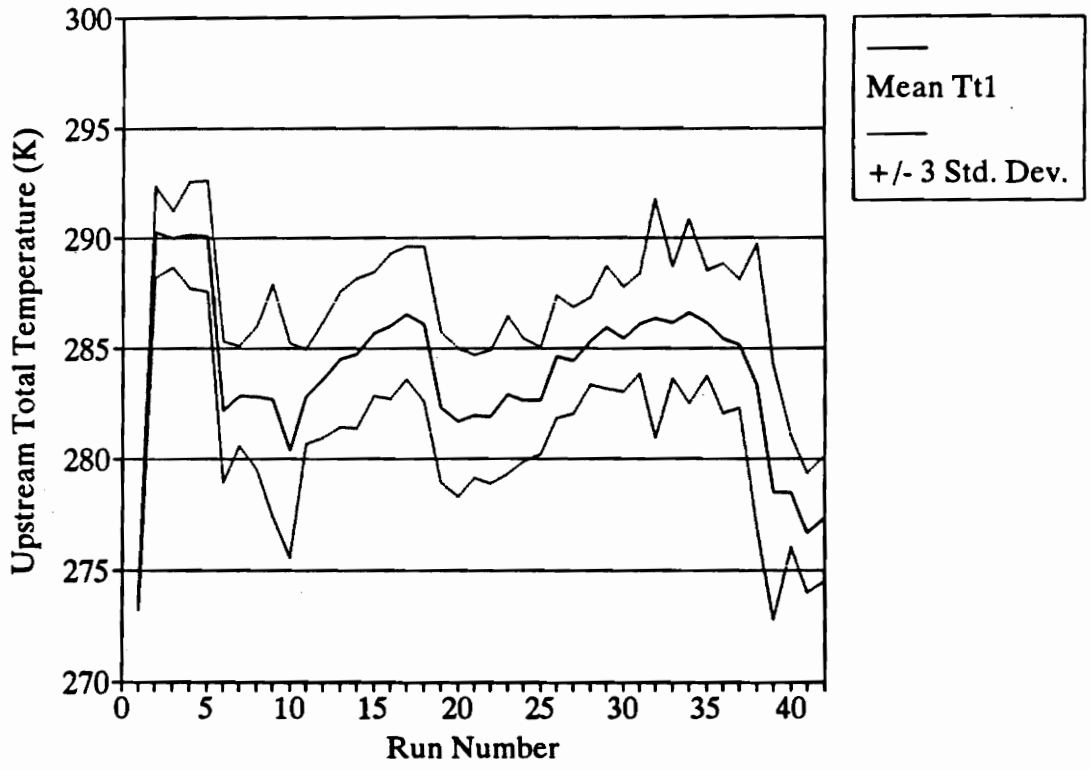

Figure 53. Variation of Upstream Total Temperature for Several Runs

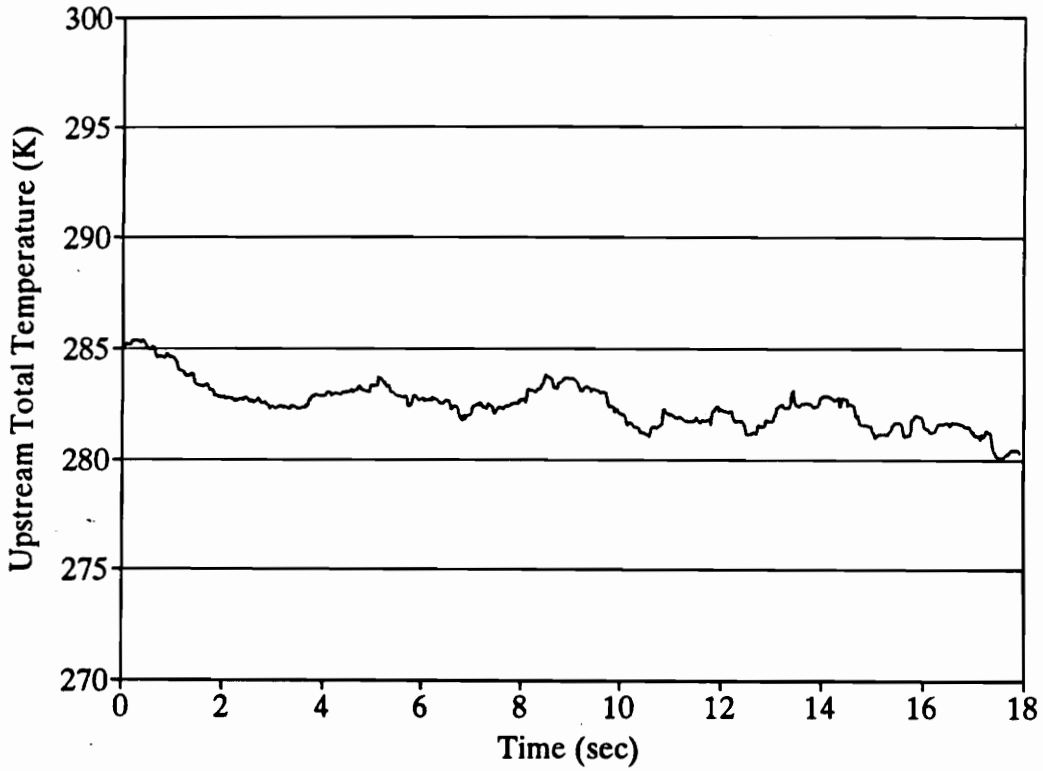

Figure 54. Variation of Upstream Total Temperature for a Typical Run (M_2 = 0.94)

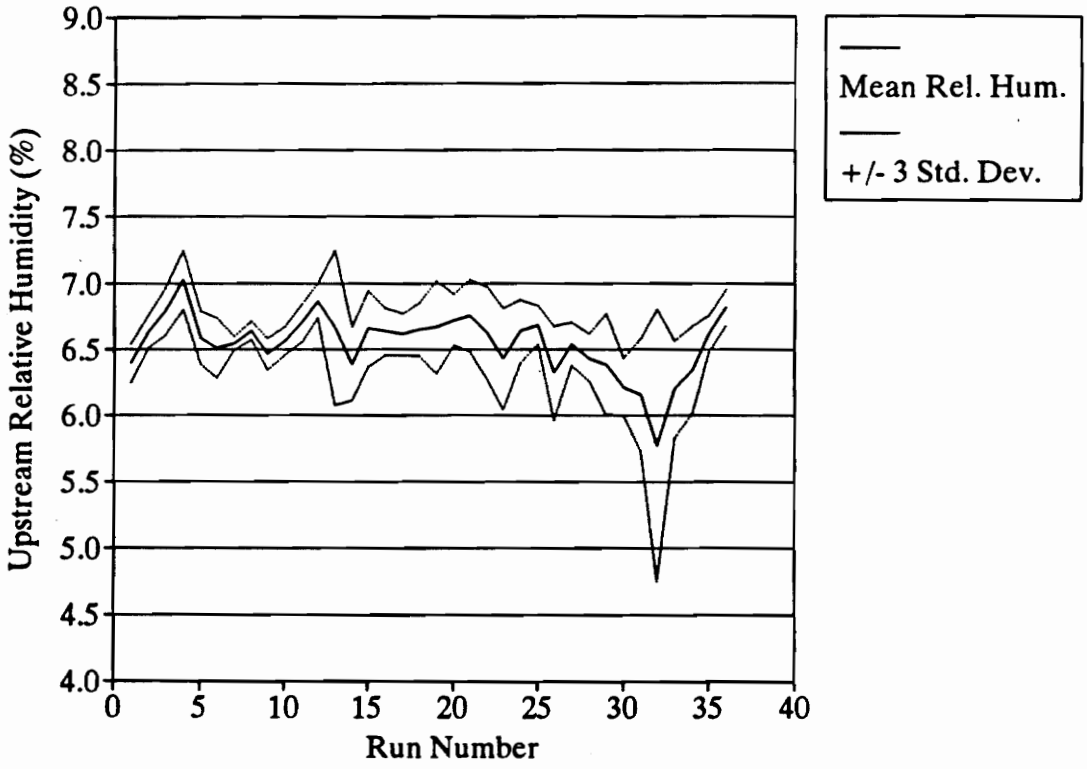

Figure 55. Variation of Upstream Relative Humidity for Several Runs

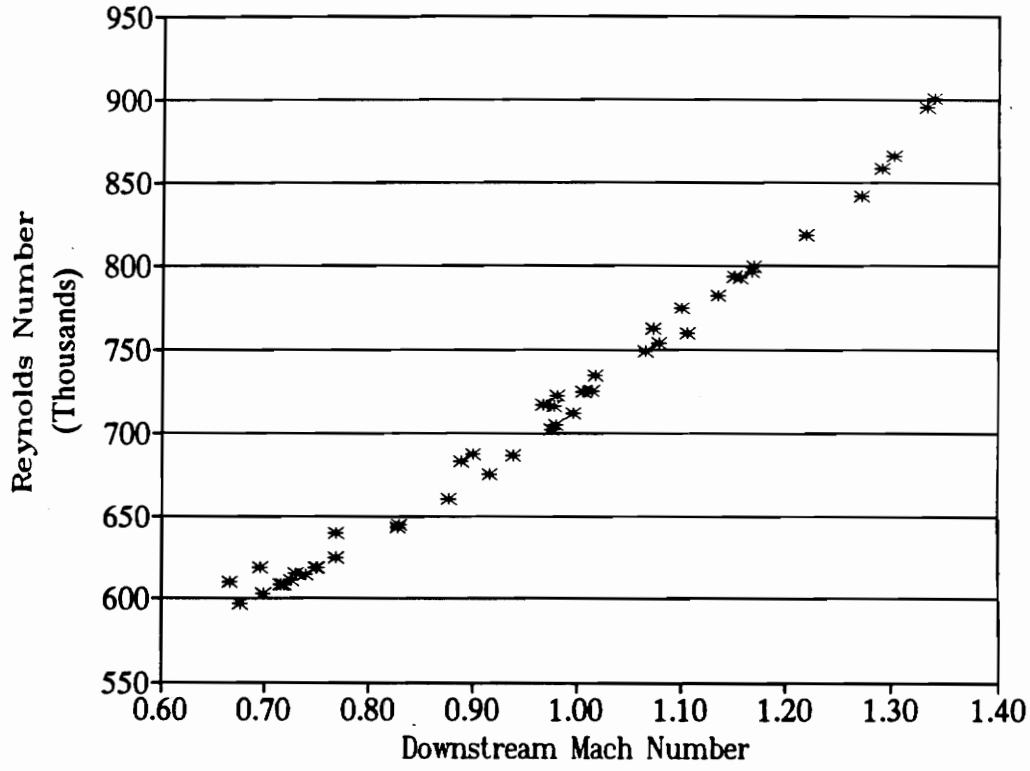

Figure 56. Reynolds Number Versus Downstream Mach Number

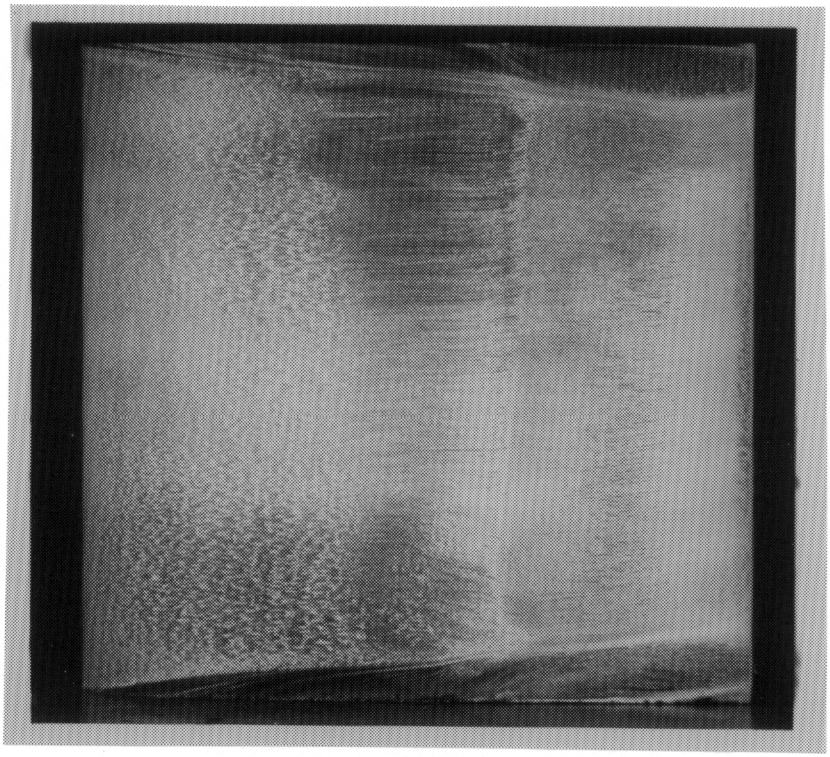

Figure 57. Suction Side Flow Visualization $M_2 = 1.20$

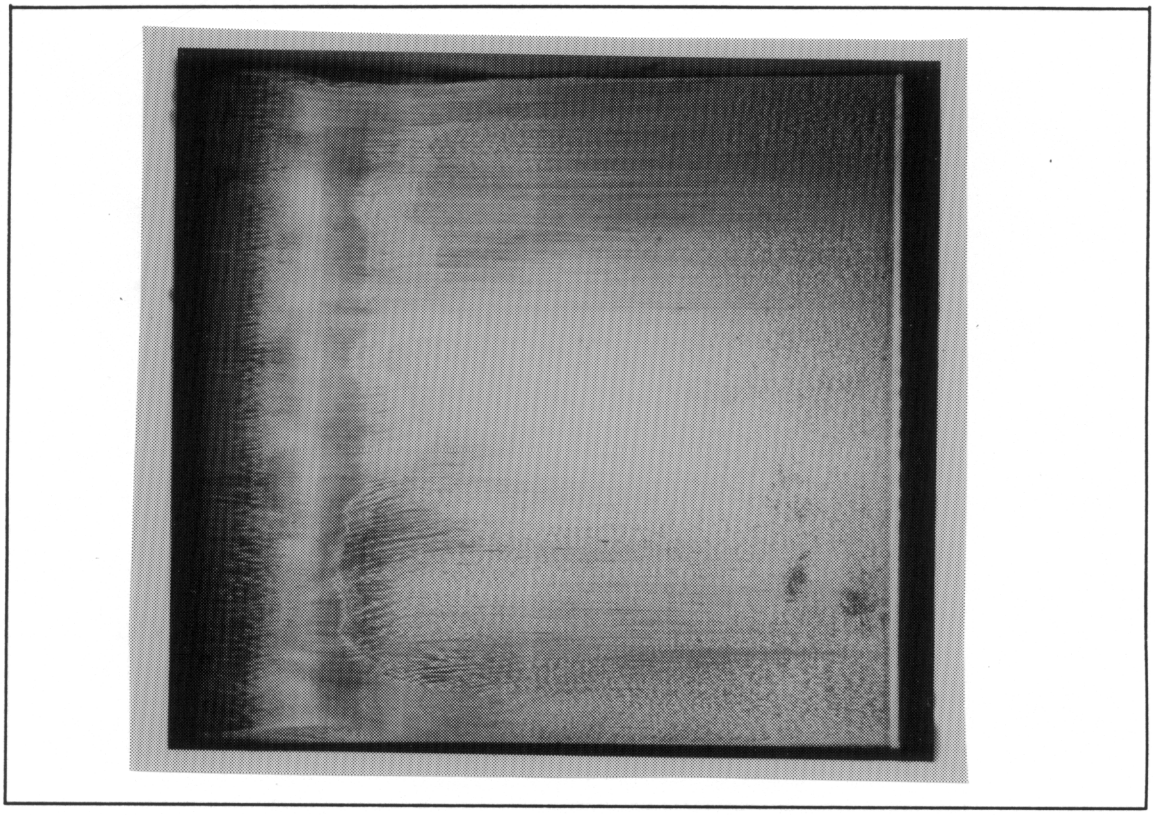

Figure 58. Pressure Side Flow Visualization $M_2 = 1.20$

VITA

The author was born on March 21, 1969 in Columbus, Ohio to Richard and Jacqueline Walls. He grew up near Richmond, Virginia, where he graduated from Monacan High School in 1987. He graduated summa cum laude with a Bachelor of Science degree in Mechanical Engineering at Virginia Tech in 1991. He stayed on at Virginia Tech to earn a Master of Science degree in Mechanical Engineering in 1993. He will begin working at Lexmark International in Lexington, Kentucky this fall.